Implementation and Application of Methods for Micro-Gravity Emulation

by

Thomas Richard Johnstone Corrigan

Bachelor of Science in Mechanical Engineering
University of Minnesota (1992)

Bachelor of Science in Applied Physics
Saint John's University (1992)

Submitted to the
Department of Mechanical Engineering
in partial fulfillment of the requirements for the degree of

Master of Science in Mechanical Engineering

at the

Massachusetts Institute of Technology

September 1994

Signature of Author ______________________________
Department of Mechanical Engineering
August 12, 1994

Certified by ______________________________
Steven Dubowsky
Thesis Supervisor

Accepted by ______________________________
Ain A. Sonin
Chairman, Departmental Graduate Committee

Implementation and Application of Methods for Micro-Gravity Emulation

Submitted to the
Department of Mechanical Engineering
in partial fulfillment of the requirements for the degree of
Master of Science in Mechanical Engineering

by

Thomas Richard Johnstone Corrigan

Abstract

Experimentally evaluating micro-gravity control and planning algorithms for space robotic systems on earth is difficult because gravity masks the more subtle dynamic forces which dominate in space. Previous experimental test beds for micro-gravity have been largely restricted to planar motion, or have other limitations. A system called the Vehicle Emulation System (VES), a fully spatial system, overcomes many of these problems. However, compensating for the effects of gravity with the VES is a challenge.

This thesis presents two methods of gravity compensation, the Learning Method and the Model Method, which allow fully spatial emulation of the micro-gravity interaction between a space manipulator and its supporting structure or spacecraft. Experimental results show the effectiveness of the methods.

These micro-gravity emulation techniques are used to experimentally evaluate the effectiveness of two space robotic algorithms, the Coupling Map Algorithm and the Pseudo-Passive Energy Dissipation Concept.

Finally, the design and evaluation of a digital filter which improved the performance of the VES system is presented.

Thesis Supervisor: Dr. Steven Dubowsky
Professor of Mechanical Engineering

Acknowledgments

I will always be grateful to my advisor, Professor Steven Dubowsky, for giving me one of the greatest opportunities of my life. His guidance and advice, in engineering, professionalism, communication and life itself will stay with me forever.

I would like to thank my predecessors in the group who made my transition to MIT an enjoyable experience. They are Andrew Kuklinski, Dalila Argaez, Chantal Moore, Peng Yun Gu, Miguel Torres, Joe Deck, and Attilio Pissoni. I would especially like to thank Andrew and Dalila for filling my first year at MIT with adventures, lots of laughs, and a fair amount of goofing around.

I thank Craig Sunada whose entrance to the group--as well as married life--coincided with mine, for providing camaraderie and friendship. Thank you to the students who joined the group after me--Jeff Cole, Nathan Rutman, Richard Wang and Michele Tesciuba--for making me feel like I knew what was going on once in a while, and for making the lab and office enjoyable.

To my loving wife Mary I owe the greatest thanks for supporting me through countless hours of research, and for inspiring me to pursue excellence. Consider this a toast.

To my Parents I owe a great deal of thanks; for providing the genetic and educational framework for success, and for a life time of unconditional love and support. I would also like to thank my brother Pat and sisters Beener, Bell, and Kaz for their support, and for making my life more interesting. I would like to thank my two best friends, Kevin Davis and Terry Szymanski, for spending countless hours keeping me in touch (electronically) with my home.

I would like to recognize the efforts of the professors and students who proceeded me in the VES project and made my own research possible. They include Professor Will Durfee, Professor Igor Paul, Uwe Müller, Husni Idris, Jay Baker, and Andrew Kuklinski. The support of NASA grant NAG-1-801 for this work is also recognized.

Table of Contents

List of Figures

Chapter 1

Introduction

1.1 Background and Literature Review

The hazard and expense of space maneuvers makes extensive preflight experimental testing of control and planning schemes for space robotics critical. The gravity of earth dominates most dynamic systems, making micro gravity emulation difficult.

In many proposed space applications there are important dynamic interactions between a manipulator and its base structure [Umetani and Holcomb 1990]. These applications include free floating systems, such as a robot mounted on a small satellite, and free flying systems, where the robot-satellite combination is positioned by reaction jets [Erickson et al 1989]. Another important scenario is a space robotic manipulator carried by a long slender arm from a base structure [Crane et al. 1991], such as the space manipulator system idealized in figure 1-1.

A number of planning and control algorithms have been proposed for robotic systems in the micro-gravity of space [Xu and Kanade 1993]. It is relatively easy to test these algorithms in simulation; however, experimental tests are required to validate their effectiveness fully. Performing such tests in terrestrial laboratories is difficult since gravity often masks the dynamic effects which dominate in the micro-gravity of space. For example, the dynamic forces and moments exerted by a free flying space manipulator on its spacecraft can cause undesirable system motions if these are not compensated for [Papadopoulos and Dubowsky 1993].

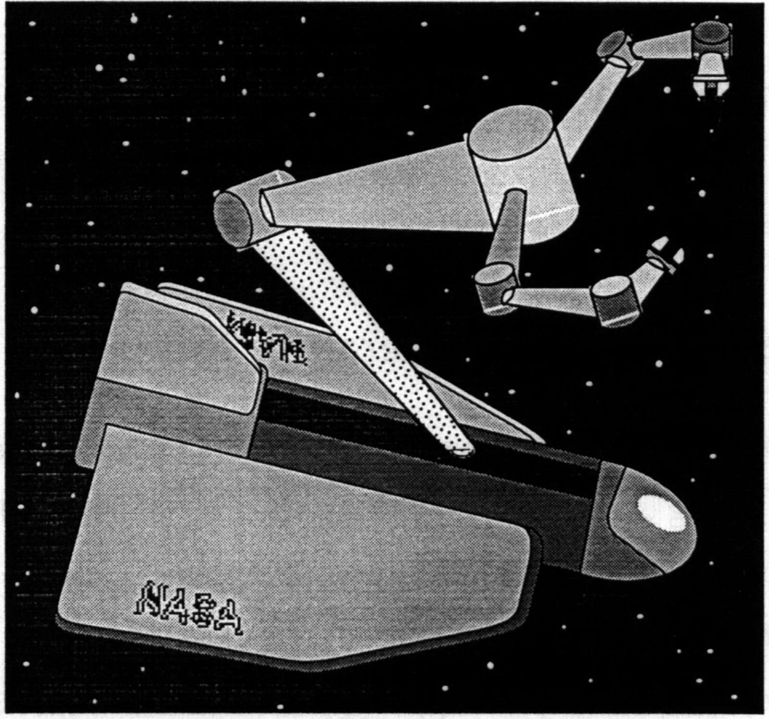

Figure 1-1: Space Manipulator System Concept.

Each of the existing test bed systems developed to study the dynamics and control of space manipulators in micro-gravity has advantages and limitations. The most common systems use air bearings riding on a flat surface to support a manipulator system [Alexander and Cannon 1990, Umatani and Yoshida 1989]. These relatively simple and useful studies are restricted to planar motion. But the complex nature of real space robotic systems makes their full three dimensional behavior important. Neutral buoyancy tanks are used to approximate three dimensional weightless motions [Spofford and Akin 1990]. These systems are effective for some studies, but fluid damping and inertia can corrupt the results when a system's dynamic behavior is important. The complexity of suspension systems with counterbalancing mechanisms proposed for micro-gravity emulation makes their reliable, accurate use difficult at best [Sato et al. 1991, Ulrich and Kumar 1991]. Finally, other systems only simulate micro-gravity with approximations of a system's dynamics [Iwata et al. 1990, Shimoji et al. 1989, Whittaker et al. 1991]. Complex three dimensional dynamic interactions cannot be completely studied with any of these approaches.

A system called the Vehicle Emulation System Model II (VES) developed at MIT permits the experimental evaluation of planning and control algorithms for mobile terrestrial and space robot systems by using an approach called "admittance control" [Fresko 1987].

1.2 Purpose of this Thesis

The VES II is a second generation experimental test bed, designed and built to study experimentally the three dimensional motion of complex mobile manipulator systems. An earlier version, the VES I was built in the 1980's and used to study several manipulator control algorithms [Stelman 1988]. The VES II was designed to investigate a wider range of dynamic systems with an increased accuracy (Müller 1992, Idris 1992, Kuklinski 1993). With effective gravity compensation, the VES II is now capable of emulating micro-gravity conditions.

Previous theses have detailed the design of the VES II hardware (Müller 1992), the software used to control the VES II (Idris 1992), and the integration of many components to get the system working well (Kuklinski 1993). This thesis documents the final addition to the VES II system, the ability to emulate micro-gravity environments to study space robotics. Two methods of compensating for gravity are presented to achieve this emulation, the Learning Method and the Model Method. Two control and planning algorithms for space robotics are investigated with the VES II system to demonstrate the use of the gravity compensation technology. The addition of a digital filter to improve the performance of the system, is also documented. The equations used by the gravity compensation methods are compiled in the appendices, along with a detailed handbook for operating the VES II.

1.3 Outline of Thesis

This thesis is organized into 6 chapters. This chapter serves as an introduction to set the background and purpose for the work. An overview of the basic VES system is presented in Chapter 2. The hardware and software architecture is summarized. The admittance model concept is also discussed.

Chapter 3 describes the inherent difficulties involved in emulating micro-gravity. Two methods of emulating micro-gravity, the Learning Method and the Model Method, are then presented in detail, along with some results which demonstrate the accuracy of these methods.

Chapter 4 reviews space robotics control and path planning theories and applies the VES to analyzing two of them, the Coupling Map Algorithm and Pseudo-Passive Energy Dissipation.

The design and implementation of a digital filter is presented in Chapter 5. The improvements achieved by this filter are also documented.

An extensive series of appendices provides some details of this work. The calculations for generating an admittance model of a beam structure are presented in Appendix A. Appendix B provides details of the PUMA 560 system used in this thesis. The calculations required to create a minimal model of the PUMA 560 are presented in Appendix C. The coordinate transformation from reference frame of the force sensor to the robotic base frame is given in Appendix D. Appendix E provides an operating manual for using the VES system to perform micro-gravity experiments. Errors in the force sensor are discussed in Appendix F. Finally, the full linearized dynamic equations of the PUMA 560 on a flexible base are developed in Appendix G.

Chapter 2

The Experimental System

2.1 Introduction

This chapter describes the basic components of the VES and its operation, including the structure of the computer architecture and the multi-computer coordination required for micro-gravity emulation. Also presented is a discussion of the admittance control concept, used to control the platform motions and emulate any number of structures.

Details of the construction and components used on the VES II are presented by [Müller 1992] and [Kuklinski 1993]. The software used to control the VES II is presented by [Idris 1992] and [Kuklinski 1993]. Detailed operation procedures for the VES system are presented in Appendix E. Appendix B describes the PUMA 560 system which is used with the VES throughout this thesis.

2.2 The VES Basic Operation

The basic components of the VES II are: a 6 degree-of-freedom, high-performance, hydraulically-actuated Stewart platform, a six-axis force/torque

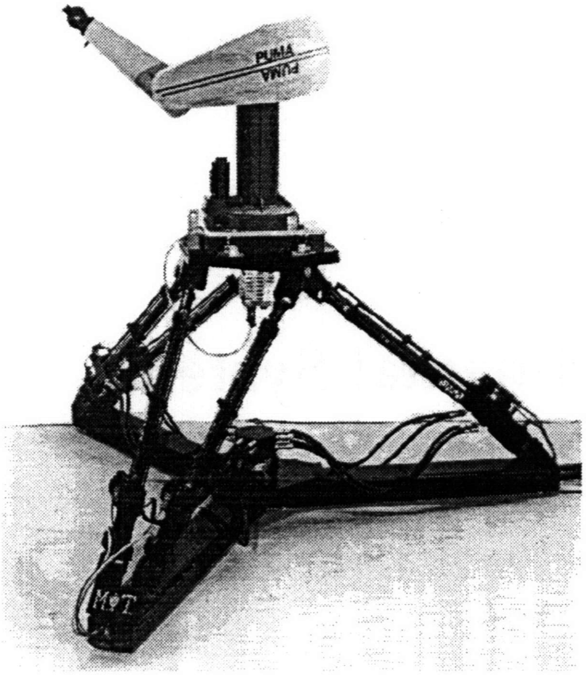

Figure 2-1: The VES II with a PUMA 560

sensor, and a control system based on the admittance control concept [see section 2.3]. Figure 2-1 shows the VES II with a PUMA 560 mounted on it.

The VES II has three basic modes of operation; position control, admittance control, and micro-gravity emulation. Under position control, the platform top is simply commanded to move through a specified motion. The other two modes are more complex.

Figure 2-2 briefly outlines the VES admittance control mode operation. A manipulator system mounted on the VES exerts forces and torques (a wrench) on the sensor, $\mathbf{W}_S$, as it moves. The admittance controller uses this wrench as input to a set of differential equations which describe the dynamics of some system or structure called the vehicle. A more detailed discussion of the admittance concept is presented in Section 2.3, and the process of creating a simple admittance model is presented in Appendix A. Note that platform drawing in Figures 2-2 through 2-4 are based on a drawing in [Baker 1993].

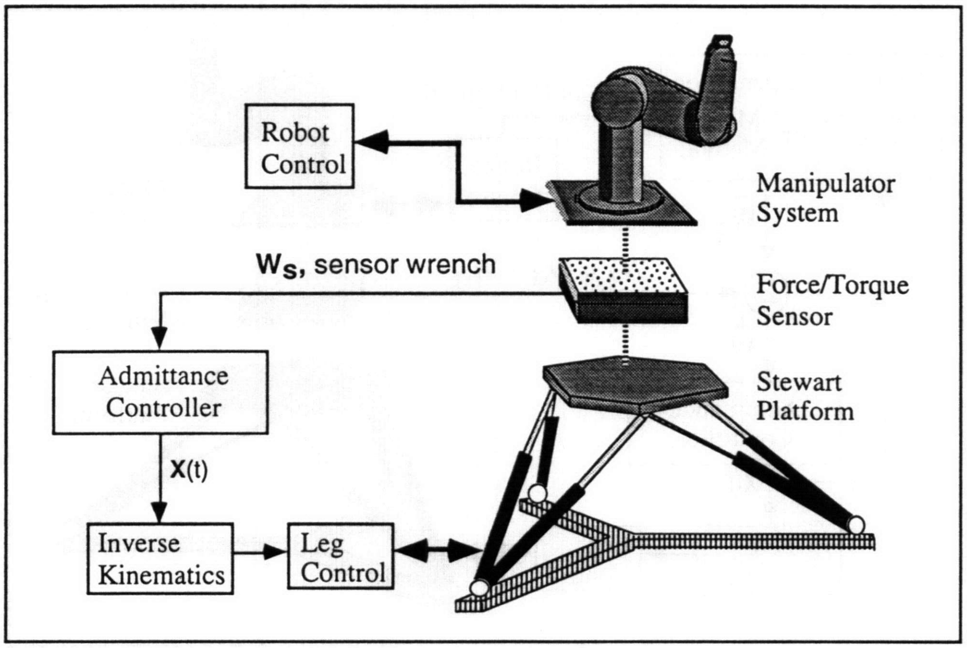

Figure 2-2: VES Admittance Mode Schematic

The admittance controller solves the admittance equation for the platform position, and commands the platform top carrying the manipulator system to move as if it were the vehicle being emulated. The commanded platform position is resolved into hydraulic actuator lengths through inverse kinematics; individual high performance controllers then maintain these desired lengths. Hence the platform top moves in response to manipulator motions in real time in a manner approximating the vehicle being emulated.

For micro-gravity emulation a gravity compensation routine, the Learning Method or Model Method, is used to estimate the static component of the wrench, due to the weight of the manipulator system. This value is subtracted from sensor measurements to leave only the dynamic wrench resulting from the motion of the manipulator, see Figure 2-3.

$$\hat{W}_d = W_s - \hat{W}_g , \tag{2.1}$$

where $\hat{W}_g$ is an estimate of the gravitational wrench from the Learning Method or Model Method, and

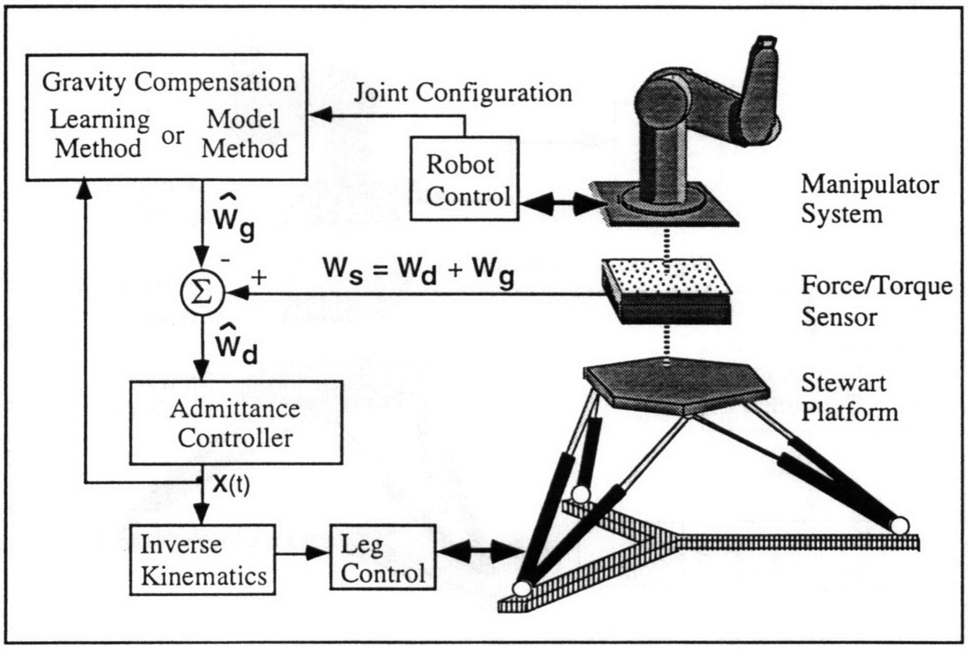

Figure 2-3: VES Micro-Gravity Emulation Mode Schematic

$\hat{W}_d$ is an estimate of the dynamic wrench, used by the admittance controller for micro-gravity emulation.

The admittance controller then operates on the dynamic wrench only, and the platform top moves as if it where the system being emulated, in micro-gravity.

2.3 The Admittance Control Concept

The basic admittance control concept is quite simple [Fresko 1987, Dubowsky et al. 1988, Durfee et al. 1991, Dubowsky et al. 1994]. A model of some physical system is created. Knowledge of the wrench acting on that system, can then be used to determine changes in the system's position and velocity. The general form of the differential equation which defines the system, or vehicle, is:

$$\dot{X}(t) = g\big(X(t), W(t)\big), \tag{2.2}$$

where W(t) is the input wrench as a function of time,

X(t) is the state vector describing the position and velocity of the Stewart platform top as a function of time, and

g() is called the admittance model; a linear or nonlinear function which characterizes the vehicle or structure being emulated.

The position and velocity of the model, **X**(t), are calculated and maintained by the VES. Admittance control gets its name from the form of Equation 2.2, since it takes effort [**W**(t)] as an input and returns flow [$\dot{\mathbf{X}}$(t)] as the output. Complex nonlinear admittance models can be programmed into the VES. In this thesis, a linear model is used which has the form:

$$M\ddot{\mathbf{Y}}(t) + D\dot{\mathbf{Y}}(t) + K\mathbf{Y}(t) = \mathbf{W}(t), \qquad (2.3)$$

where M, K, and D are matrices which describe the mass, spring and damping characteristics of the system being modeled, and

Y(t) = $\{X, Y, Z, \Phi_X, \Phi_Y, \Phi_Z\}^T$ is a state vector describing the position and orientation of the platform top (see Figure 2-4). The Z-Y-X constant angle convention of [Craig 1989] is used to define rotations.

W(t) is the input wrench of forces and moments which correspond with the **Y**(t) axes.

Before being used by the admittance controller, the admittance model is

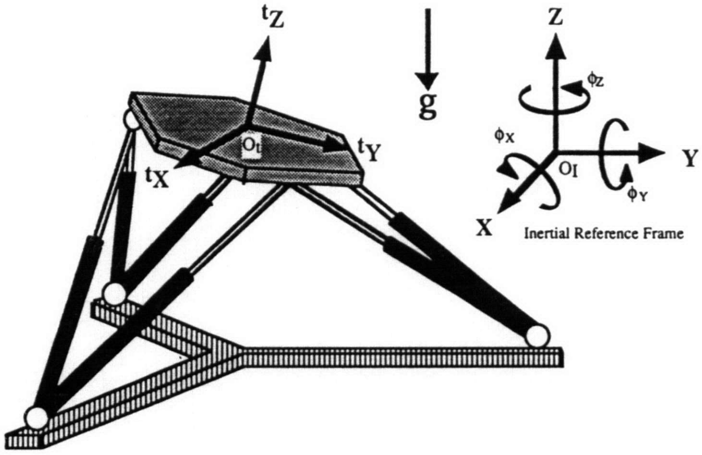

Figure 2-4: Platform frames and rotation axes

converted from a continuous time model, given by equation 3, to a discrete time representation. The discrete system is defined by [Kuklinski 1993]:

$$X_{k+1} = [\Phi]\cdot X_k + [\Gamma]\cdot U_k, \tag{2.4}$$

where $X_k = \{X, Y, Z, \Phi_X, \Phi_Y, \Phi_Z, \dot{X}, \dot{Y}, \dot{Z}, \dot{\Phi}_X, \dot{\Phi}_Y, \dot{\Phi}_Z\}$ is the state vector at discrete time step k,

U_k is the input wrench at discrete time step k.

The discrete space model matrices are a function of the continuous time model and the sampling time, Δt, of the discrete system:

$$[\Phi] = e^{[A]\Delta t} \tag{2.5}$$

$$[\Gamma] = \int_0^{\Delta t} e^{[A]\tau} d\tau \, [B] \tag{2.6}$$

where $[A] = -\begin{bmatrix} [0] & [M] \\ [I] & [0] \end{bmatrix}^{-1} \cdot \begin{bmatrix} [K] & [D] \\ [0] & -[I] \end{bmatrix}$, and

$[B] = \begin{bmatrix} [0] & [M] \\ [I] & [0] \end{bmatrix}^{-1}$.

For the experiments presented in this thesis, the VES emulates a long flexible beam structures similar to the one shown in figure 2-5. Appendix A gives the mass, spring and damper matrices of straight and bent flexible beam systems used in this thesis. Also shown are the calculations used to generate the matrices.

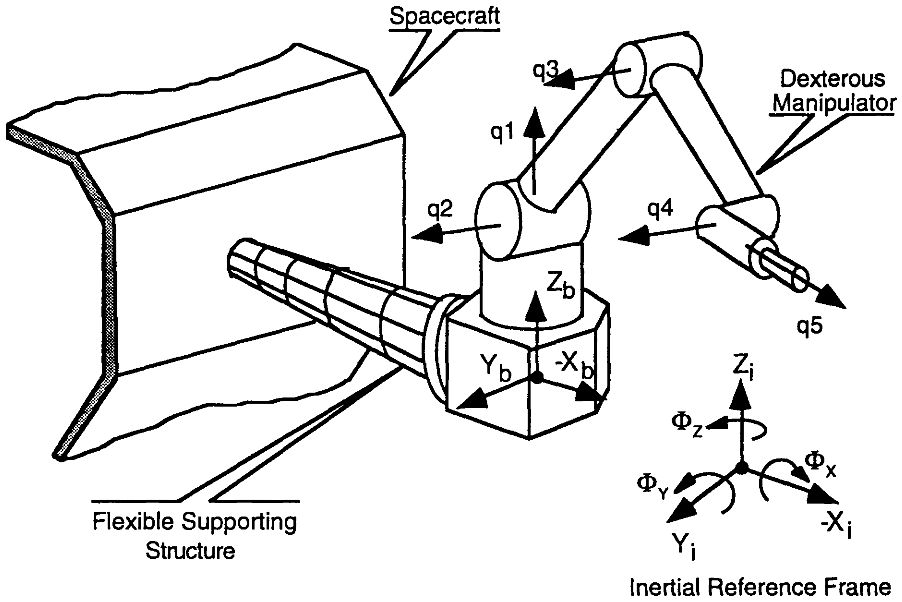

Figure 2-5: Typical VES Space Robotic System
Figure based on [Torres 1993]

2.4 The VES Control Architecture

The VES system is controlled by a fairly complex arrangement of computers and controllers. In addition, performing micro-gravity emulation experiments requires the user to coordinate two control computers.

2.4.1 An Overview

Figure 2-6 summarizes the VES computer architecture. A Sun Workstation serves as the primary interface and software editing platform. The Sun is connected to the main control system via Ethernet.

Admittance based control of the VES platform is supervised by the Redslave, a 68030 based single board computer running the vxWorks operating system. Admittance control is performed using the force sensor measurements read from an analog to digital converter. The desired platform position is converted to individual actuator lengths by inverse kinematics. The Redslave

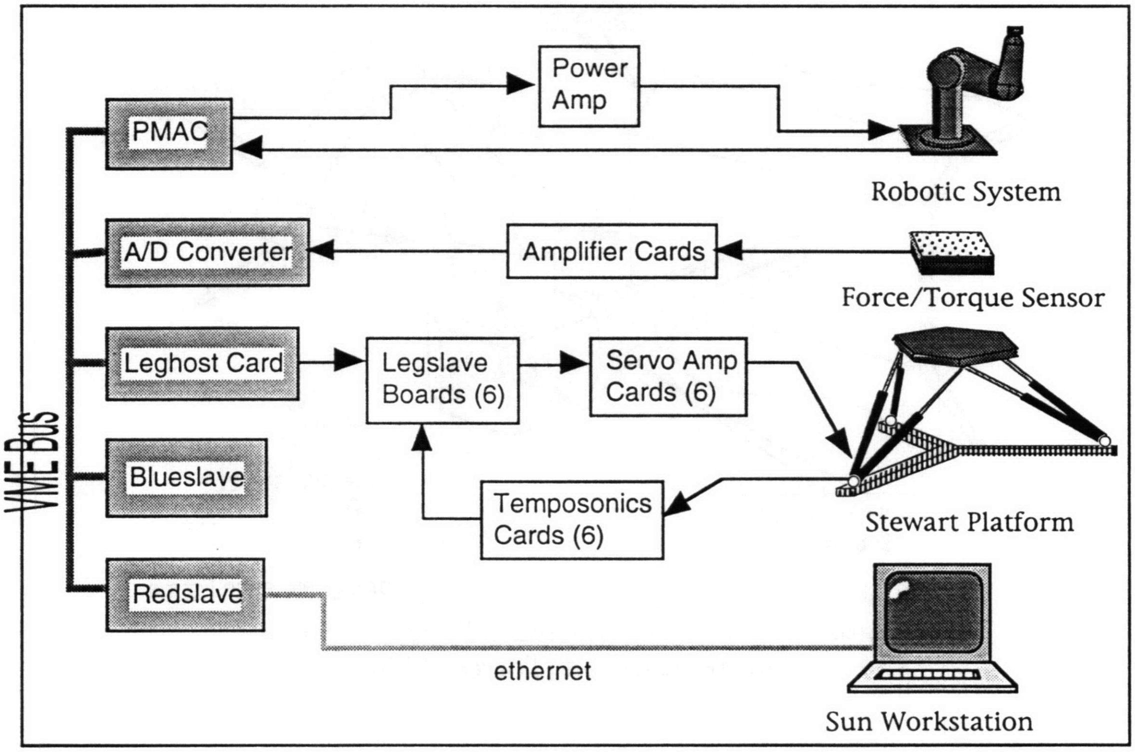

Figure 2-6: VES Computer Architecture

sends the desired lengths to individual legslave controllers through a custom made leghost card at around 100Hz.

The legslaves perform closed loop proportional-derivative control at 500Hz to maintain the desired lengths. The legslaves control the actuator lengths with a signal to Servo Amp cards which send a controlling current to the corresponding servovalve at 1000Hz. A Temposonics linear transducer in each leg sends an electromagnetic pulse from the base of the leg through a shaft inside the rod which is reflected back at the end of the leg. The time it takes for the pulse to return is measured by a Temposonics card and made available to the legslave every 341 milliseconds. This provides an accurate leg length as feedback for the closed loop controllers. The legslaves also filter the feedback signals to prevent exciting the natural vibrational modes of the hydraulic legs [see Chapter 5].

The control of the robotic system mounted to the platform is distinct from the control of the platform. The Blueslave, a 68020 based single board computer running the vxWorks operating system, supervises the control of the robotic system. In this thesis, a PUMA 560 was the only robotic system used with the VES. The Blueslave sends desired joint positions to and receives actual joint encoder signals from the PUMA through a Programmable Multi-Axis Controller, or PMAC. The PMAC can perform PID control on up to 8 joints at a time.

When micro-gravity emulation is performed, coordination is required between the platform control system (Redslave) and the robotic control system (Blueslave). The Redslave makes information about the inertial orientation of the platform top available to the Blueslave. In the Model Method, the Blueslave uses this information to calculate an estimate of the gravitational wrench and provides that information to the Redslave so it can be subtracted from the force sensor measurements per Equation 2.1. This transfer of information is done through a shared memory space on the Redslave which both the Redslave and Blueslave can access.

2.4.2 The Platform Admittance Control Cycle

Before an admittance model experiment begins, with or without micro-gravity emulation, a sample rate and admittance model type must be selected. The main platform control loop is driven by a clock interrupt. The sample rate specifies how often the interrupt will be given. If the interrupt comes before the admittance control cycle has been completed the experiment is halted. Sample rates are generally in the range of 75Hz-90Hz, and depend on the number of safety routines activated and the type of admittance model being used. If a complex coupled admittance model is being used, then every element of the 6 by 6 $[\Phi]$ and $[\Gamma]$ matrices (see Section 2.3) must be used in the admittance calculations. If the admittance model is linearly decoupled, then only the diagonal terms are necessary. Similarly, if the admittance model is of a beam, then only certain terms, about half, might be used in the calculation. For a given admittance model, then, the most computationally efficient calculation method is adopted.

Figure 2-8 summarizes the basic admittance control cycle which the Redslave performs during an experiment. The clock interrupt starts the cycle. First, the forces are read from the force sensor. If micro-gravity emulation is being performed, then a gravity wrench estimate from the Blueslave is subtracted from the measured value. Next, the admittance controller performs the calculations described is Section 2.3 to determine the desired position and velocity of the platform. Inverse kinematics are then performed to turn these values into individual leg lengths. A series of safety calculations are then performed to be sure that the desired leg lengths fall within pre-defined safety margins. Finally, the desired leg lengths are sent to the individual legslave

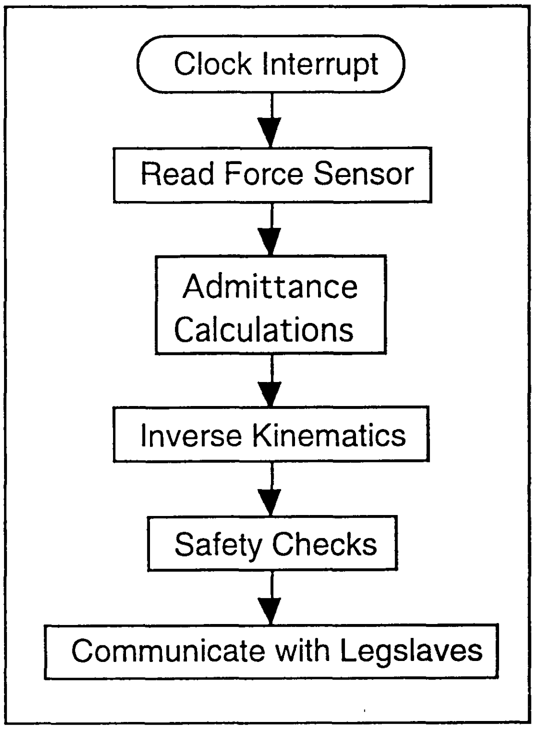

Figure 2-8: Admittance Control Cycle

controllers. More detail of the control software is presented by [Kuklinski 1993].

2.4.3 PUMA 560 Control

The Blueslave controls the motion of the PUMA 560. Direct control of the PUMA is performed by the PMAC. Communication between the PMAC and Blueslave is made simple with the use of dual-ported ram (DPRAM), a memory location which is accessible from both computers. For real time control, the PMAC receives position commands and provides joint encoder information through DPRAM, but this communication is not automatic. The PMAC is programmed to continually read from and/or provide information to a DPRAM address. This small sub-program internal to the PMAC is called a PLC. For real time motion control, a Motion Control Program is written on the PMAC to read desired joint positions and velocities from a buffer space. The buffer space allows the PMAC to always make a smooth transition between any two commanded positions. The PMAC always looks two commands ahead for this reason, so a sufficiently large buffer space is required to allow the Blueslave to fill it with commands while the PMAC is busy performing those commands.

Software has also been written for the Blueslave to estimate the gravitational wrench for the robotic system it is controlling. The theory and form of these equations is presented in Chapter 3. A series of calibration and zeroing procedures are required to accurately perform micro-gravity emulation. A detailed guide to these procedures is presented in Appendix E. Details of the PUMA/PMAC interface and DPRAM are presented by [Baker 1992].

2.5 Summary

This chapter described the basic components and operation of the VES II, including the control architecture and the PUMA 560. The basic theory of the admittance control concept was also presented.

Chapter 3

Emulating Micro-Gravity

3.1 Introduction

This chapter presents the analytical basis which allows gravity to be compensated for to emulate micro-gravity. In Section 3.2, the inherent difficulty in estimating the effects of gravity is discussed, the sources of estimation error are presented, and limits are set for these errors.

The Learning Method and the Model Method are then presented in Sections 3.3 and 3.4 to compensate for gravity and emulate micro-gravity using the VES. The Model Method uses a mass parameter model of the manipulator to calculate and compensate for the forces and moments caused by gravity. The Learning Method uses an iterative learning approach which avoids the need for careful, detailed parameter estimation. Experimental results are presented which show that these methods can accurately extract even relatively small dynamic interactive behaviors from much larger gravitational effects. The two methods are compared in Section 3.5. Note that these methods do not remove the gravity forces seen by manipulator joints, they predict the gravitational wrench at the base of the robot. If necessary, however, joint balancing or feedforward computed torque-control techniques can be used to remove the effects of gravity on the joints.

3.2 The Challenges of Micro-Gravity Emulation

The basic concept of these micro-gravity emulation methods is to subtract the gravity wrench seen by the force sensor from the total wrench to yield an estimate of the dynamic wrench. Micro-gravity emulation can be difficult to achieve if the dynamic wrench estimate is corrupted because of inaccurate estimates of the gravity wrench. Even small errors in the dynamic wrench estimate can cause large errors in the motion of the system.

3.2.1 Wrench Error Sensitivity

The sensitivity of dynamic wrench estimates to gravity wrench errors can be easily demonstrated experimentally. A flexible beam similar to the one shown in Figure 2-5, described in Section A.3, with a PUMA 560 on it was emulated with the VES system. The PUMA was commanded to move its shoulder joint, **q1**, through 180 degrees of motion in 2 seconds with its arm and forearm extended perpendicular to the **q1** axis as shown in Section A.5. This created a large dynamic wrench shown by the solid line in Figure 3-1. Also shown in Figure 3-1 is the range of dynamic wrench estimates, $\hat{\mathbf{W}}_d$, which will result if the error in the gravity estimate, $\delta\hat{\mathbf{W}}_g$, is bounded by 1% or 5% of the total gravity wrench. Clearly, even small errors in $\hat{\mathbf{W}}_g$ will badly corrupt an estimate of $\hat{\mathbf{W}}_d$ since $\mathbf{W}_g$, the gravitational wrench, is much larger than $\mathbf{W}_d$. It is also clear that small sensor errors create similarly large errors in $\hat{\mathbf{W}}_d$, since it must measure the large true gravity wrench. The basic problem is that the sensor must measure a large force (about 1000 Newtons) with very high accuracy.

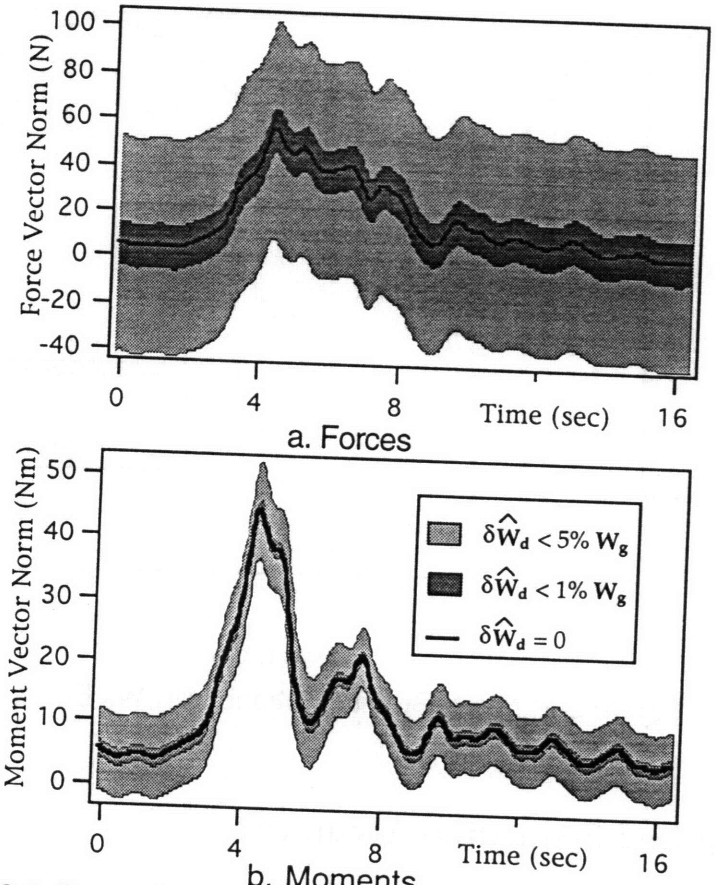

a. Forces

b. Moments

Figure 3-1: Dynamic Wrench Vectors with Gravity Error Ranges

3.2.2 Position Error Sensitivity

The above problem is compounded by the fact that even small wrench errors can cause large position errors during micro-gravity emulation for many space systems. For example, Figure 3-2 shows the translation of the manipulator base in the $\mathbf{Z}_i$ direction, defined in Figure 2-5, during the experimental micro-gravity motion described above. The base motion is shown with 0%, 0.5% and 1% errors in the gravity wrench estimate. Even a 0.5% wrench error causes a very different motion compared to the case with no error, resulting in a poor emulation. For many admittance models, force errors of as little as 1% will actually cause motion errors which are several times the size of the true micro-gravity motion of the system.

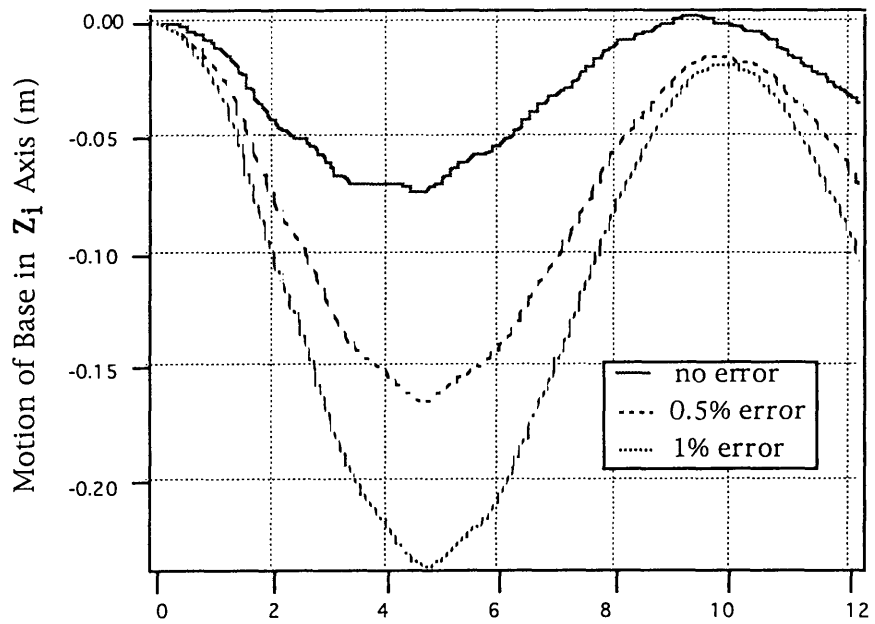

Figure 3-2: Micro-Gravity Motions with $\hat{W}_g$ Errors

3.2.3 Required Estimation Accuracy

A simulation of a typical space robotic system was constructed to investigate the sensitivity of the emulations to gravity wrench estimation errors. Errors were introduced to the dynamic wrench of the simulations and the effect on the system motion was observed. It was found that to maintain motion accuracy of a few percent, it was necessary for the errors in $\hat{W}_d$, called $\delta\hat{W}_d$, to be less than 1.0 Newton of force or 1.5 Newton-meters of moment for the VES with a typical payload of a thousand Newtons. The gravity wrench estimate must therefore be accurate to 0.1%, which is no easy task.

3.2.4 Error Sources

Error in the dynamic wrench estimate has two main sources, the sensor measurement error, δW_s , and error in the gravity wrench prediction, $\delta\hat{W}_g = W_g - \hat{W}_g$. The total dynamic wrench estimate error is their sum:

$$\delta\hat{W}_d = \delta W_s + \delta\hat{W}_g, \tag{3.1}$$

Both these error sources must be minimized to emulate micro-gravity accurately.

Some errors in sensor measurements are repeatable. For example the geometry of strain gauges used in the sensor causes a signal in one axis because of forces in another. This "cross talk" is a repeatable sensor error. The electronics which process the strain gauge signals can also introduce repeatable errors. Multiplying the signals by a calibrating matrix was found to compensate effectively for these repeatable errors since our sensor and electronics are well characterized by a linear model. A method of experimentally determining this calibration matrix is presented in Section 3.4.5.

Non-repeatable sensor errors occur principally due to high frequency electronic noise (> 10-20 Hz) and low frequency thermal drift (< 1 Hz). High frequency noise can be eliminated by analog and digital filters. Note that only relatively low frequency signals are necessary for micro-gravity emulation. Signal frequencies well above the natural frequency of the space system being emulated, generally a few Hertz, can be filtered. The effect of low frequency drift can be minimized by establishing a protocol to reset the sensor offsets before each experiment. Details of the force sensor noise and drift are presented in Section 5.2.1.

Although system performance during micro-gravity emulation is very sensitive to sensor errors, we found that these could be reduced to acceptable levels by the use of a high quality sensor, precise multi-axis calibration, filtering, and careful experimental protocols. The reduction of the other major error source, the gravity wrench estimate, is not quite so direct.

The gravity wrench is a function of several variables:

$$\mathbf{W_g} = \mathbf{W_g}(\mathbf{q},\Phi,\mathbf{P}), \tag{3.2}$$

where $\mathbf{q}$ is a vector of the manipulator system joint displacements, Φ is a 3x1 vector of manipulator base (Stewart platform top) inertial orientation angles, and $\mathbf{P}$ is a vector of mass parameters of the system.

Both $\mathbf{q}$ and Φ are controlled variables, while $\mathbf{P}$ is a physical property of the manipulator. Each of these variables can introduce some error to the gravity wrench estimate. The gravity wrench due to manipulator joint errors are not generally important. Typical manipulator joint encoders produce such small errors that they have a negligible effect on $\delta\hat{\mathbf{W}}_g$. Although errors in knowledge of the manipulator base orientation can cause significant errors in the gravity prediction, the positioning accuracy of the VES Stewart platform can be used to greatly reduce these errors (see Section 5.2.2). The major source of error in $\hat{\mathbf{W}}_g$ is reduced to the term, $\mathbf{P}$, in Equation 3.2.

Two methods are presented for accurately predicting the gravitational wrench, the Learning Method and the Model Method. The Model Method directly finds the manipulator mass parameters, $\mathbf{P}$, and the exact relationship of Equation 3-2, while the Learning Method iteratively finds $\mathbf{W_g}$ without explicitly solving for the mass parameters.

3.3 Learning Method Gravity Compensation

The gravitational wrench of a manipulator can be "learned" iteratively during its motion on the VES. This produces accurate space emulations with minimal analysis and real time computation. Also, it does not require accurate mass parameter identification. However, the learning method can be used only for experiments where the commands to the system are known in advance and are repeatable. It is inapplicable for telerobotic experiments involving human supervisors, or for other experiments with spontaneous events.

The method finds directly the reaction motions of the manipulator base structure (the platform top) caused by the dynamic forces for a given manipulator motion, $\mathbf{q}(t)$. At each iteration, a trajectory of the manipulator base $\hat{Y}(t)$, an approximation of the micro-gravity dynamic base motion, is used to form an estimate of the gravity wrench $\hat{\mathbf{W}}_g(t)$. The manipulator is moved very slowly through $\mathbf{q}(t)$ while its base is moved through $\hat{Y}(t)$ and the sensor readings are recorded. Since the gravity wrench is a function only of system positions, at low velocities (those with negligible dynamic effects) the measured wrench will be equal to the gravity wrench. The accuracy of this estimate depends on how closely the base motions used in the iteration approximate the true micro-gravity dynamic motions. If the true micro-gravity base motion is not large, an initial guess of no base motion can be iteratively improved until the correct micro-gravity system motion is found. The estimate found, $\hat{\mathbf{W}}_g$, is then subtracted from actual sensor readings during a full speed motion to yield an estimate of the dynamic base wrench, $\hat{\mathbf{W}}_d$, which is then used by the controller to produce a better estimate of the micro-gravity base motion. Hence the iterative procedure consists of obtaining an improved estimate for the platform motion and then using the platform motion to produce an improved estimate of $\mathbf{W}_g$.

3.3.1 The Learning Algorithm

The iterative learning procedure can be written as follows. First we define:

$s = \alpha \cdot t$ is a time variable scaled by α,

$\mathbf{q}(s)$ is a well defined, repeatable manipulator motion,

$\hat{\mathbf{W}}_g^i(s)$ is a gravity wrench estimate for iteration i, and

$\hat{Y}^i(s)$ is an estimate for the trajectory of the manipulator base in iteration i.

First, the admittance model of the spacecraft or supporting structure to be emulated is developed and programmed into the VES. Figure 3-3 summarizes the two phase iterative procedure. At each iterative step i {i=1, 2, ... n} the following occurs:

PHASE A:

1) The time scale is set to make all actions slow, with no dynamic effects, $\alpha \gg 1$.

2) The platform performs motion estimate $\hat{Y}^{i-1}(s)$ slowly, while the manipulator moves slowly through $\mathbf{q}(s)$. Recall that the initial guess $\hat{Y}^0(s)$ is usually no motion.

3) The wrench on the sensor is recorded as an estimate for the gravity wrench $\hat{\mathbf{W}}_g^i(s)$, with no dynamic effects

PHASE B:

4) The time scale is set to create full speed actions, $\alpha=1$, and the manipulator moves through $\mathbf{q}(s)$ at full speed.

5) A dynamic wrench estimate is formed by subtracting the gravity wrench estimate (recorded in step 3) from current sensor measurements: $\hat{\mathbf{W}}_d^i(s) = \mathbf{W}_s - \hat{\mathbf{W}}_g^i(s)$.

6) $\hat{\mathbf{W}}_d^i(s)$ is used as input to the admittance model, which moves the platform through $\hat{Y}^i(s)$, an improved estimate of the actual micro-gravity platform motion.

7) Iteration i+1 begins at step 1.

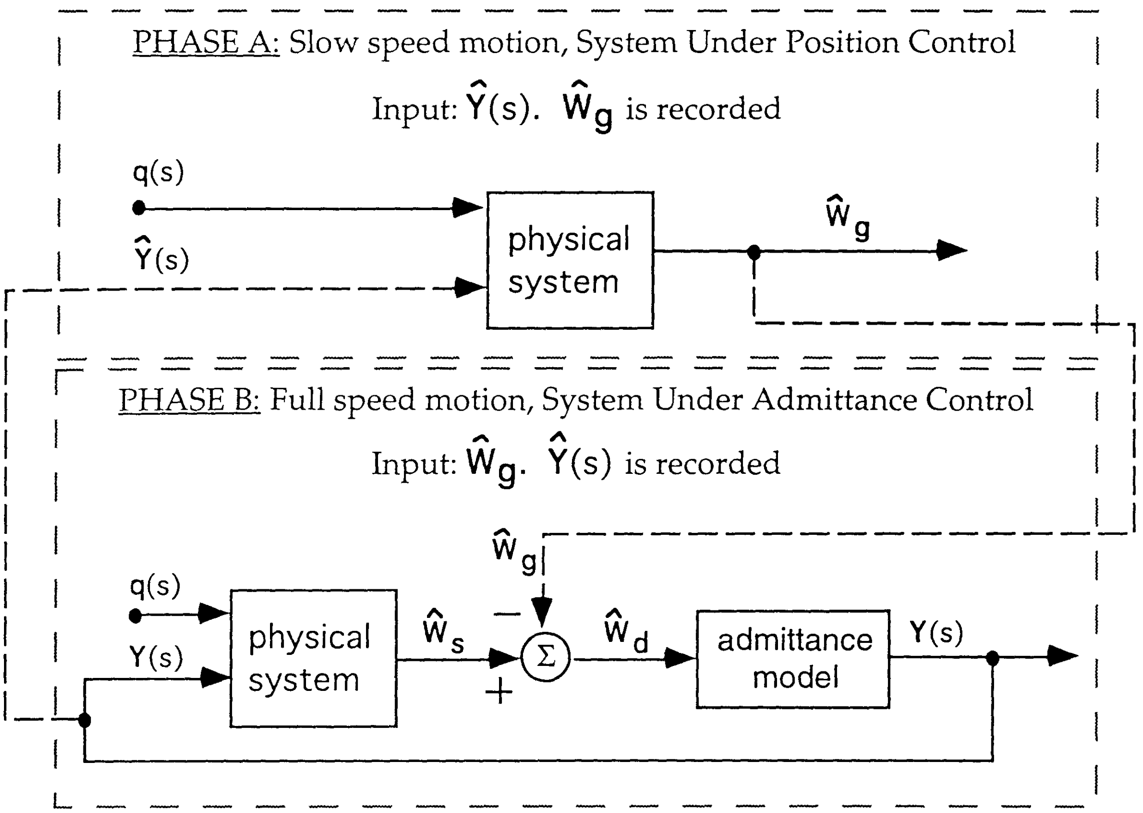
PHASE A: Slow speed motion, System Under Position Control
Input: Ŷ(s). Ŵg is recorded
q(s)
Ŷ(s)
physical system
Ŵg
PHASE B: Full speed motion, System Under Admittance Control
Input: Ŵg. Ŷ(s) is recorded
Ŵg
q(s)
Y(s)
physical system
Ŵs
−
+
Σ
Ŵd
admittance model
Y(s)

Figure 3-3: Learning Algorithm Schematic

If the method converges, it can be shown that the final dynamic wrench $\hat{W}_d^n(s)$ and base motion $\hat{Y}^n(s)$ correspond to micro-gravity conditions. Successive base motion estimates will generally converge quickly to some accuracy. Substantial dynamic wrench errors may result in the platform trying to move outside its workspace when there are large errors in the initial base motion guess. In these cases the VES safety systems will abort the procedure.

This iterative method is similar to a method used to learn all the static and dynamic mass parameters of a manipulator to improve the accuracy of manipulator motions [Arimoto et. al. 1984]. The convergence characteristics of the Learning Method are also similar to the method presented by Arimoto.

The following subtleties also apply to the Learning Method. First, the motion of the manipulator does not have to be known accurately: only the commands to the manipulator must be known and repeatable. The actual micro-gravity motion of the manipulator joints will converge along with the base motion. Second, for some cases, the initial guess of no base motion may be replaced by some other trajectory, say one based on simulations.

3.3.2 Emulation Accuracy

The Learning Method was used to emulate micro-gravity on the VES. Once again, the system idealized in Figure 2-5 and described in Section A.2 was emulated with a PUMA 560 mounted on the VES. The PUMA was commanded to move its arm through the same 180 degrees of motion during repeated iterations of the learning method. After nine iterations of the learning algorithm the micro-gravity motions of the manipulator base converged to less than a millimeter, or less than .001 radians in each axis. The convergence of the motion in successive iterations for rotations about the $\mathbf{X}_i$ axis and the $\mathbf{Z}_i$ axis of the manipulator base is shown in Figure 3-4.

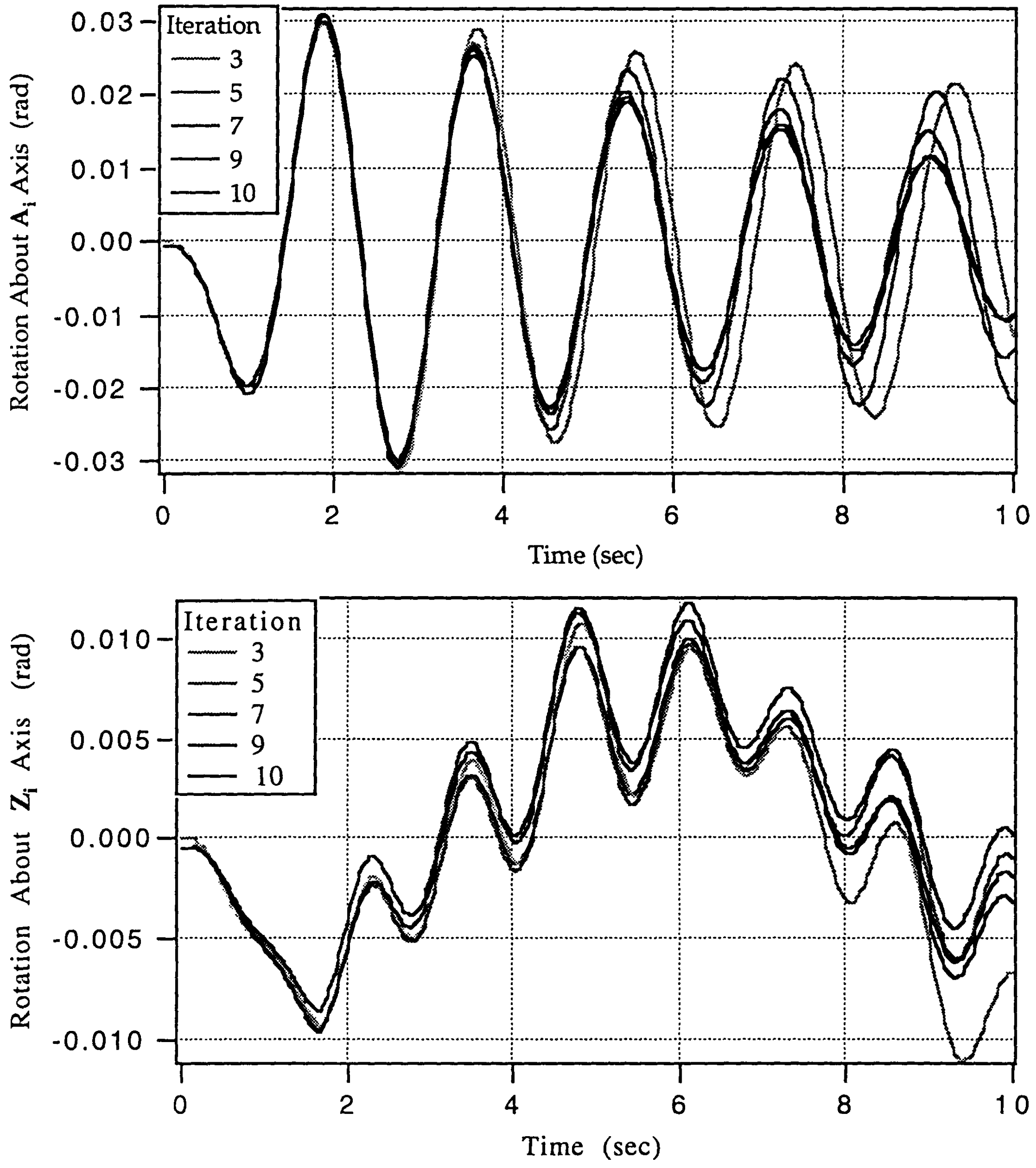

Figure 3-4: Rotation of Base During Learning Iterations

3.4 Model Method Gravity Compensation

The model based method analytically formulates the wrench due to gravity at the base of a manipulator, which is uniquely determined by its mass parameters, joint angles and base orientation. The basic analytical formulation was proposed by [West et. al 1989], with no experimental results. The method presented here requires experimentally finding the manipulator mass parameters very accurately. With the analytical relationship and the mass parameters, $\mathbf{W}_g$ can be calculated, allowing the VES to compensate for gravity and emulate micro-gravity without a priori knowledge of the system inputs. This permits studies such as telerobotic experimentation or human supervisory control.

3.4.1 Determining Mass Parameters

Mass parameter identification is the key to accurately predicting the force and moment at the base of a manipulator due to gravity. Several algorithms have been developed to experimentally determine the mass and inertial parameters of manipulators [Mayeda et al. 1984, Olsen et al. 1985, Mayeda et al. 1988]. These methods use motor torque information to solve for the dynamic parameters, which are generally used in feed forward or computed torque control of the joints. These methods are limited to manipulators with low joint friction, such as direct drive. Regardless, many of the parameters found are not required for space emulation, and the lowest, undriven, link is not modeled. Mass parameters can be found by disassembly and measurement of the manipulator [Armstrong et al. 1986]. This method is tedious, and does not account for variations in the manipulator.

A method of experimentally determining mass parameters of a manipulator is presented. The parameters found are used to predict gravity forces and moments exerted at the base of the manipulator. Experimentally finding the mass parameters of the manipulator allows an arbitrary manipulator to be quickly modeled and then used in an emulation.

3.4.2 Formulating the Model

The analysis that follows is presented for a single serial link manipulator system whose base is capable of being positioned accurately in inertial space. The geometry and Denavit-Hartenburg parameters of a PUMA 560 are presented in Appendix B, and the development of this mass parameter analysis for the PUMA 560 is presented in Appendix C.

Consider a stationary general manipulator with n links oriented arbitrarily in inertial space in order to develop a model of manipulator mass parameters. Applying elementary laws of statics, the gravitational wrench at the base of the general manipulator can be written:

$$W_g = \begin{cases} F_g = \sum_1^n (m_i)\{{}^b g\} = (M_{total})\{{}^b g\} & (3.3a) \\ M_g = \sum_1^n \{{}^b r_i\} \times \{{}^b g\}(m_i) & (3.3b) \end{cases}$$

where m_i is the mass of link "i", ${}^b g$ is the gravitational force vector transformed to the coordinate frame of the manipulator base, and ${}^b r_i$ is the position vector to the i^{th} link's center of mass from the manipulator base coordinate frame, expressed in the manipulator base frame.

The inertial orientation of the base of the manipulator is defined by the Z-Y-X constant angle (roll-pitch-yaw) convention [Craig 1989]. The transformation matrix for this convention can be used to write the gravitational force vector in the manipulator base frame as:

$$ {}^b g = \begin{Bmatrix} gx \\ gy \\ gz \end{Bmatrix} = [T_{XYZ}]^T \begin{Bmatrix} 0 \\ 0 \\ -g \end{Bmatrix} = -g \begin{Bmatrix} -\sin\phi_Y \\ \sin\phi_X \cdot \cos\phi_Y \\ \cos\phi_X \cdot \cos\phi_Y \end{Bmatrix} \qquad (3.4)$$

where ϕ_X, ϕ_Y and ϕ_Z are the roll, pitch, and yaw of the manipulator base in the inertial frame, shown in Figure 2-4. The manipulator base is mounted accurately on the top of the VES platform in our experimental system; hence the manipulator base inertial orientation is known by the VES system. The mass parameter constants, m_i and ${}^b\mathbf{r}_i$ for each link, are not known.

The manipulator model and the method for experimentally finding the model are based on Equations 3.3 and 3.4. The model has two parts; one for predicting gravity forces, Equation 3.3a, and one for moments, Equation 3.3b.

3.4.3 Estimating Gravity Forces

Estimating the gravity forces at the base of the manipulator requires finding the total mass of the manipulator, M_{total}, and using Equation 3.3a. An estimate for M_{total} could be formed from one force sensor measurement at a known platform orientation, essentially weighing the manipulator. Unfortunately, small errors in the sensor or orientation could lead to large errors in subsequent force predictions by this method. A better approach is to average out the effects of small random errors. A large sample of m force measurements is collected at various orientations and the corresponding gravitational accelerations are calculated by Equation 3.4. A minimization of the errors can then be achieved in a fashion similar to the pseudo-inverse or least squares approaches. Individual estimates for M_{total} are weighted by their magnitudes and averaged, producing a best estimate for M_{total} according to:

$$M_{total} = \frac{\left\{{}^b\tilde{g}\right\}^T \left\{\tilde{F}_s\right\}}{\left\{{}^b\tilde{g}\right\}^T \left\{{}^b\tilde{g}\right\}} \tag{3.5}$$

where ${}^b\tilde{g} = \left[\left\{{}^bg(1)\right\}^T \ \left\{{}^bg(2)\right\}^T \ \ldots \ \left\{{}^bg(m)\right\}^T\right]^T$ is a vector composed of m gravity force vectors in the manipulator base frame, and

$\tilde{F}_s = \left[F_s(1)^T \ F_s(2)^T \ \ldots \ F_s(m)^T\right]^T$ is a vector composed of the m sensor force vector measurements.

The M_{total} found is the only model parameter needed to predict the forces due to gravity.

3.4.4 Estimating Gravity Moments

The position vector of each link's center of mass in that link's coordinate frame, $\mathbf{r}_i$, is a mass parameter constant of the manipulator. The position vector to each link's center of mass from the manipulator base frame, ${}^b\mathbf{r}_i$, can be found with a transformation matrix:

$$ {}^b\mathbf{r}_i = \left[{}^b_i A\right] \cdot \mathbf{r}_i \qquad (3.6)$$

This transformation is shown for joint two of a PUMA 560 in Figure 3-5. Note that both ${}^b g$ and $\left[{}^b_i A\right]$ are configuration dependent (knowns) while r_{ij} and m_i are the mass parameter constants of the manipulator (unknowns).

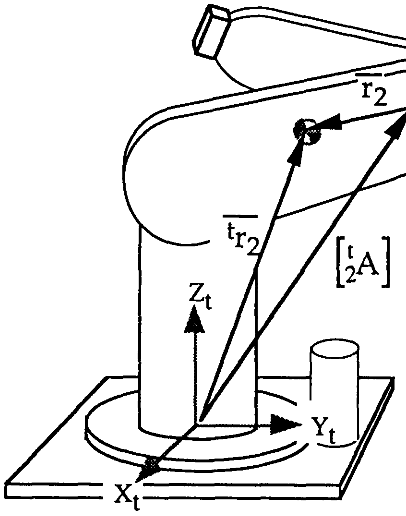

Figure 3-5: Link “i” center of mass vector

The transformation of Equation 3.6 can be used to rewrite Equation 3.3b, the moment at the manipulator base caused by gravity:

$$M_g = \sum_{i=0}^{n} \begin{bmatrix} 1 & 0 & 0 & 0 \\ 0 & 1 & 0 & 0 \\ 0 & 0 & 1 & 0 \end{bmatrix} \cdot \left[{}^b_i A\right] \cdot \begin{Bmatrix} r_{ix} \\ r_{iy} \\ r_{iz} \end{Bmatrix} \times (m_i) \cdot \begin{Bmatrix} {}^b g_x \\ {}^b g_y \\ {}^b g_z \end{Bmatrix} \qquad (3.7)$$

where $\{r_{ix}\ r_{iy}\ r_{iz}\}^T$ is the position vector for the link "i" center of mass in the link "i" coordinate frame, and

$\left[{}^b_i A\right]$ is the homogeneous transformation matrix from the i^{th} link frame back to the manipulator base frame.

Equation 3.7 can be expanded to produce three equations for the gravity moment (for the three axes) with 4n+1 terms in each of the three axes. Recall that n is the number of links. This calculation is shown for the PUMA 560 in Appendix C. The constant mass parameter terms ($m_0 \bullet r_{0x}$, $m_0 \bullet r_{0y}$...) can be factored out as a 3(n+1) by 1 vector, **Q**, leaving the equation in a simplified linear matrix form:

$$\mathbf{M_g} = \left[W(\mathbf{q},\Phi)\right] \left\{\mathbf{Q}\right\}. \tag{3.8}$$

where the matrix $\left[W(\mathbf{q},\Phi)\right]$ is a function of joint angles and manipulator base orientations of dimension 3 by 3(n+1).

Matrix $\left[W\right]$ is a function of the inputs, while **Q** is a function of the constant mass properties. Expressions for both $\left[W\right]$ and **Q** for a PUMA 560 are shown if Appendix C. Physically, each term in **Q** represents a link mass times a moment arm for some link axis, such as '$m_1 \cdot r_{1z}$'. Link lengths and offsets produce an extra term in the elements of **Q** which are aligned with the offset or link length, such as '$m_2 \cdot r_{2z} + (m_2+m_3) \cdot d_2$'. The base of the manipulator is treated as an extra link since it has mass which is offset from the ideal manipulator base, causing some moment.

The columns of $\left[W\right]$ contain gravity acceleration components which combine with a "mass times moment arm" element from **Q** to produce the gravitational moment. Since each revolute joint axis is defined in space by only two angles, one of the three columns added to $\left[W\right]$ for that link will be proportional to a previous column, or identical for orthogonal joints. In other words, the gravity acceleration component for one axis of each link will be aligned with an axis from the previous link. Prismatic joints will have two axes similarly aligned. This alignment causes identical acceleration components which appear as linearly dependent columns in the $\left[W\right]$ matrix. Subtracting dependent columns produces :

$$M_g = \left[G(q,\Phi)\right] \{P\}. \tag{3.9}$$

where $\left[G(q,\Phi)\right]$ is a new configuration dependent matrix of dimension 3 by 3 +2(# revolute joints) + (# prismatic joints), and **P** is a mass parameter vector of matching dimension.

The vector **P** is the model of the manipulator necessary for predicting gravitational moments. Although each element of **P** contains several constants, only their sum is required, producing a simplified model of the manipulator .

Equation 3.9 could be solved for **P** by collecting a minimal set of independent $\left[G\right]$ matrices and $\mathbf{M}_g$ vectors to create a linear set of equal equations and unknowns. This method produces poor results, since it is very sensitive to small errors as we found in estimating forces. A better approach is the least squares solution. The vector which minimizes the squared error $\left\|[A]\{\mathbf{x}\}-\{\mathbf{b}\}\right\|^2$ for the linear equation $[A]\{\mathbf{x}\}=\{\mathbf{b}\}$ is:

$$x_{\mathbf{best}} = \left[[A]^T[A]\right]^{-1}[A]^T\{\mathbf{b}\}, \tag{3.10}$$

where the $\left[[A]^T[A]\right]$ matrix is invertible if and only if $\left[A\right]$ has independent columns. The least squares approach allows a large data sample to minimize the errors over the entire equation range.

Since our geometry dependent matrix $\left[G\right]$ has independent columns, we can compose a least squares solution in the form of Equation 3.10. We calculate $\left[G(i)\right]$ matrices at m unique configurations and combine them to form:

$$\left[\tilde{G}\right] = \left[\left[G(1)\right]^T \ \left[G(2)\right]^T \ \ldots \ \left[G(m)\right]^T\right]^T. \tag{3.11}$$

The m corresponding sensor moment vector measurements are combined producing:

$$\tilde{\mathbf{M}} = \left[\mathbf{M}(1)^T \ \mathbf{M}(2)^T \ \ldots \ \mathbf{M}(m)^T\right]^T. \tag{3.12}$$

We then solve:

$$\mathbf{P} = \left[\left[\tilde{G}\right]^T \left[\tilde{G}\right]\right]^{-1} \left[\tilde{G}\right]^T \left\{\tilde{\mathbf{M}}\right\}, \tag{3.13}$$

where **P** is the best estimate of a model which can be used to predict gravity moments by Equation 3.9.

Together, estimates of **P** and M_{total} form the minimal model parameters required to predict the forces and moments due to gravity at the base of a manipulator.

3.4.5 From Theory to Application

The preceding analysis suggested a procedure for estimating the mass parameters, **P** and M_{total}, which could then be used to estimate the gravitational forces and moments by Equations 3.3a and 3.9. Unfortunately, achieving experimental results which met the strict requirements of Section 3.2.3 was more difficult.

Analysis revealed that the experimental estimation procedure was very sensitive to errors in the force sensor calibration matrix. The calibration matrix converts the signal from the force sensor into actual force and moment readings in SI units:

$$^{s}W_{app} = \left[C\right] W_{sig}, \tag{3.14}$$

where ${}^{S}W_{app}$ is the wrench (in SI units) applied to the force sensor in the sensor frame (Appendix D defines the sensor frame and conversion to the platform top frame),

W_{sig} is the wrench signal read from the strain gauge attenuation circuitry via the analog to digital converter, and

$\left[C\right]$ is the calibration matrix.

An estimate of the calibration matrix can be constructed from the manufacturers data and a measurement of the gains of the strain gauge amplifiers. Unfortunately, the accuracy of the manufacturers estimate is unknown and the procedure for measuring the amplifier gains is not very accurate. A discussion of the calculation of this matrix can be found in [Baker 1992] and [Kuklinski 1993].

A method was devised for determining the calibration matrix experimentally in a manner similar to the mass parameter estimation routine. If the manufacturer's estimate of the calibration matrix is reasonably good, then the mass parameter estimation of Equation 3.13 should prove equally good. Equations 3.5 and 3.13 can then be used to estimate the gravitational wrench. This wrench estimate can be used for ${}^{S}W_{app}$ in Equation 3.14. An experimental estimate of the calibration matrix can then be found by combining six wrench estimates, ${}^{S}W_{app}$, and six signals from the sensor, W_{sig}, and solving Equation 3.14. Once again, a least squares approach with a large sample of data across the entire workspace of the platform and manipulator will produce the best result.

The platform and manipulator are commanded to "m" different configurations. At each configuration "j", Equations 3.5 and 3.13 produce an estimate of the applied wrench, ${}^{S}W_{app}(j)$. These are combined to form:

$$\left[\tilde{W}_{app}\right] = \left[W_{app}(1)\ W_{app}(2) \ldots W_{app}(m)\right]. \qquad (3.15)$$

Similarly, at each configuration "j" the signals from the force sensor are also recorded and combined, making:

$$\left[\tilde{W}_{sig}\right]=\left[\mathbf{W_{sig}}(1)\ \ \mathbf{W_{sig}}(2)\ \ \ldots\ \ \mathbf{W_{sig}}(m)\right]. \tag{3.16}$$

A least squares solution can then be written:

$$[C]=\left[\tilde{W}_{app}\right]\cdot\left[\tilde{W}_{sig}\right]^{T}\cdot\left[\left[\tilde{W}_{sig}\right]\cdot\left[\tilde{W}_{sig}\right]^{T}\right]^{-1}. \tag{3.17}$$

By alternately re-estimating the calibration matrix and the mass parameters, it was found that they converged quickly to within some range. Unfortunately, this still resulted in several Newtons or Newton-meters of error which was unacceptable.

Experimentation showed that the range of the wrench convergence was roughly equal to wrench errors due to inaccuracies in the knowledge of the platform position. The original procedure was to command the platform to a position and then freeze it. It was assumed that the platform accurately maintained its position. Gravity estimation, however, is very sensitive to the base orientation of the manipulator, so even errors of half a degree were unacceptable. This problem was solved by improving the coordination between the two control computers to allow the platform to remain under position control while the wrench measurements were made.

When the platform position was known accurately, the iterative process of estimating a calibration matrix and mass parameters was repeated. This time the errors in gravity force prediction were reduced much farther, very close to the range of errors found in the force sensor itself. Some improvement was made in the noise errors of the force sensor (see Appendix F) yet it remains the dominating source of error in accurate gravity compensation.

3.4.6 Emulation Accuracy

The first step in emulating a gravity free system is to model the manipulator. Estimates for M_{total} and the $\mathbf{P}$ vector were found for a PUMA 560 by the method described above. The manipulator and VES platform were moved through a series of 47 positions. in each configuration "j": a geometry matrix $[G(j)]$ was calculated from the measured platform orientation and robot position, a gravity vector ${}^{b}\mathbf{g}(j)$ was formed from orientation information, and measurements $\mathbf{F_s}(j)$ and $\mathbf{M}(j)$ were collected. The data from all configurations was combined to form a $[\tilde{G}]$ matrix, a ${}^{b}\tilde{\mathbf{g}}$ vector, an $\tilde{\mathbf{M}}$ vector, and an $\tilde{\mathbf{F}}_{\mathbf{s}}$ vector as described above. A manipulator model was then formed by solving Equations 3.5 and 3.13 for M_{total} and $\mathbf{P}$.

The mass parameter estimates found were then used to find an improved estimate for the calibration matrix. The system was commanded through the same series of 47 positions. Vectors of ${}^{s}\mathbf{W}_{\mathbf{app}}(j)$ and ${}^{s}\mathbf{W}_{\mathbf{sig}}(j)$ were collected at each position "j". These were combined to form the matrices $\left[\tilde{\mathbf{W}}_{\mathbf{sig}}\right]$ and $\left[\tilde{\mathbf{W}}_{\mathbf{app}}\right]$. A best estimate for $[C]$ was then generated from Equation 3.16.

After two iterations of this procedure, estimates of the gravitational wrench were accurate to within the required range. Further iterations did not significantly improve the accuracy, although the values for the mass parameter estimate and $[C]$ changed by a few percent. The mass parameter estimates found in this way were similar to physical mass parameter measurements, see Section C.3.

To check the accuracy of the gravity wrench estimates, the model was used to predict gravity wrenches over the range of motion of the system. This predicted value, and the actual sensor readings were collected for several very slow movements of the manipulator and the base which had negligible dynamic effect. The manipulator moved joint 1 through the 180 degree rotation described earlier, while the platform was commanded to rotate the manipulator base from +5 degrees to -5 degrees rotation about the inertial X and Y axes. Table 3-1 summarizes the error in $\hat{W}_g$, the difference between estimated and measured values, showing the average and maximum error found in each axis. Figure 3-6 shows the measured and estimated wrenches over the entire motion. The accuracy of $\hat{W}_g$ found with this experimentally identified robot model met the goal set in our sensitivity analysis.

TABLE 3-1: Errors in Gravity Prediction

Axis	RMS. Error	Max. Error
X_b Force	0.46 N	0.95 N
Y_b Force	0.24 N	0.53 N
Z_b Force	0.46 N	1.4 N
X_b Moment	0.62 Nm	1.14 Nm
Y_b Moment	1.01 Nm	1.67 Nm
Z_b Moment	0.06 Nm	0.13 Nm

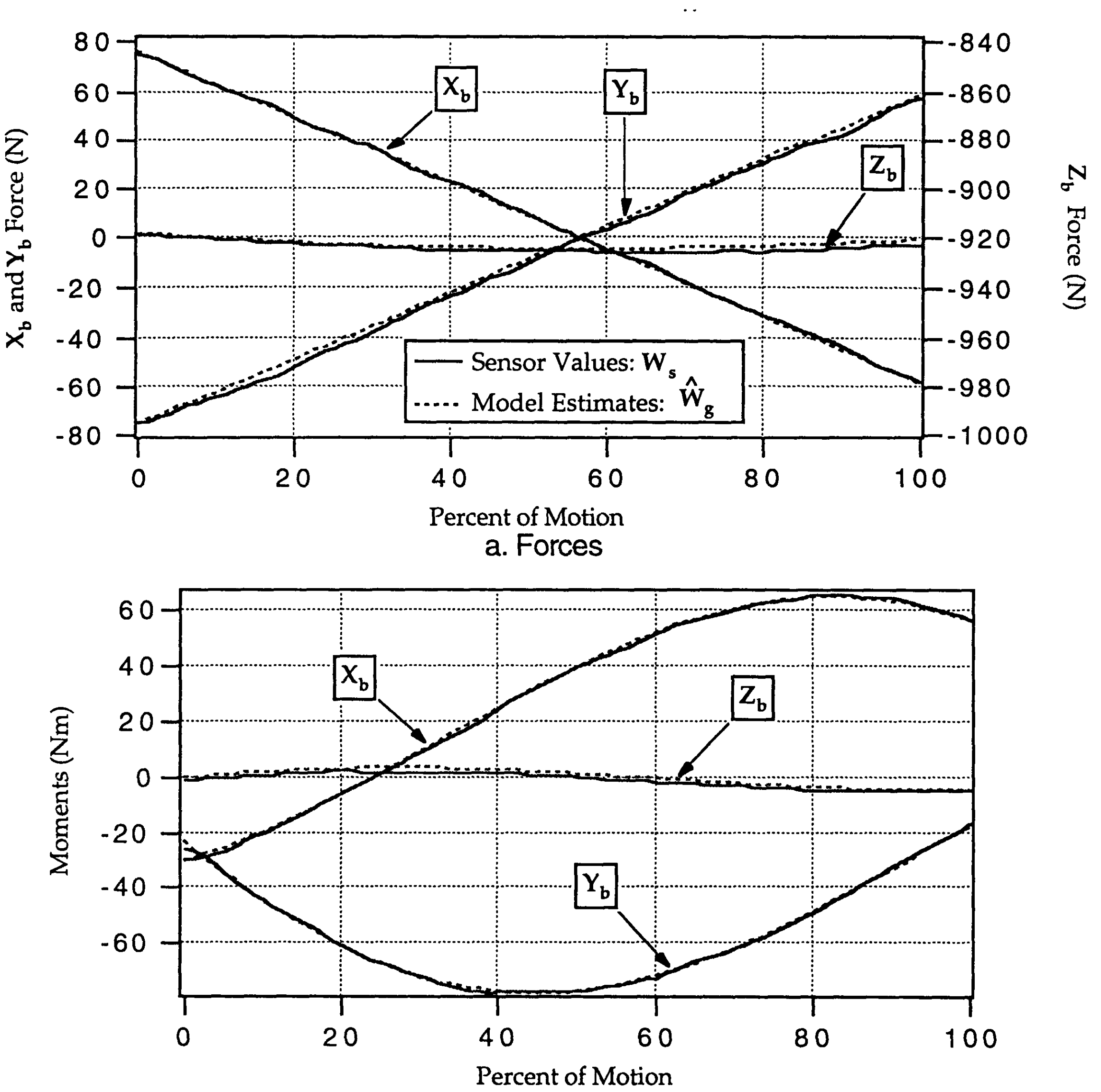

a. Forces

b. Moments

Figure 3-6: Estimated and Actual Gravity Wrench

3.5 Comparison of the Methods

The Learning Method was the first successful method of gravity compensation. Its iterative nature allowed many of the critical error sources to be ignored. Exact knowledge of the robot orientation was unimportant, as long as it was repeatable. Errors in knowledge of the calibration matrix could also be ignored. Only the unrepeatable, high-frequency noise in the force sensor could not be overcome with the Learning Method. Although the Learning Method has a good accuracy and is computationally very inexpensive, it takes quite a bit of time to perform an experiment. Each experiment must be run through several iterations, and half of those iterations are at a very slow, non-dynamic, speed which is generally 1/20th the normal speed. This means that a 20 second experiment can take over 20 minutes to perform just once. Even though the Learning Method could be used to emulate micro-gravity, there was still a need for a more practical, faster method of emulation, in addition to the need to emulate experiments without pre-planned motions.

The basic idea behind Model Method was proposed in 1989 [West et al. 1989]. The most challenging aspect of this method was not theoretical, it was in the application. Accurate knowledge of the robot orientation was very important, as was reduction of the force sensor errors. The final improvement which allowed this method to achieve the high accuracy desired was the estimation of the calibration matrix described in Section 3.4.5.

Figure 3-7 shows the gravity compensated dynamic moment in the $\mathbf{X}_b$ axis for an experiment performed with both the Learning Method and the Model Method. Figure 3-8 shows the close correlation in the base motion produced by the two methods. Both of these methods have been used successfully to verify the effectiveness of path-planning and control algorithms for space robotics in a number of studies, see Chapter 4.

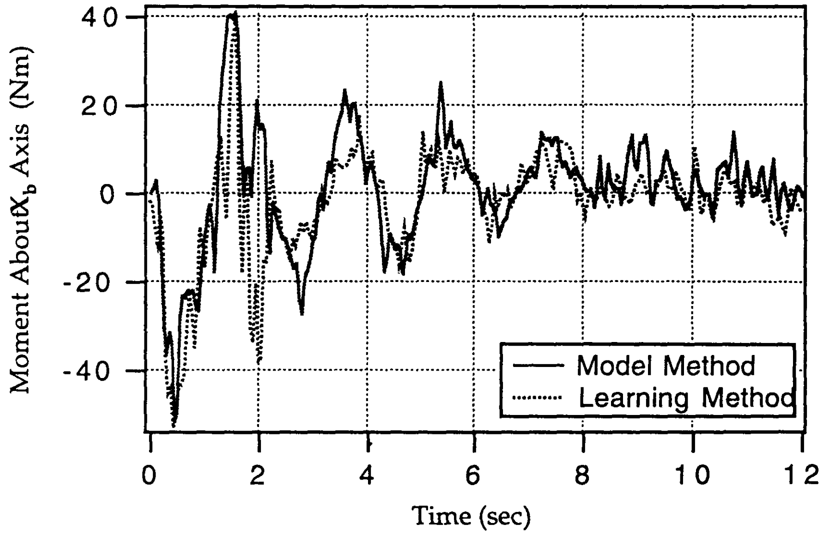

Figure 3-7: Micro-Gravity Moment

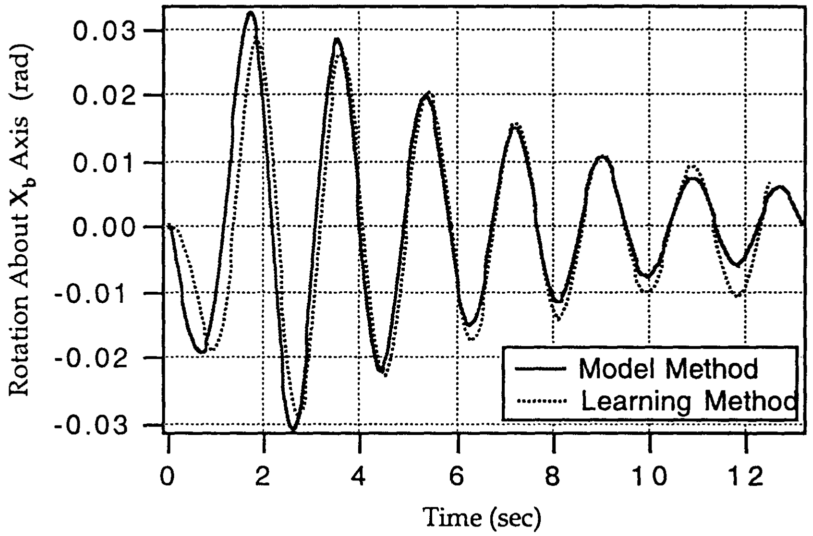

Figure 3-8: Micro-Gravity Rotation

3.6 Summary

This chapter presented the theoretical developments for gravity compensation. The difficulties of estimating the effects of gravity were discussed. Then, two methods were presented to compensate for gravity on the VES II, the Learning Method and the Model Method. Experimental results were presented which showed that these methods can extract even small dynamic forces from the larger gravitational effects to accurately emulate a micro-gravity environment.

Chapter 4

Investigation of Planning and Control Methods

4.1 Introduction

The high cost of space operations and the dangers involved in manned space operations has created a heightened interest in the field of space robotics. Many control theories and manipulator path planning algorithms have been proposed to improve the speed and accuracy of robotic space operations [Papadopoulos and Dubowsky 1993, Xu and Kanade 1993]. The VES system described in the preceding chapters has been used to investigate several of these algorithms experimentally.

A series of algorithms were investigated which deal with one of the fundamental problems of space robotics. A common scenario in space robotics will be the maneuvering of a small dexterous manipulator whose gross positioning is achieved by a less accurate long flexible manipulator, such as the proposed space station scheme the SSRMS. The main problem is the accurate positioning of the small dexterous manipulator. Motions of the small manipulator will excite the low frequency vibrations in the long flexible manipulator, causing the small manipulator to bounce around. In this study, the long flexible manipulator, the base of the dexterous manipulator, is assumed to be a simple flexible beam system.

Two basic algorithms which deal with this vibration problem are investigated. One algorithm, the Coupling Map, is used to minimize the amount of vibration caused during a motion [Torres and Dubowsky 1993]. A second algorithm, called Pseudo-Passive Energy Dissipation (PPED), is used to remove the vibrations once they are caused [Torres 1993]. A third algorithm, which is not presented here, such as Coordinated Jacobian Transpose Control [Sunada 1994] could be used to maintain the end effector in an accurate position despite any vibrations which remain.

4.2 The Coupling Map

A path planning algorithm for a manipulator mounted on a compliant base in zero gravity was proposed by [Torres 1993, Torres and Dubowsky 1993]. The *coupling map* is a tool for finding paths in manipulator joint space which minimize the energy transferred into the compliant base during manipulator motions. Energy transferred to the base causes motion which damp out very slowly, increasing the duration and expense of space operations. This approach would be used to plan the motions of future space robotics systems. The coupling map theory has produced good results in simulation and planar experiments [Torres 1993, Torres and Dubowsky 1993], and is experimentally verified in full spatial motion here.

The coupling map is a function of the compliance and damping characteristics of the base (the long reaching flexible manipulator) as well as the static and dynamic parameters of a manipulator with n joints. Analysis of the system equations of motion with the assumption of small motions and wrenches produces the coupling matrix [Torres 1993]. The coupling matrix, $\left[Q(\mathbf{q})\right]$, is a measure of the sensitivity of the support structure to receiving strain energy from the manipulator in a given manipulator configuration. The eigenvectors of $\left[Q(\mathbf{q})\right]$ suggest joint motion directions of maximum and minimum energy transfer at location $\mathbf{q}$ in joint space. Lines of minimum energy transfer can be drawn in joint space by following the minimum eigenvectors; the magnitude of the eigenvector is represented by the darkness of the line. These lines can be easily visualized for a 2 degree of freedom system with a *coupling map* of minimum energy lines. Higher degree of freedom systems are more difficult to represent visually, cross sectional *coupling maps* can be drawn for any two joints by fixing all others. The disturbance of the base for any manipulator path is shown by the darkness of the lines crossed in the map. Traveling parallel to a line transfers the minimum possible energy to the base in that region. Darker regions are called high coupling areas while lighter regions are low coupling areas.

Figure 4-1 shows three cross sectional Coupling Maps for a PUMA 560 on the two link beam structure described in Appendix A. These maps form three faces of one quadrant of the manipulators joint space, the orientation of this quadrant is also shown in Figure 4-1. For this system the symmetry of the joint 1 axis resulted in nearly vertical low coupling lines on the faces B and C for any orientation of joints 2 and 3. This simplified the path finding task, since paths could be generated for each surface of the cube almost independently. With arbitrary initial and final end effector positions, I and F, two paths are superimposed on this map. The "Bad Path" crosses over many dark lines, high coupling areas, while the "Good Path" passes through the lighter lines, low coupling areas, and travels parallel to the lines in high coupling areas. Following minimum energy lines and avoiding high coupling regions is called the Hot Spot

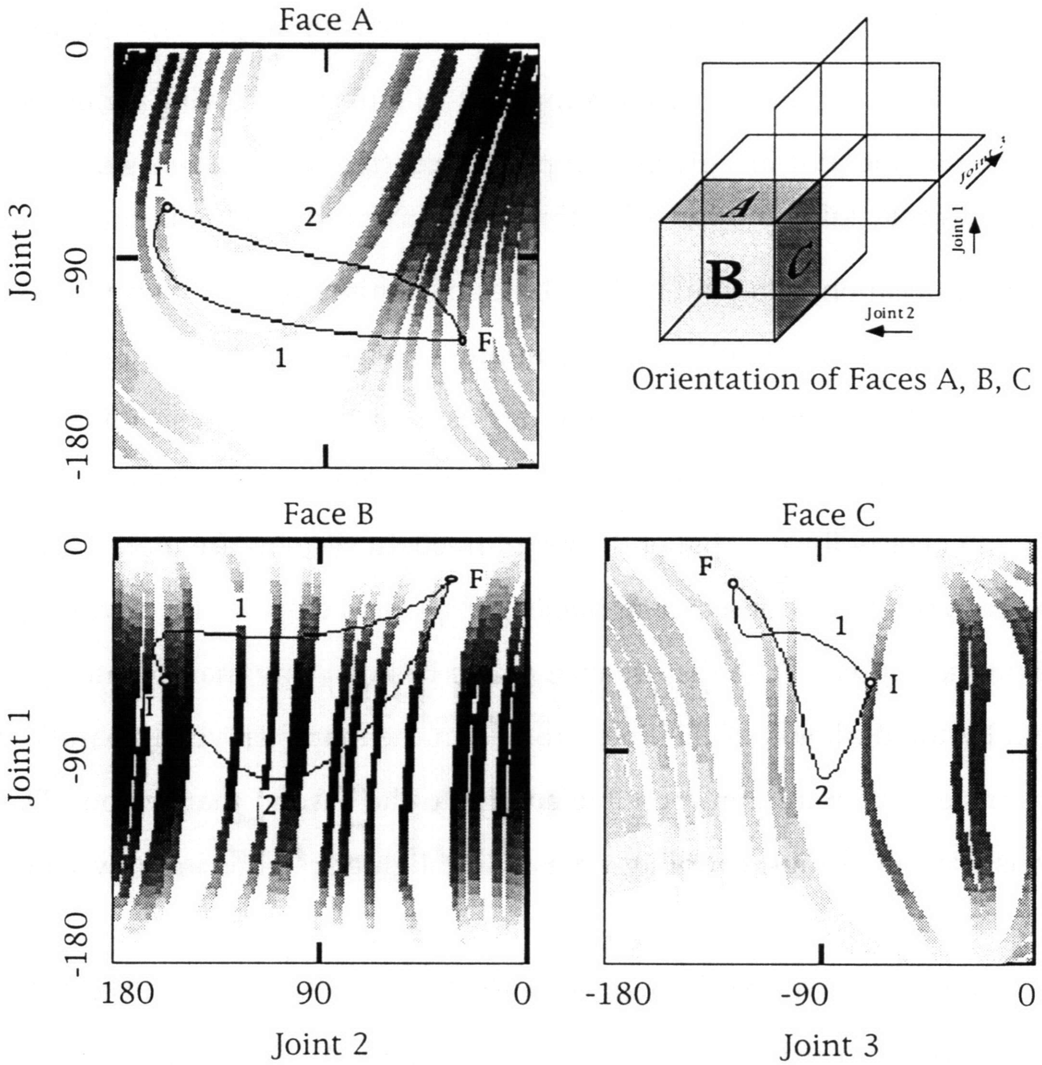

Figure 4-1: Coupling Map Cross Sections for PUMA 560 on Flexible Beam

Method. The theory suggests that the "Bad Path" would transfer more energy into the flexible beam and disturb it more than the "Good Path".

The VES system was used to emulate the flexible beam system while removing the effects of gravity with the model based method. The PUMA 560 was moved along the "Bad Path" and "Good Path" and the motions of the manipulator base on the emulated flexible beam were recorded. To represent the motion of all six axes clearly, the total energy transferred to the supporting structure was calculated by $E_{ij} = \frac{1}{2} \cdot k_{ij} \cdot \Delta x_i \cdot \Delta x_j$ for each element ij of the spring matrix which modeled the elasticity of the beam. This energy is shown for both paths in Figure 4-2. Clearly path 1, the low coupling path, caused much less motion and transferred less energy into the flexible structure than path 2, as the Coupling Map theory suggested.

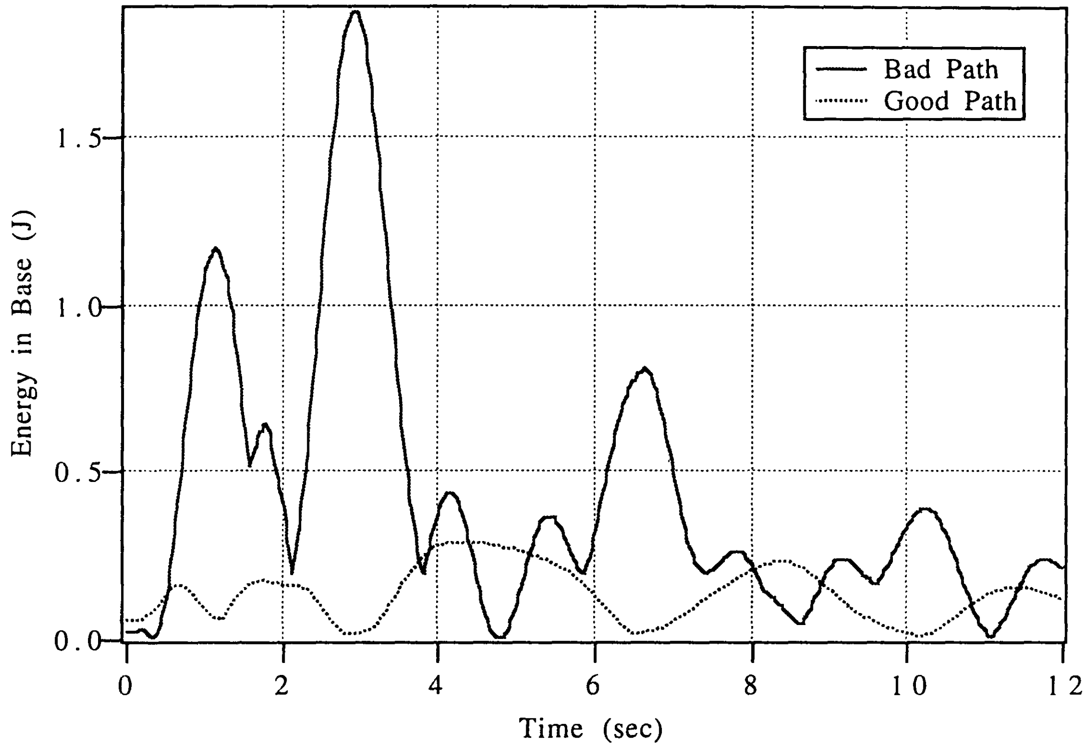

Figure 4-2: Energy Transferred to the Flexible Beam for Two Motions

For comparison, Figure 4-3 shows the "Good Path" without the gravity compensation routines along with the paths of Figure 4-2. Clearly the data is corrupted by gravity, making a meaningful experiment impossible.

Computer algorithms can also be used to search high order coupling maps for good paths.

These experimental results demonstrate the effectiveness of the Coupling Map for selecting manipulator paths that reduce the vibration of a system's flexible base and reduce the duration of space operations.

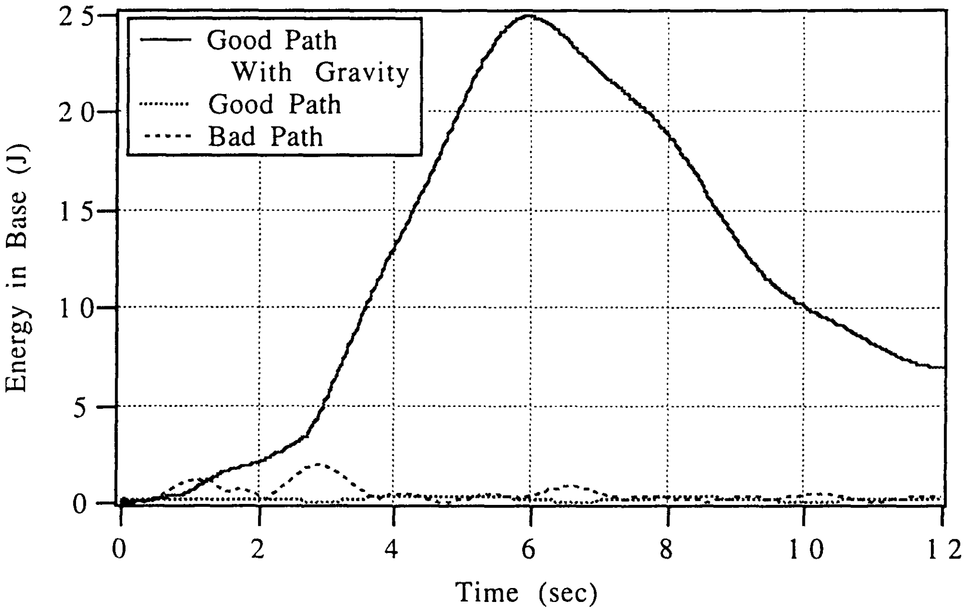

Figure 4-3: Energy Transferred to Beam With and Without Gravity

4.3 Pseudo-Passive Energy Dissipation

When vibrations exist in a long flexible beam system which is supporting a dexterous manipulator, the manipulator itself can be used to damp out the vibrations. An algorithm has been proposed which tunes the manipulators joint controller gains to act as passive spring and damper elements to damp out the vibrations [Torres 1993]. This method is called Pseudo-Passive Energy Dissipation or PPED.

The basic PPED concept is very simple. The joint controller gains are tuned to values which maximize the damping in the combined manipulator and base system. The damping of energy works best if the manipulator is in a configuration where the strain energy of the base is sensitive to small joint motions. The Coupling Map Algorithm can be used to find these configurations. For some systems, a concept known as the Virtual Manipulator can be used to simplify the calculation of the best PPED gains [Torres 1993]. For many systems, however, PPED requires calculating the full dynamic model of the manipulator and its base structure.

4.3.1 The Virtual Manipulator Simplification

The virtual manipulator concept simplifies the analysis of space robotic systems by allowing a manipulator to be modeled by a single mass with massless links [Vafa 1987, Vafa and Dubowsky 1990]. This development is based on applying the conservation of angular momentum principle to an arbitrary free-floating manipulator.

A virtual manipulator can be constructed for any free floating robotic system. The total mass of the manipulator is represented at the center of mass of the system, and is called the virtual base. For a true free floating system, the virtual base would remain stationary despite manipulator motions. Virtual links connect the virtual base to the manipulators end effector. These links are always parallel to the original links, and revolute joints always have the same angular rotation as the actual joint (virtual prismatic joint motions are related to but not the same as the originals). The lengths of the virtual links are calculated simply as the ratio of mass in the present link and all previous links to the total mass in the manipulator. Section B.5 shows the construction of a virtual manipulator for a PUMA 560.

A virtual manipulator can also be constructed to go from the virtual base to any point on the actual manipulator. For PPED analysis, it is convenient to construct a virtual manipulator from the virtual base to the base of the actual manipulator. Section B.5 also shows this construction for a PUMA 560.

Once the manipulator is modeled by its virtual manipulator the analysis to find gains which maximize the system damping is quite simple. Figure 4-3 shows a manipulator and base system, and a simplified model which includes a virtual manipulator. Also shown in Figure 4-3 is an even more simplified model of the system where the manipulator is replaced by a simple spring and damper. A state space representation of the most simplified system can easily be constructed. The values for the K_i's and B_i's can then be varied in an iterative process which finds the gains K_d and B_d that produce the maximum damping in the total system.

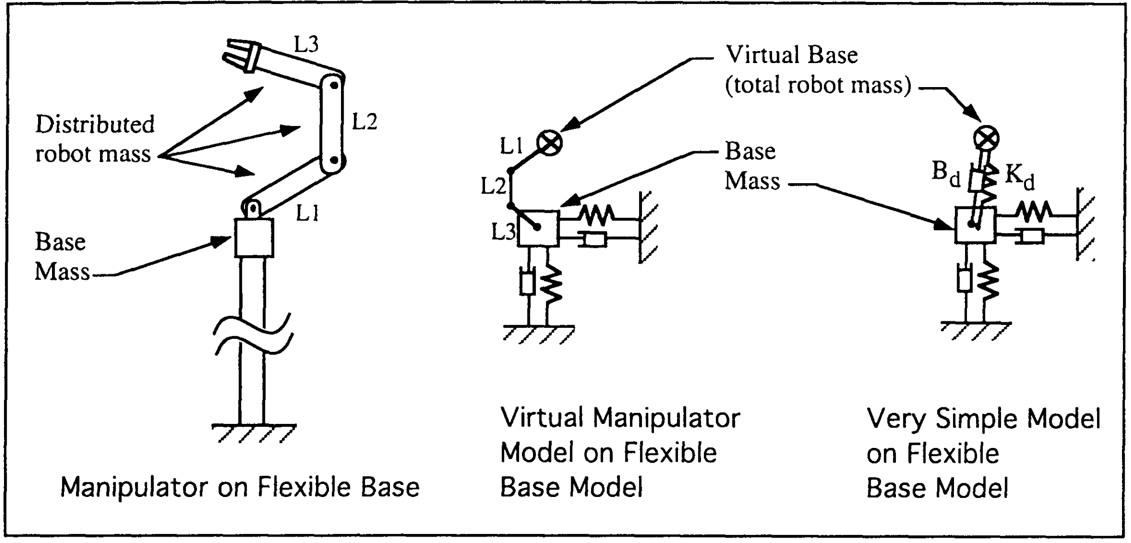

Manipulator on Flexible Base

Virtual Manipulator Model on Flexible Base Model

Very Simple Model on Flexible Base Model

Figure 4-3: Virtual Manipulator Modeling Concept

The K_d and B_d found can be easily converted to actual manipulator gains. First the Cartesian space K_d and B_d must be converted to the virtual manipulator joint proportional and derivative gains. Since the virtual manipulator has as its end point the base of the supporting structure, the K_d and B_d are actually desired end point compliance and damping values for the virtual manipulator. The desired K_d and B_d values can be realized with the endpoint compliance control method [Asada and Slotine 1986]. The standard analysis produces:

$$[K_{vm}] = [J_{vm}]^{T} \cdot [K_d] \cdot [J_{vm}] \tag{4.1}$$

$$[B_{vm}] = [J_{vm}]^{T} \cdot [B_d] \cdot [J_{vm}] \tag{4.2}$$

where $[K_{vm}]$ is a matrix of desired proportional gains for the virtual manipulator joints,

$[B_{vm}]$ is a matrix of desired derivative gains for the virtual manipulator joints,

$[J_{vm}]$ is the Jacobian matrix for the virtual manipulator.

Since the joints of the virtual manipulator are always parallel to the actual joints and have the same basic geometry, the Jacobian matrix of the virtual manipulator is the same as that of the robot with the virtual manipulator link lengths substituted. For similar reasons, the control gains in the virtual manipulator are the same as that of the actual robot. Therefore, the $[K_{vm}]$ and $[B_{vm}]$ found in equation 4.1 and 4.2 are the actual manipulator PPED gains.

This approach has been used to successfully find gains for a simple two degree of freedom planar space robot on a flexible base in simulation and experimentation [Torres 1993]. Unfortunately, many flexible base systems have significant stiffness in them, this makes them unsuitable for the free-floating assumption that the virtual manipulator concept is based on. The scale of the PUMA 560 robot used for our three dimensional VES experiments requires a flexible base with a significant stiffness to be realistically practical. This suggests that a different approach is required to demonstrate PPED on our system; a full dynamic analysis.

4.3.2 Full Dynamic Analysis

When a space manipulators base structure has significant stiffness in it, the virtual manipulator simplification cannot be used. A more complex full dynamic analysis of the system is required. The concept behind PPED with full dynamic analysis is quite simple, although the calculations are far more complex.

To find the appropriate PPED joint gains that will damp the most energy out of the base, the full linearized dynamics of the combined manipulator and base system must be written. For a complex system this can be quite difficult.

The full linearized dynamic equations for a PUMA 560 on an arbitrary linear admittance model base are written in Appendix G.

The PUMA and base system dynamics are written in the form:

$$\frac{d}{dt}\begin{Bmatrix}\dot{X}\\X\end{Bmatrix}=\begin{bmatrix}A\end{bmatrix}\cdot\begin{Bmatrix}\dot{X}\\X\end{Bmatrix} \tag{4.3}$$

where X = [X, Y, Z, α, β, γ, q1, q2, q3] is the state vector containing the position and orientation of the base and the joint displacements, and

$[A]$ is a state space matrix.

To maximize the damping in the complex system, the damping of the 18 poles of matrix $[A]$ must be maximized. An iterative searching algorithm was written in matlab to search for joint gains which maximize this damping. At each iteration, all 18 poles of the 9 DOF system were found. The damping of each pole, weighted by the relative closeness to the origin, was used to estimate the total system damping. The estimator used was:

$$\text{Damping Estimator} = \sum_{i=1}^{n} \zeta_i \cdot \left[1 - \frac{\omega_i}{\sum \omega_i}\right], \tag{4.4}$$

where n is the number of poles (18),

ζ_i is the damping ratio of pole "i", and

ω_i is the natural frequency of pole "i".

This estimator was maximized interatively as the gains were changed. The values which maximized the damping for a PUMA 560 with desired joint angles of 45°, 0°, 0° mounted on the beam system of Section A.5 were found to be:

$$\left[K_{PPED}\right] = \begin{bmatrix}210 & 0 & 0\\0 & 33 & 0\\0 & 0 & 20\end{bmatrix} \tag{4.5a}$$

$$\left[B_{PPED}\right] = \begin{bmatrix}72 & 0 & 0\\0 & 55 & 0\\0 & 0 & 17\end{bmatrix} \tag{4.5b}$$

where $\left[K_{PPED}\right]$ is a matrix of joint proportional control gains which maximize the system damping, and

$\left[B_{PPED}\right]$ is a matrix of joint derivative control gains which maximize the system damping

The 18 system poles which correspond to the PPED gains of Equation 4.5 being used in the PUMA 560 are shown in Figure 4-4.

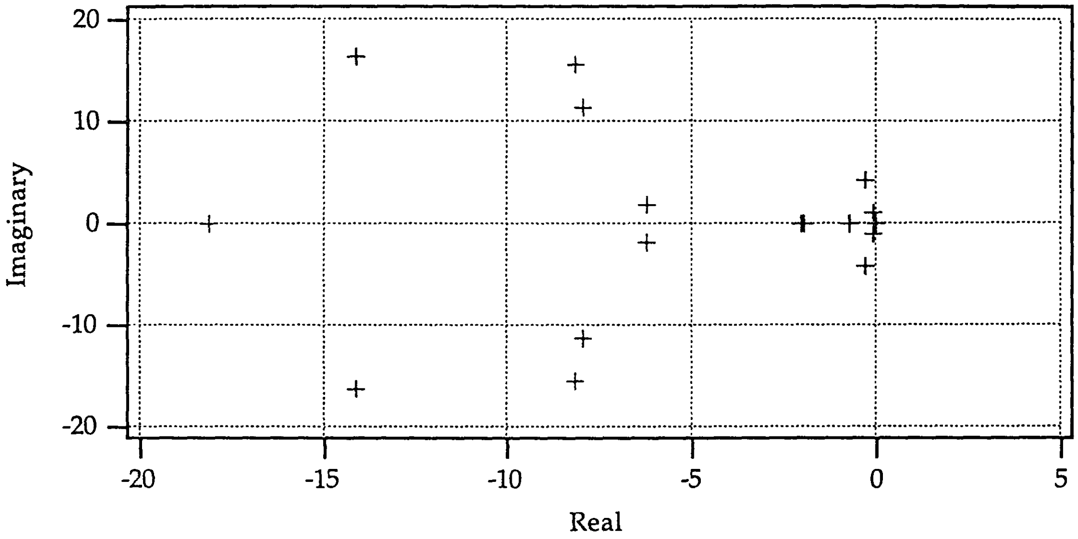

Figure 4-4: System Poles, PPED Gains

Arbitrary large controller gain values were chosen for comparison:

$$\left[K_{high}\right] = \begin{bmatrix} 3000 & 0 & 0 \\ 0 & 2000 & 0 \\ 0 & 0 & 1000 \end{bmatrix} \tag{4.6a}$$

$$\left[B_{high}\right] = \begin{bmatrix} 50 & 0 & 0 \\ 0 & 40 & 0 \\ 0 & 0 & 30 \end{bmatrix} \tag{4.6b}$$

The 18 system poles for these high gain values are shown in Figure 4-5. The four most dominant poles (closest to the origin) were found to be almost completely a function of the supporting base characteristics. These poles are not affected by changes in the manipulator gains. Poles far from the origin correspond to high frequency modes which decay rapidly and have little effect on the system. By comparing Figures 4-4 and 4-5, the poles of primary interest (in the -2 through -5 range) can be seen to move closer to, or onto, the real axis, increasing the damping of those poles and the whole system.

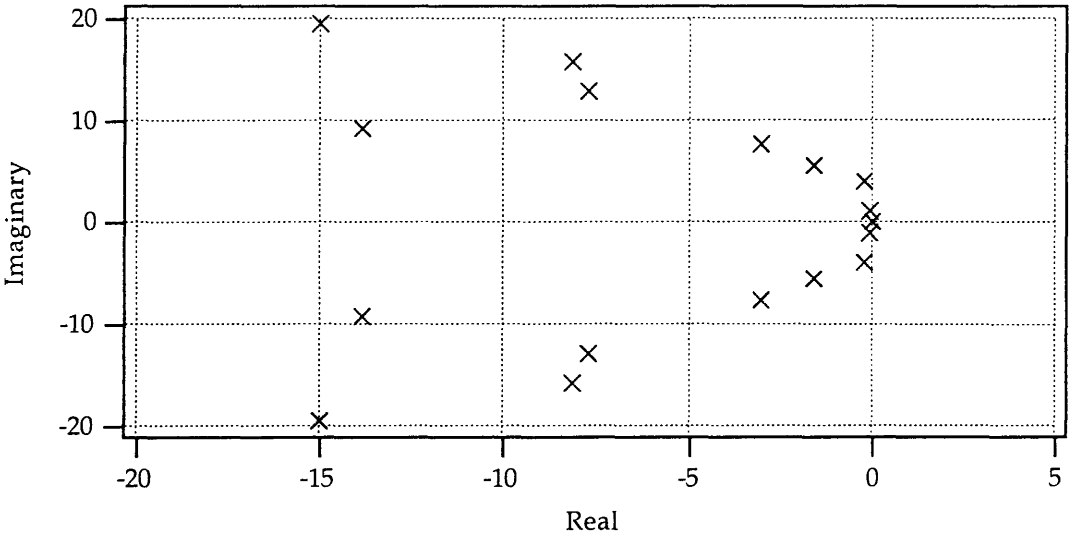

Figure 4-5: System Poles, High Gains

Both the PPED and high joint gains were used in simulations of the PUMA 560 on the flexible beam of Section A.5. In simulation, the base of the manipulator was displaced to an initial position Y(0)= {.1m, .1m, .1m, 0°, 0°, 0°}, where Y(t) is defined in Equation 2.3, and then released. The total translational motion of the base is shown versus time in Figure 4-6 for both the High gains, and the PPED gains. The motion of the base in all six axes was used to calculate the strain energy in the base. Figure 4-7 shows the total strain energy in the base versus time, from a disturbed position with normal high gain values. Also shown in Figure 4-7 is the strain energy for the same disturbance with the PPED gains being used. Clearly the PPED gains allowed the manipulator to passively damp out more of the vibrational energy in the system, reducing the total time it took for the oscillations to die out. The same experiment could be performed experimentally on the VES. Unfortunately, time does not allow the inclusion of experimental results in this thesis.

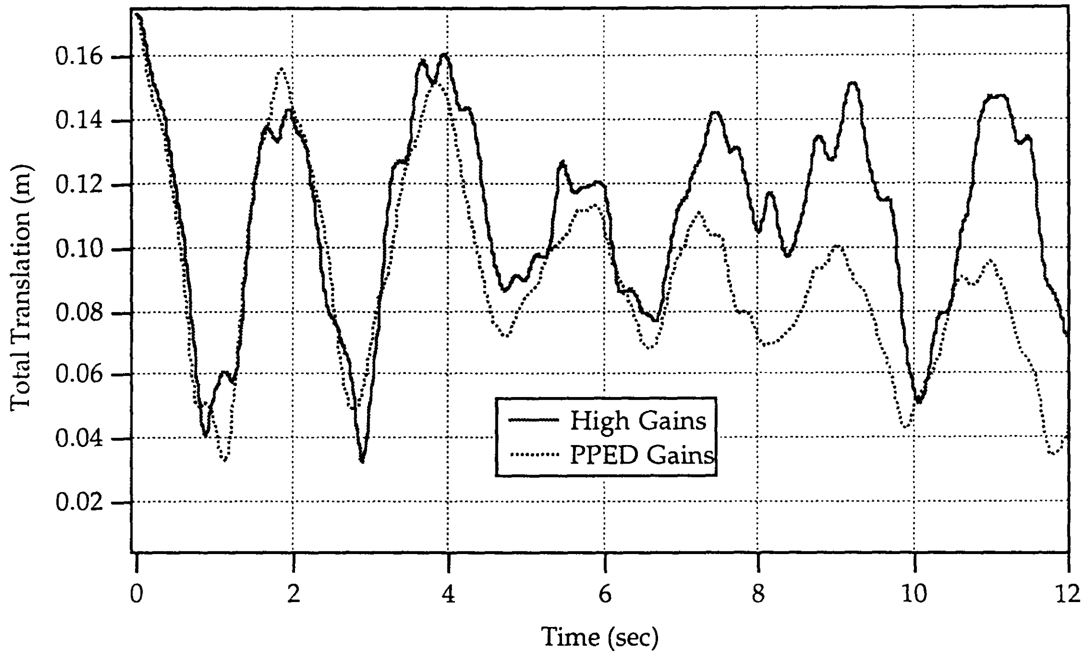

Figure 4-6: PPED Simulation Results, Translation

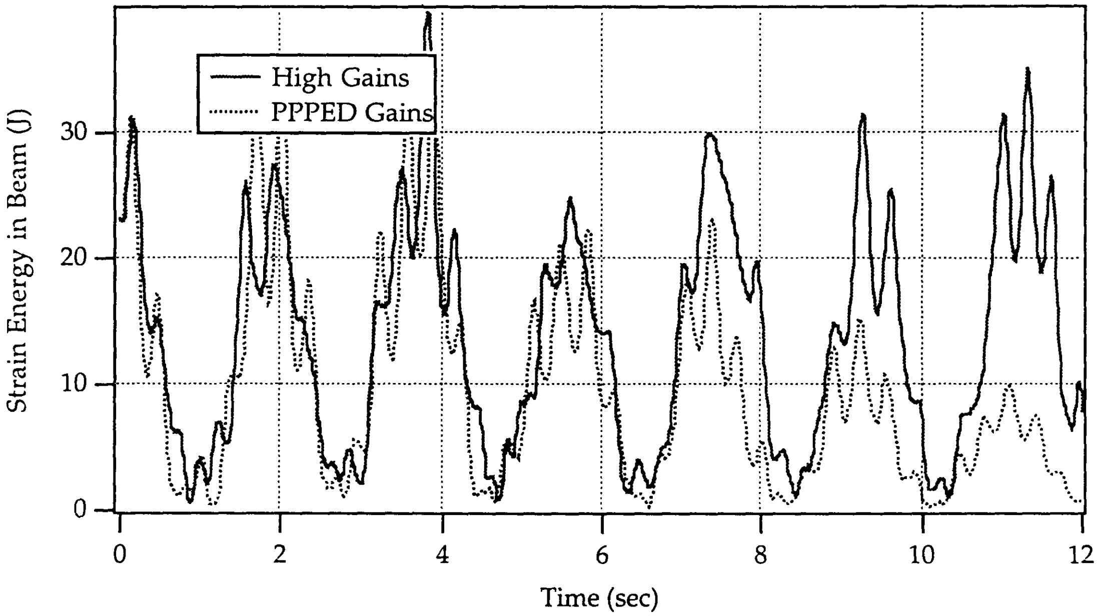

Figure 4-7: PPED Simulation Results, Energy

4.4 Summary

Two algorithms were investigated which address the problem of vibrations in space manipulators on long flexible bases. The Coupling Map algorithm was shown to accurately plan paths which minimize the energy transferred to the flexible base. The Pseudo-Passive Energy Dissipation concept was shown to remove energy from an oscillating beam, allowing the settling time to be reduced for a given disturbance. Both of these algorithms can be used to reduce the time and cost of space robotic operations. Experimental verification of the Coupling Map Algorithm was performed using the gravity compensations routines on the VES.

Chapter 5

Improving System Performance with a Digital Filter

5.1 Introduction

Excessive vibrations of the VES system were encountered during many early attempts to perform experiments. Lowering the bandwidth of the legslave controllers prevented vibrations, but caused further performance problems. An analysis of this problem was conducted, and a digital filter was designed to reduce the occurrence of vibrations and improve the response of the VES system.

5.2 The Performance Problems

The first mode natural frequency of the assembled platform was experimentally determined to be in the neighborhood of 10-13 Hz. This frequency corresponds to transverse vibration of the individual legs, and decreases with increasing length. The frequency of vibrations experienced during operation was measured with an accelerometer attached to one leg, Figure 5-1 shows the frequency range found by a spectrum analyzer. To avoid

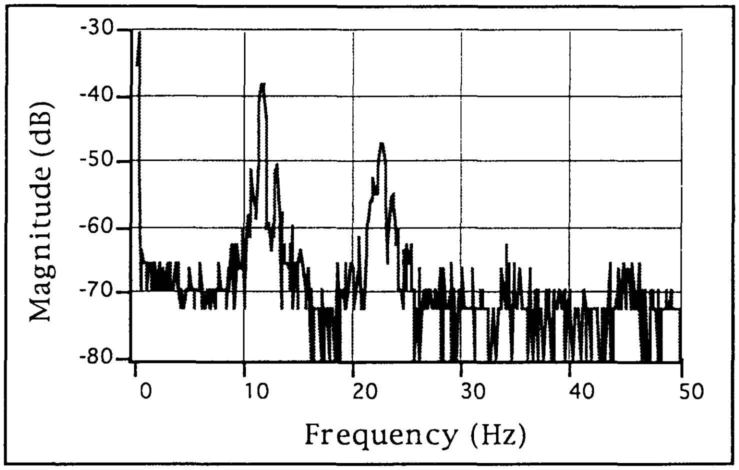

Figure 5-1: Platform leg natural frequencies

exciting these platform modes, low PD gains had been used, thus reducing the platform bandwidth to about 2 Hz. Figure 5-2 shows the frequency domain response of the original platform system without a digital filter. The low gains response in Figure 5-2 shows the reduction in bandwidth necessary to avoid vibrations. Running the platform with this reduced bandwidth created two problems:

(1) Poor emulation of systems above 1Hz due to substantial positioning errors.

(2) Excessive phase shift from the lowered gains caused increased damping which was apparent in certain admittance model systems.

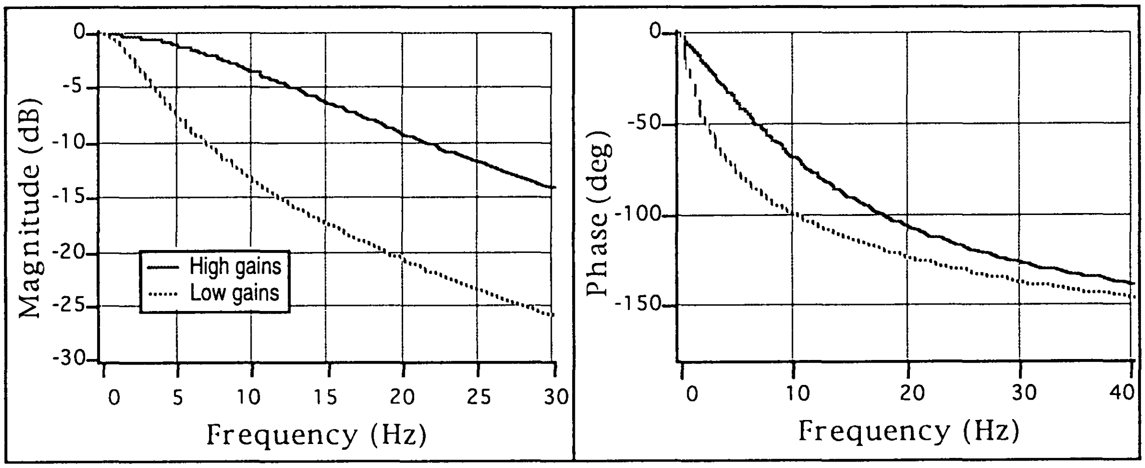

Figure 5-2: Original closed loop response with high and low gains

5.3 The Design Solution

To solve these problems, a digital filter was designed. The three basic types of filter considered are shown in Figure 5-3. A Chebychev type 2 filter was chosen to achieve a sharp corner attenuation with minimal phase shift from a low order filter. The built-in first order attenuation (20dB per decade visible in Figure 5-2) from the servo actuator was sufficient to prevent excitation of the higher vibrational modes. The absence of higher order disturbance can be seen

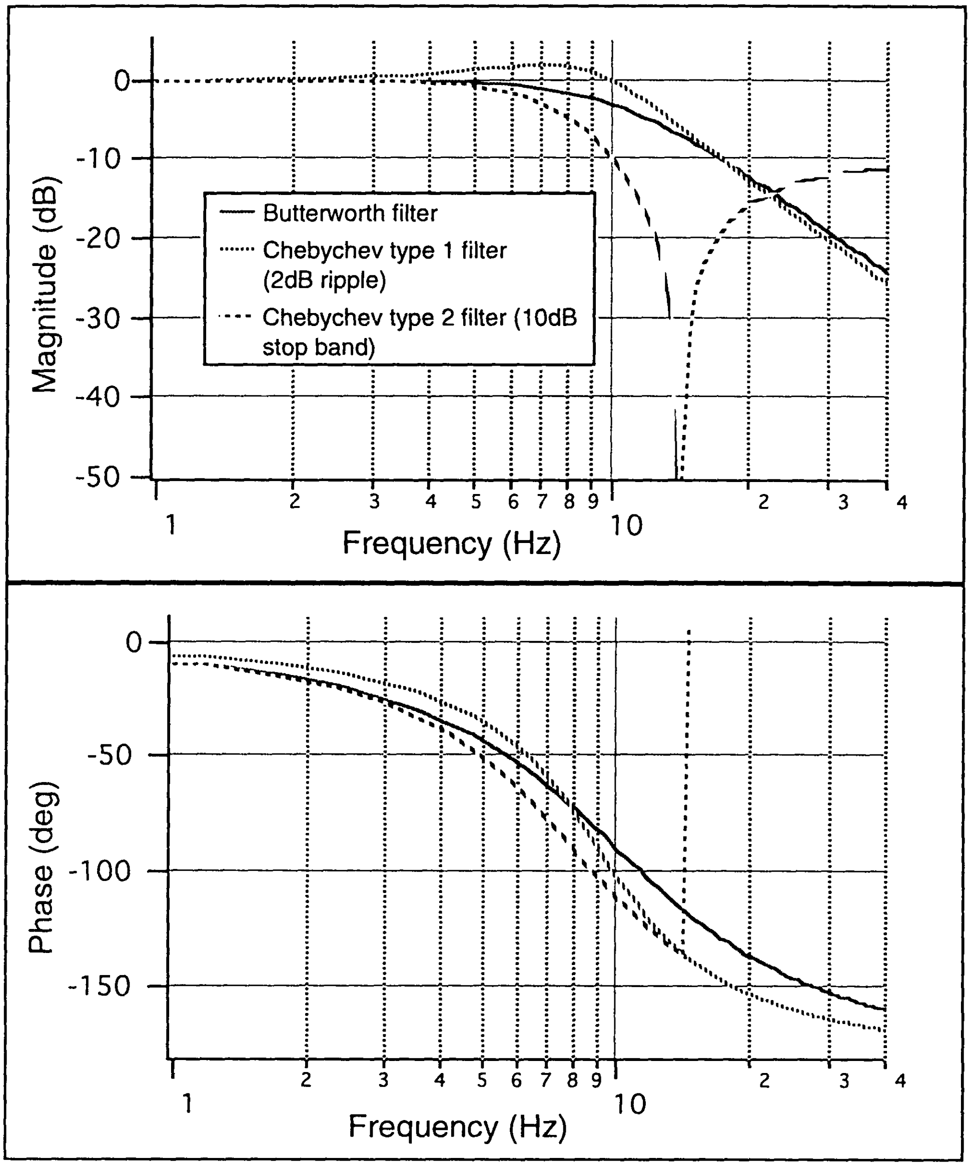

Figure 5-3: Basic filter types, corner frequency of 10Hz

in Figure 5-1. The filter therefore needed to attenuate sharply in the desired location, and minimally elsewhere. The design process was unique since the filter is part of the platform closed loop control system. A model of the closed loop actuator control system was constructed [Müller 1992], and Matlab was used to design filters within the closed loop system, to achieve a desired response of the entire system. The block diagram of a continuous approximation of the actuator system used for Matlab analysis is shown in Figure 5-4.

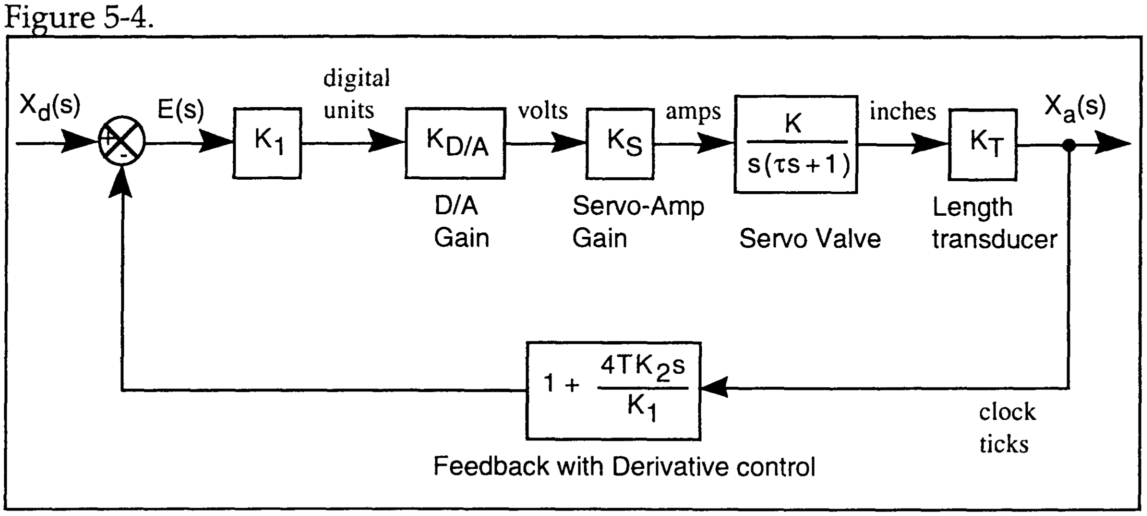

Figure 5-4: Closed Loop Actuator Block Diagram

The general form of a digital recursive filter is:

$$Y_n = b_1 \bullet X_n + b_2 \bullet X_{n-1} + b_3 \bullet X_{n-2} + \ldots - a_2 \bullet Y_{n-1} - a_3 \bullet Y_{n-2} - \ldots \qquad (5.1)$$

where Y_n is the output of the filter during digital step n, and

X_n is the input to the filter during digital step n.

Matlab can be used to generate several types of digital filter given the cycle time of the digital system and the desired filter characteristics. Designing a digital filter as an element within a complex closed loop system required several design iterations.

The legslave board software was modified to add the digital recursive filter calculations. This added a 2nd order filter component before the K_1 gain in

Figure 5-4. Timing issues became critical because of the number of calculations required for a 2nd order digital filter. The cycle time of the legslave boards was increased from 1.023 msec. (831 Hz) to 1.705 msec. (587 Hz) to allow for the added calculations. Since the Redslave board, which sends command positions to the legslave boards, runs around 100Hz (10 msec. cycle time) it is still more than five times slower than the legslaves. This insures that no commanded data will ever be ignored.

The legslave board program, with the digital filter, was then burned into 6 EPROM's and the entire platform system was run. A sine wave was input to the legslave boards (the Xd in Figure 5-4), and the magnitude and phase of the legslave board output (the voltage out of the $K_{D/A}$ component of Figure 5-4) was compared to the input wave. The platform was not allowed to run, so the actual leg measurement in the feedback loop was constant. The change in magnitude and phase shift were recorded to create a frequency response plot which is compared to the Matlab designed filter in Figure 5-5. This procedure confirmed the performance of the digital filter in the single closed loop system of Figure 5-4.

The performance of the actual closed loop platform control system, which is Figure 5-4 with the platform allowed to move, was tested by commanding the platform to perform sine wave motion in the inertial Z-axis. Commanded and actual position data for the platform were then converted to frequency and magnitude data for a frequency response plot. This testing showed that the filter did not completely attenuate the control signal in the lower end of the platform natural frequencies. The filter was redesigned to achieve this goal, but at the cost of an increasing phase lag. The increased phase lag would cause more damping in the system, so several design iterations were made.

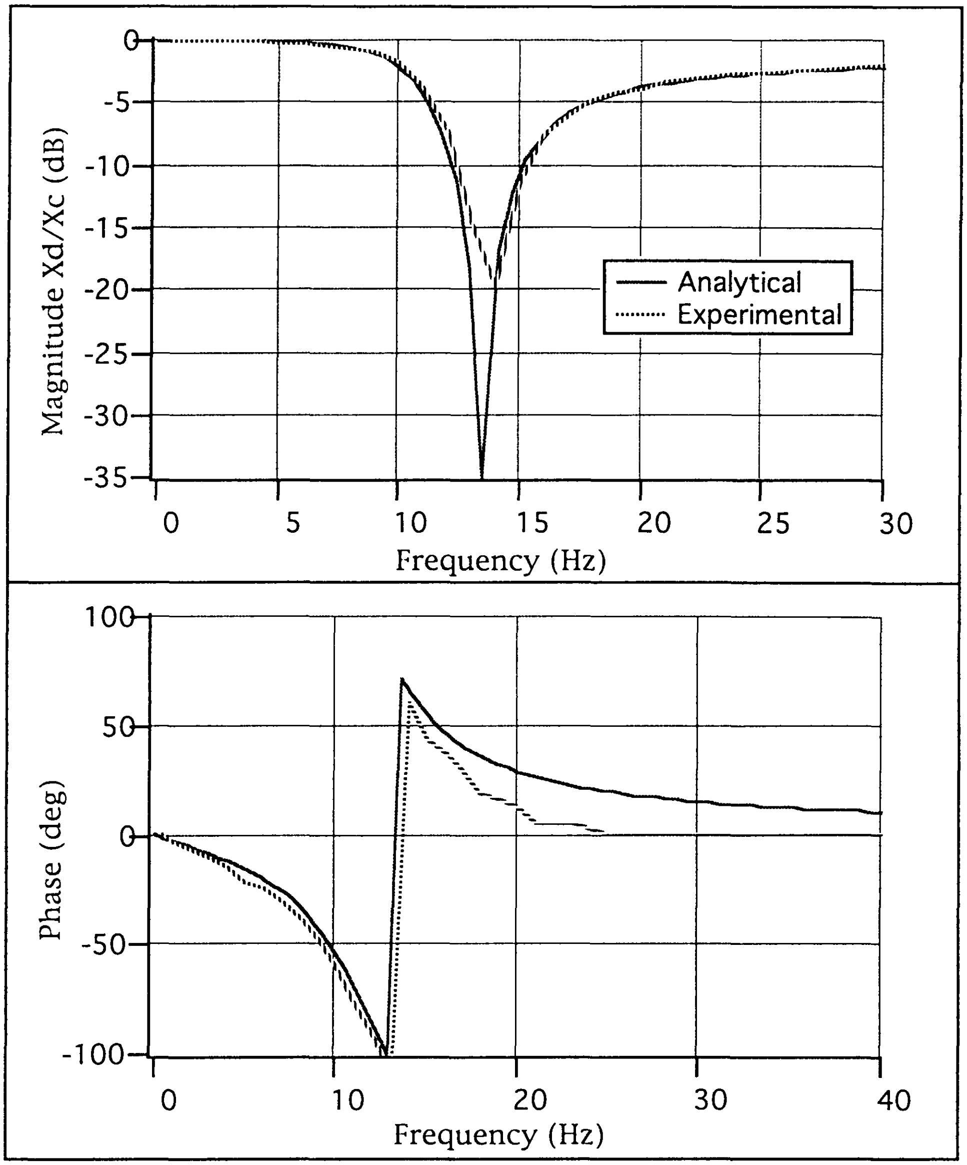

Figure 5-5: Experimental verification of open loop filter design

5.4 Effect of Filter Location on Stability

After the digital filter was added to the legslave controllers, it was found that some low mass admittance models were unstable. Even when the manipulator was not moved, the platform would slowly oscillate with increasing amplitude. The Matlab analysis of the closed loop actuator control loop [Figure 5-4] was modified to include the complete admittance model, closed loop actuator control, and force sensor feedback. This complete VES admittance control loop is represented by the block diagram in Figure 5-6.

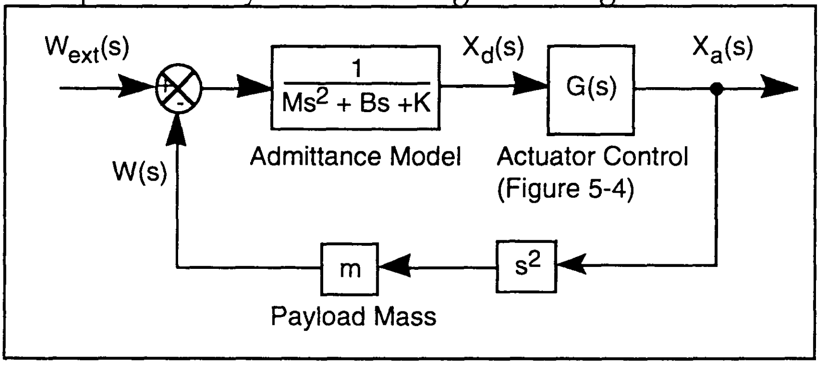

Figure 5-6: VES Admittance Control Block Diagram

The digital filter was originally programmed to operate on the error signal in the legslave controller as shown in Figure 5-7. Matlab analysis revealed that although the actuator loop itself is stable, within the total VES control loop, the digital filter caused instability. Admittance models with a mass less than half of the actual mass on the force sensor (the payload mass in Figure 5-6) were unstable, growing more unstable the lower the model's mass. A pole plot of the VES system with the digital filter affecting the error signal and a low model mass is shown in Figure 5-8. Two of the poles are clearly in the right half plane, causing instability.

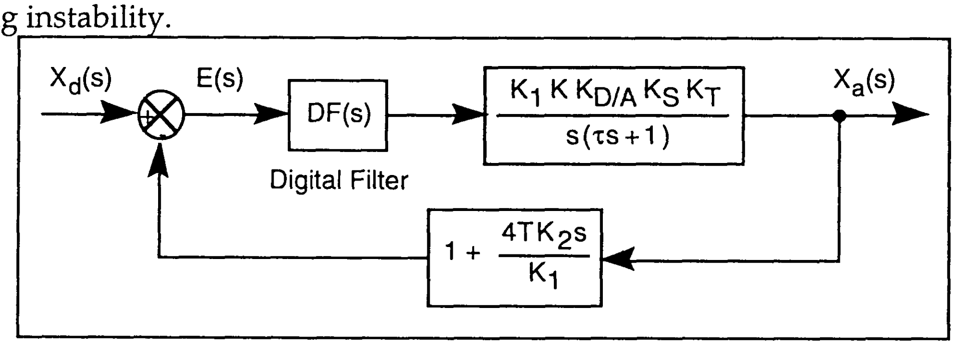

$X_d(s)$
+
E(s)
DF(s)
Digital Filter
$\frac{K_1 K K_{D/A} K_S K_T}{s(\tau s + 1)}$
$X_a(s)$
$1 + \frac{4TK_2 s}{K_1}$

Figure 5-7: Digital Filter on Error Signal

Further analysis showed that if the filter were reprogrammed to operate only on the feedback signal from the Temposonics cards, see Figure 59, the entire VES closed loop system would be stable. Figure 5-10 shows the root locus of the VES system with the digital filter affecting only the feedback signal.

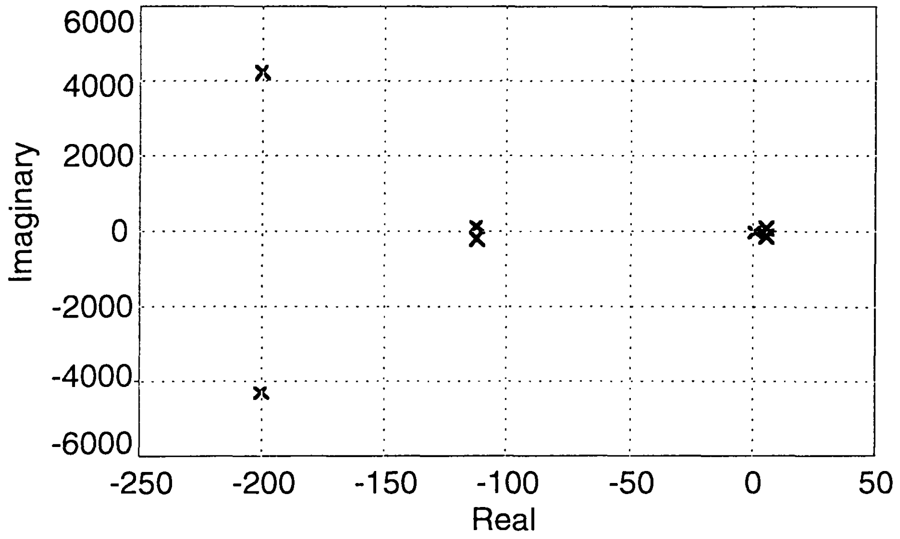

Figure 5-8: VES Pole Plot, Filter on Error Signal

Simulations confirmed that the VES system, with the digital filter on the feedback signal only, was stable for a wider range of admittance model values. Very low stiffness systems are, however, still susceptible to small errors in the force sensor.

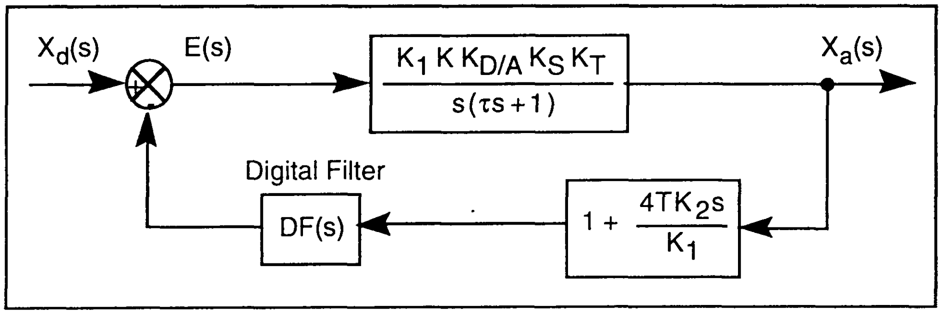
$X_d(s)$
E(s)
$\frac{K_1 K K_{D/A} K_S K_T}{s(\tau s+1)}$
$X_a(s)$
Digital Filter
DF(s)
$1 + \frac{4TK_2 s}{K_1}$

Figure 5-9: Digital Filter on Feedback Signal

At the time of the writing of this thesis, the digital filter had not been moved to operate on the feedback signal. The results of the system and the system response as shown in Sections 5.5 and 5.6 are based on Matlab analysis of the leg control (Figure 5-7 or 5-9) only, and do not change significantly based on the location of the filter. Only the stability of the total system for a small range of admittance models (Figure 5-6) is affected.

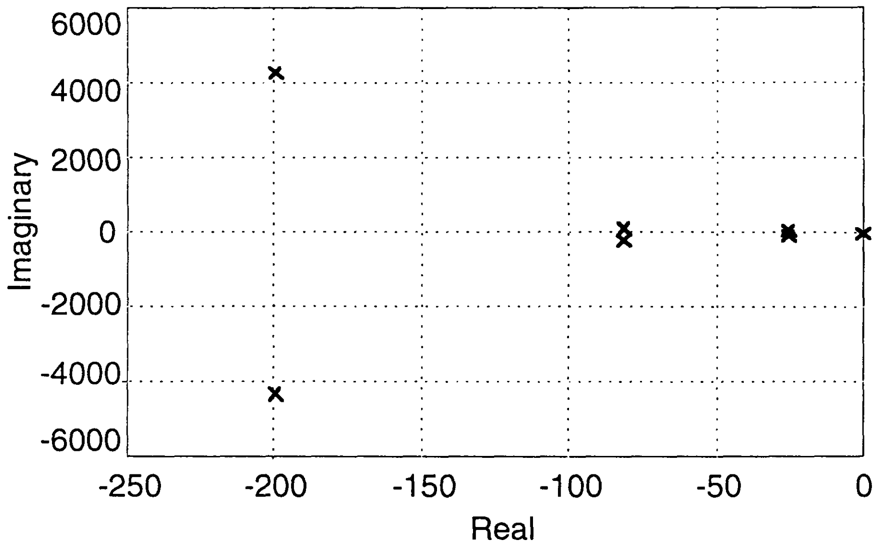

Figure 5-10: VES Pole Plot, Filter on Feedback Signal

5.5 Digital Filter Results

The specifications of the final filter design are summarized in Table 5-1. In operation, the filter has performed well. The vibrations which had been caused by disturbing the natural frequencies of the platform were removed for most cases. An experiment was performed to compare the positioning errors in the platform motion with the errors found before the digital filter was installed [Kuklinski 1993]. The admittance model used for the experiment was a decoupled model of varying parameters shown in Table 5-2, this model does not represent any physically real system. With the PUMA 560 mounted on it, the platform was displaced to an initial position Y(0)= {.2m, -.2m, .1m, 10°, -10°, 20°}, where Y(t) is defined in Equation 2.3, and then released. The micro-gravity motion which resulted was recorded, and the commanded and actual position data were collected. Figure 5-11 shows that the positioning errors, the difference between the commanded and actual position of a the platform, were reduced by about 40% over the case of using low gains without the filter.

Table 5-1: Digital Filter Specifications

Type	Chebychev Type 2
Order	2nd
Stop Band	4 dB
Corner Freq.	9 Hz
Sample Rate	587 Hz
Digital Recursive Coefficients	
a_1 = 1.0000	b_1 = 0.6040
a_2 = 1.9002	b_2 = 1.1969
a_3 = 0.9113	b_3 = 0.6040
$\frac{As^4 + Bs^3 + Cs^2 + Ds + E}{Fs^4 + Gs^3 + Hs^2 + Is + J}$ Laplace Domain Coefficients	
A= 0.00000000000854	F= 0.00000000001353
B= 0.00000000139394	G= 0.00000000616895
C= 0.00015641891531	H= 0.00024771331743
D= 0.00000019127013	I= 0.01347347243526
E= 0.99990021116393	J= 1.00000000000000

TABLE 5-2: Admittance Model for Positioning Error Experiment

Mass Matrix	Spring Matrix	Damping Matrix
M_{11}=500 kg	K_{11}=1500 N/m	B_{11}=500 N/m/s
M_{22}=500 kg	K_{22}=2500 N/m	B_{22}=500 N/m/s
M_{33}=500 kg	K_{33}=4000 N/m	B_{33}=500 N/m/s
M_{44}=250 kg·m^2	K_{44}=1500 N·m	B_{44}=250 N·m/rad/s
M_{55}=250 kg·m^2	K_{55}=1000 N/m	B_{55}=250 N·m/rad/s
M_{66}=250 kg·m^2	K_{66}=2000 N/m	B_{66}=250 N·m/rad/s

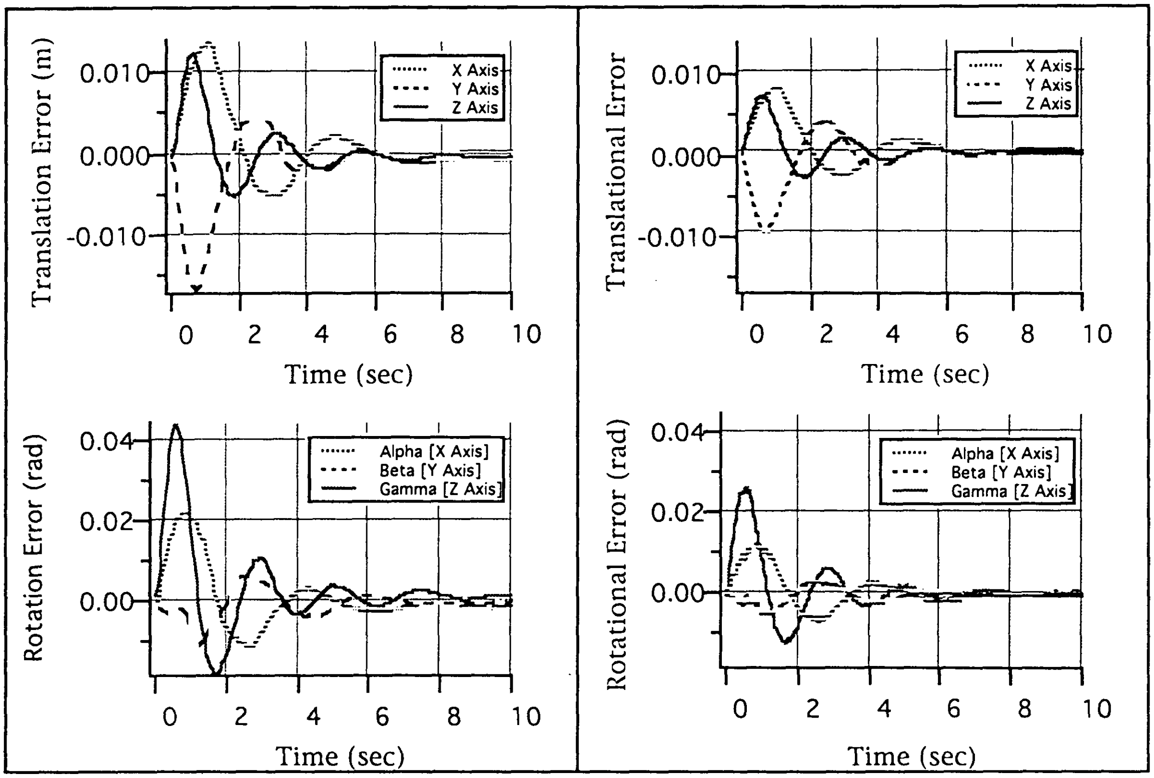

Without Filter With Filter

Figure 5-11: Platform positioning errors

5.6 Choosing Platform Gains

In some orientations one or more of the legs are stretched longer than they might during typical operation. This decreases their natural frequencies such that they are not attenuated by the filter and may cause instability. This can be alleviated by reducing the gains, again at the cost of a lower bandwidth and more phase lag. Figure 5-12 shows the bode plots of the closed loop system with the filter for a series of gains, based on simulations. It was found that K_2 (see Figure 5-4) had minimal effect on the bandwidth. It can therefore be set to a maximum to reduce overshoot. For many applications, for low frequency models when the platform stays near its home position, gains of K_1=20,000 K_2=30000 will provide a good response. If vibrations are experienced, the bandwidth can be lowered slightly by decreasing K_1. Even if very low gains are used to avoid vibrations on some experiments, the bandwidth and phase characteristics are better than would be possible without the filter; compare Figure 5-12 to Figure 5-2.

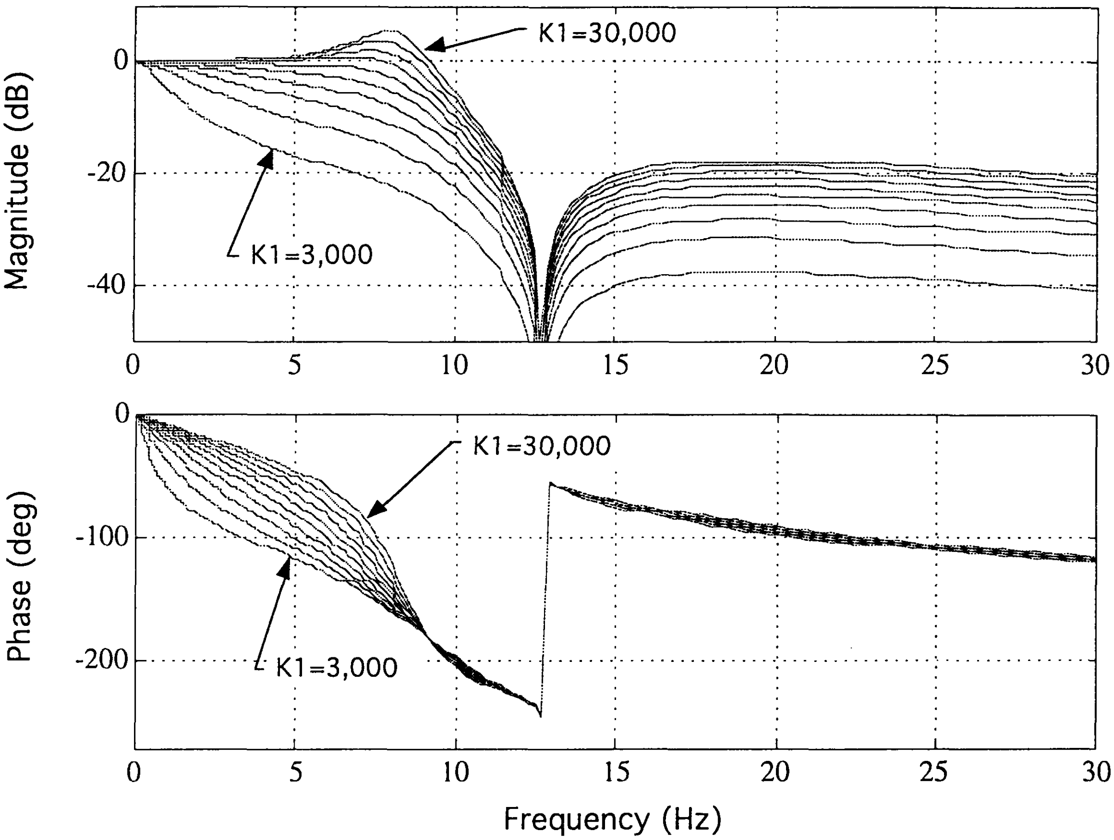

Figure 5-12: Bode Plot of Platform with Filter. {K2=30,000 K1=3,000-30,000}

The response to a unit step input of the closed loop leg control system, including the filter, with varying gains is shown in Figure 5-13. This figure is based on Matlab analysis.

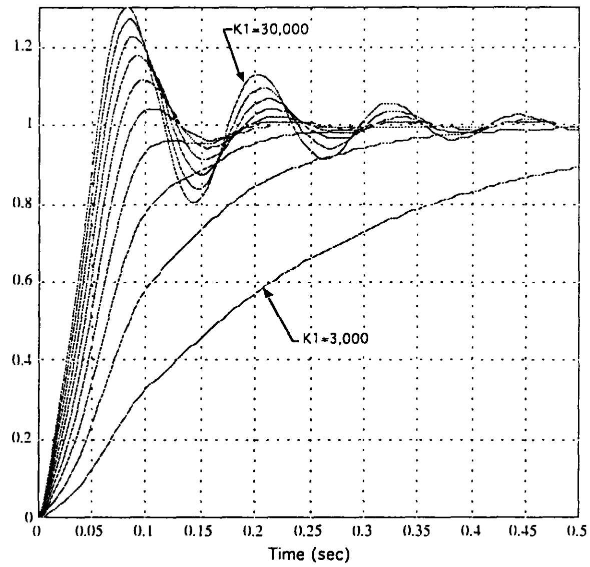

Figure 5-13: Platform Unit Step Response with Filter

5.7 Summary

A vibration problem encountered in the VES system was presented. An analysis and the development of a digital filter to solve this problem was also presented in detail. The effectiveness of the design was discussed. Finally, an interesting application of control theory was detailed, the effects of positioning a simple filter within a complex system.

Chapter 6

Conclusions

6.1 Contributions of This Work

This thesis describes the implementation of two micro-gravity emulation routines on the VES II, the Learning Method and the Model Method. This system can now be used to experimentally evaluate the dynamic interaction between a robotic manipulator and its supporting structure in the micro-gravity of space.

An overview of the basic components and operation of the VES II was presented. An introduction was also given to the control architecture of the VES II and the PUMA 560. The basic theory of the admittance control concept was also presented.

The theoretical developments for gravity compensation were presented in detail. The difficulties of estimating the effects of gravity were discussed. Two methods were presented to compensate for gravity on the VES II, a learning based method and a model based method. Experimental results were presented which showed the accuracy of these methods.

Two algorithms were investigated which address the problem of vibrations in space manipulators on highly flexible bases. The Coupling Map algorithm was shown to accurately plan paths which minimize the energy transferred to the flexible base. The Pseudo-Passive Energy Dissipation concept was shown to remove energy from an oscillating beam, allowing the settling time to be reduced for a given disturbance. Both of these algorithms can be used to reduce the time and cost of space robotic operations.

A vibration problem encountered in the VES system was discussed. An analysis and the development of a digital filter to solve this problem was presented in detail. The effectiveness of the design was documented. Finally, an interesting application of control theory was presented, the effects of positioning a simple filter within a complex system.

Many details and calculations from this work are documented in the appendices. This will hopefully provide a useful source of information for researchers who will follow this work in the future.

6.2 Recommendations for Future Work

The primary contribution of this work was to bring the VES II system to a state where it could reliably emulate micro-gravity. Some experimental work was then performed with the system, but only a small sample of the possible space robotic algorithms which could be tested. The most obvious and important requirement for further work in this area is the application of the VES II system to a number of control and planning algorithms for space robotics.

Although some improvement in the VES II will undoubtedly be made in the future, there are no immediate problems to be solved. The primary addition to the VES system should be the software which will expand the range of useful experiments it can perform. Great care should be taken in the structure of new software to fit it smoothly into the VES regime, but also to keep the total VES software in a coherent state. The total software required to run a VES experiment has already become very extensive, with no less than 6 programmers contributing. For the VES system to remain useful, all capabilities and modifications of the software should be user friendly and well documented.

Bibliography

Alexander, H. and Cannon, R., "An Extended Operational-Space Control Algorithm for Satellite Manipulators," *Journal of Astronautical Sciences,* Vol. 38, No. 4, 1990, pp. 473-486.

Arimoto, S., Kawamura, S., and Miyazaki, F., "Bettering Operation of Robots by Learning," *Journal of Robotic Systems,* Vol. 1, 1984, pp. 123-140.

Armstrong, B., O. Khatib and J. Burdick, "The Explicit Dynamic Model and Inertial Parameters of the PUMA 560 Arm." *Proceedings of the IEEE International Conference on Robotics and Automation,* San Francisco, April 1986, pp. 510-518.

Corrigan, T. and Dubowsky, S., "Emulating Micro-Gravity in Laboratory Studies of Space Robotics," *1994 ASME Mechanisms Conference,* St. Paul, MN, Sept. 1994.

Craig, J., Introduction to Robotics, Addison Wesley Publishing Co., 1989

Crane, C.D., Duffy, J. and Carnahan, T., "A Kinematic Analysis of the Space Station Remote Manipulator System (SSRMS)," *Journal of Robotic Systems,* vol. 8, no. 5, 1991, pp. 637-658.

Dubowsky, S., et al, "The Design and Implementation of a Laboratory Test Bed for Space Robotics: The VES Mod II," *1994 ASME Mechanisms Conference,* St. Paul, MN, September 1994.

Dubowsky, S., Paul, I. and West, H., " An Analytical and Experimental Program to Develop Control Algorithms for Mobile Manipulators," *Proceedings* *of the VIIth Symposium on Theory and Practice of Robots and Manipulators,* Udine, Italy, Sept., 1988.

Durfee, W., Idris, H. and Dubowsky, S., "Real Time Control of the MIT Vehicle Emulator System," *Proceedings of the 1991 American Control Conference,* Boston, MA, June 1991, pp. 2057-2058.

Erickson, J.D., Reuter, G. J. and Healey, K.J., " Technology for an Intelligent, Free Flying Robot for Crew and Equipmet Retrieval in Space," *Proceedings of the Space Operations & Robotics Conference & Workshop,* JSC, Houston, TX, July 1989.

Fresko, M., "The Design and Implementation of a Computer Controlled Platform with Variable Admittance," S.M. Thesis, Department of Mechanical Engineering, MIT, Cambridge, MA, January 1987.

Idris, H., Real-Time Control of a Six Degree-of-Freedom Vehicle Emulation System, S.M. Thesis, Dept. of Mech. Engineering, MIT, Cambridge, MA, April 1992.

Iwata, T. et al., "Ground & Flying Testbed for the 2nd Generation Space Robot," *Proceedings of the i-SAIRAS* '90, Kobe, Japan, 1990.

Juvinall, R. and Marshek, K, Fundamentals of Machine Component Design, John Wiley and Sons, 1991.

Kuklinski, A., The Practical Implementation of an Experimental Tool for the Dynamic Interactions in Mobile Manipulator Systems, S.M. Thesis, Department of Mechanical Engineering, MIT, Cambridge, MA, June 1993.

Mayeda, H., K. Osuka and A. Kangawa, "A New Identification Method for Serial Manipulator Arms," *9th IFAC World Congress*, Vol II, 1984, pp. 2429-2434.

Mayeda, H., Yoshida, K. and Osuka, K., "Base Parameters of Manipulator Dynamic Models," *Proceedings of the IEEE International Conference on Robotics and Automation*, 1988, pp. 1367-1372.

Müller, U., Design of a Second Generation Experimental System for Studying Mobile Manipulator Control, S.M. Thesis, Department of Mechanical Engineering, MIT, Cambridge, MA, June 1992.

Olsen, Howard B. and Bekey, George A., "Identification of Parameters in Models of Robots with Rotary Joints," *Proceedings of the IEEE International Conference on Robotics and Automation*, 1985, pp. 1045-1049.

Papadopoulos, E. and Dubowsky, S., "The Kinematics, Dynamics and Control of Free-Flying and Free-floating Space Robotics Systems," Special Issue on Space Robotics, *IEEE Transactions on Robotics and Automation*, Vol. 9, No. 5, October 1993, pp. 1-13.

Sato, Y., et al., "Micro-G Emulation System Using Constant-Tension Suspension for a Space Manipulator," *Proceedings of the 1991 IEEE International Conference on Robotics and Automation*, Sacramento, CA, April 1991.

Shimoji, H., et al., "Simulation System for a Space Robot Using 6 Axes Servos," *Proceedings of the XIth IFAC Symposium of Automatic Control in Aerospace*, Tsukuba, Japan, 1989, pp. 115-120.

Spofford, J.R. and Akin, D.L. "Redundancy Control of a Free-Flying Telerobot," *AIAA Journal of Guidance, Control and Dynamics*, vol. 13, No. 3, pp. 515-523, May 1990.

Stelman, N., "Design and Control of a Six-Degree-of-Freedom Platform with Variable Admittance," S.M. Thesis, Department of Mechanical Engineering, MIT, Cambridge, MA, May 1988.

Torres, M., "Modeling, Path-Planning and Control of Space Manipulators: The Coupling Map Concept," Ph.D. Thesis, Department of Mechanical Engineering, MIT, Cambridge, MA, February 1993.

Torres, M. and Dubowsky, S., "Path Planning for Elastically Constrained Space Manipulator Systems," *Proceedings of the IEEE International Conference on Robotics and Automation*, Atlanta, GA, May, 1993, pp. 812-817.

Ulrich, N. and Kumar, V., "Passive Mechanical Gravity Compensation for Robot Manipulators," *Proceedings of the IEEE International Conference on Robotics and Automation*, Sacramento, CA, April 1991, pp. 1536-1541.

Umatani, Y. and Yoshida, K., "Experimental Study of a Two Dimensional Free-Flying Robot Satellite Model," *Proceedings of the NASA Conf. on Space Telerobotics*, Pasadena, CA, January 1989.

Umetani, Y. and Holcomb, L., Co-Chairmen, *Proceedings of the i-SAIRAS '90*, Kobe, Japan, November, 1990.

Vafa, Z., an Dubowsky, S., "The Kinematics and Dynamics of Space Manipulators: The Virtual Manipulator Approach," *The International Journal of Robotics Research,* August 1990.

Vafa, Z., The Kinematics, Dynamics and Control of Space Manipulators: The Virtual Manipulator Concept. PhD Thesis, Department of Mechanical Engineering, MIT, Cambridge, MA, November 1987.

West, H., Papadopoulos, E., Dubowsky, S. and Cheah, H., "A Method for Estimating the Mass Properties of a Manipulator by Measuring the Reaction Moments at its Base," *Proceedings of the IEEE International Conference on Robotics and Automation,* Scottsdale, AZ, 1989.

Whittaker, W.L., et al., *Space Robotics in Japan,* NASA Japanese Technical Evaluation Center Report (JTEC), January 1991.

Xu, Y. and Kanade T., Space Robotics: Dynamics and Control, Kluwer Academic Publishers, 1993

Appendix A

Modeling Beam Structures

A.1 Introduction

This section describes a simple method of generating an admittance model for a simple beam structure. The admittance model concept was introduced in Section 2.3. The form of the admittance model dynamic equations is (Equation 3):

$$M\ddot{Y}(t) + B\dot{Y}(t) + KY(t) = \mathbf{W}(t).$$

Basic laws of mechanics are applied to beam systems to generate the 6 by 6 matrices M, K and B which model the system.

A.2 Modeling a Straight Beam

Beam Parameter	Variable	Value (Al)
Length	L	see A.3
Modulus of Elasticity	E	72×10^9 Pa
Modulus of Rigidity	G	27×10^9 Pa
Moment of Inertia	I	see A.3
Polar Moment of Inertia	J	see A.3
Area	A	see A.3
Mass	M	see A.3
Material Density	ρ	2.8×10^3 kg/m^3

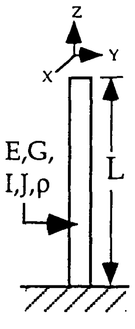

Analysis of a cantilever beam [Juvinall and Marshek 1991] produces the familiar deflections and rotations as a function of Forces and Moments:

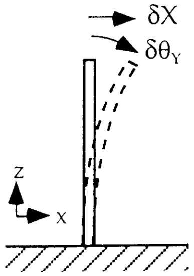

$$\delta X = \frac{F_X \bullet L^3}{3 \bullet E \bullet I} + \frac{M_Y \bullet L^2}{2 \bullet E \bullet I}$$

$$\delta \theta_Y = \frac{M_Y \bullet L}{E \bullet I} + \frac{F_X \bullet L^2}{2 \bullet E \bullet I}$$

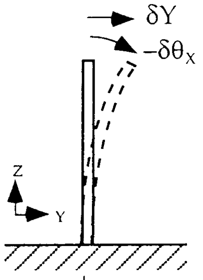

$$\delta Y = \frac{F_Y \bullet L^3}{3 \bullet E \bullet I} - \frac{M_X \bullet L^2}{2 \bullet E \bullet I}$$

$$\delta \theta_X = \frac{M_X \bullet L}{E \bullet I} - \frac{F_Y \bullet L^2}{2 \bullet E \bullet I}$$

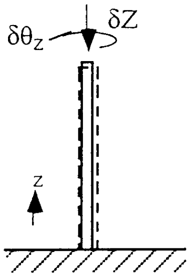

$$\delta Z = \frac{F_Z \bullet L}{E \bullet A}$$

$$\delta \theta_Z = \frac{M_Z \bullet L}{G \bullet J}$$

These equations can be used to produce a compliance matrix Q which is the inverse of our stiffness matrix K {K=F/X, Q=X/F, K=Q^{-1}}:

$$Q_{11} = \frac{\delta X}{F_X} = \frac{L^3}{3 \bullet E \bullet I} \qquad Q_{15} = \frac{\delta X}{M_Y} = \frac{L}{E \bullet I}$$

$$Q_{22} = \frac{\delta Y}{F_Y} = \frac{L^3}{3 \bullet E \bullet I} \qquad Q_{24} = \frac{\delta Y}{M_X} = - \frac{L^2}{2 \bullet E \bullet I}$$

$$Q_{33} = \frac{\delta Z}{F_Z} = \frac{L}{E \bullet A}$$

$$Q_{42} = \frac{\delta \theta_X}{F_Y} = - \frac{L^2}{2 \bullet E \bullet I} \qquad Q_{44} = \frac{\delta \theta_X}{M_X} = \frac{L}{E \bullet I}$$

$$Q_{51} = \frac{\delta \theta_Y}{F_X} = \frac{L^2}{2 \bullet E \bullet I} \qquad Q_{55} = \frac{\delta \theta_Y}{M_Y} = \frac{L}{E \bullet I}$$

$$Q_{66} = \frac{\delta \theta_Z}{M_Z} = \frac{L}{G \bullet J}$$

The total mass of the beam can be calculated easily:

$$\text{mass} = A \bullet L \bullet \rho$$

The equivalent mass seen at the end of the beam can be calculated by the kinetic-energy method [Shigley 1967] as:

$$\text{mass}_{eq} = \text{mass}/2$$

The equivalent inertia seen at the end of the beam can be reasonably calculated by the equivalent parameter method [Shigley 1967] as:

$$I_{eq} = \text{mass}_{eq} \bullet L^2$$

The mass matrix can then be created as:

$$M_{11} = M_{22} = M_{33} = \text{mass}_{eq}$$

$$M_{44} = M_{55} = I_{eq}$$

$$M_{66} = I_{zz} \approx 0$$

A damping matrix can then be chosen to create a 5% damping ratio for the system:

$$B = 2 \bullet \zeta \bullet \sqrt{K \bullet M} \qquad \zeta = .05$$

A.3 Straight Beam Experiments

The equations above produce the following matrices for a 12 meter long hollow cylinder with a diameter of 7 cm and a wall thickness of 6 mm made of aluminum oriented vertically as shown in Figure A-1:

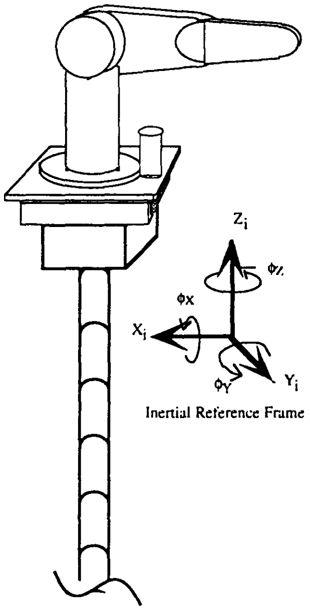

Figure A-1: PUMA on Vertical Beam

$$\text{Mass Matrix} = \begin{bmatrix} 20\ \text{kg} & 0 & 0 & 0 & 0 & 0 \\ 0 & 20\ \text{kg} & 0 & 0 & 0 & 0 \\ 0 & 0 & 20\ \text{kg} & 0 & 0 & 0 \\ 0 & 0 & 0 & 5\ \text{kg}\cdot\text{m}^2 & 0 & 0 \\ 0 & 0 & 0 & 0 & 2900\ \text{kg}\cdot\text{m}^2 & 0 \\ 0 & 0 & 0 & 0 & 0 & 2900\ \text{kg}\cdot\text{m}^2 \end{bmatrix}$$

$$\text{Stiffness Matrix} =$$

$$\begin{bmatrix} 312\ \text{N/m} & 0 & 0 & 0 & -1870\ \text{N/rad} & 0 \\ 0 & 312\ \text{N/m} & 0 & 1870\ \text{N/rad} & 0 & 0 \\ 0 & 0 & 7\text{x}10^6\ \text{N/m} & 0 & 0 & 0 \\ 0 & 1870\ \text{N}\cdot\text{m/m} & 0 & 15000\ \text{N}\cdot\text{m/rad} & 0 & 0 \\ -1870\ \text{N}\cdot\text{m/m} & 0 & 0 & 0 & 15000\ \text{N}\cdot\text{m/rad} & 0 \\ 0 & 0 & 0 & 0 & 0 & 2800\ \text{N}\cdot\text{m/rad} \end{bmatrix}$$

$$\text{Damping Matrix} = \begin{bmatrix} 5\ \text{N/m/s} & 0 & 0 & 0 & 0 & 0 \\ 0 & 5\ \text{N/m/s} & 0 & 0 & 0 & 0 \\ 0 & 0 & 1200\ \text{N/m/s} & 0 & 0 & 0 \\ 0 & 0 & 0 & 660\ \text{N}\cdot\text{m/rad/s} & 0 & 0 \\ 0 & 0 & 0 & 0 & 660\ \text{N}\cdot\text{m/rad} & 0 \\ 0 & 0 & 0 & 0 & 0 & 2\ \text{N}\cdot\text{m/rad} \end{bmatrix}$$

Note that for a hollow circle:

$$I = \frac{\pi}{64} \cdot (D_{outer}{}^4 - D_{inner}{}^4)\ ,$$

where $D_{inner} = D_{outer} - 2 \cdot t$,

and:

$$J=2 \cdot I.$$

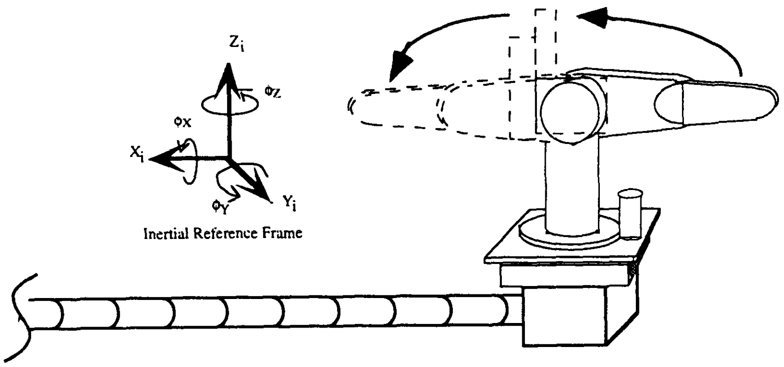

Figure A-2: PUMA on VES Performing Simple Motion

Several experiments in this thesis use the same beam, a 12 meter long hollow aluminum cylinder with a diameter of 7 cm and a wall thickness of 6mm, oriented horizontally as shown in Figure A-2. A rotation matrix can be used to produce the matrices for this horizontal beam:

$$\begin{array}{c} \text{Mass} \\ \text{Matrix} \end{array} = \begin{bmatrix} 20\ \text{kg} & 0 & 0 & 0 & 0 & 0 \\ 0 & 20\ \text{kg} & 0 & 0 & 0 & 0 \\ 0 & 0 & 20\ \text{kg} & 0 & 0 & 0 \\ 0 & 0 & 0 & 2900\ \text{kg}\cdot\text{m}^2 & 0 & 0 \\ 0 & 0 & 0 & 0 & 2900\ \text{kg}\cdot\text{m}^2 & 0 \\ 0 & 0 & 0 & 0 & 0 & 5\ \text{kg}\cdot\text{m}^2 \end{bmatrix}$$

$$\begin{array}{c} \text{Stiffness} \\ \text{Matrix} \end{array} =$$

$$\begin{bmatrix} 7\text{x}10^6\ \text{N/m} & 0 & 0 & 0 & 0 & 0 \\ 0 & 312\ \text{N/m} & 0 & 0 & 0 & 1870\ \text{N/rad} \\ 0 & 0 & 312\ \text{N/m} & 0 & -1870\ \text{N/rad} & 0 \\ 0 & 0 & 0 & 2800\ \text{N}\cdot\text{m/rad} & 0 & 0 \\ 0 & 0 & -1870\ \text{N/rad} & 0 & 15000\ \text{N}\cdot\text{m/rad} & 0 \\ 0 & 1870\ \text{N/rad} & 0 & 0 & 0 & 15000\ \text{N}\cdot\text{m/rad} \end{bmatrix}$$

$$\begin{array}{c} \text{Damping} \\ \text{Matrix} \end{array} = \begin{bmatrix} 1200\ \text{N/m/s} & 0 & 0 & 0 & 0 & 0 \\ 0 & 5\ \text{N/m/s} & 0 & 0 & 0 & 0 \\ 0 & 0 & 5\ \text{N/m/s} & 0 & 0 & 0 \\ 0 & 0 & 0 & 2\ \text{N}\cdot\text{m/rad/s} & 0 & 0 \\ 0 & 0 & 0 & 0 & 660\ \text{N}\cdot\text{m/rad} & 0 \\ 0 & 0 & 0 & 0 & 0 & 660\ \text{N}\cdot\text{m/rad} \end{bmatrix}$$

For several experiments in this thesis, the preceding horizontal beam model was used in the VES, and the PUMA 560 was commanded to move its shoulder joint through 180 degrees of motion, shown in Figure A-2. Details on the PUMA 560 used are provided in Appendix B. The position and velocity profiles of joint 1 are shown in Figure A-3. Joints 2 & 3 were held at 0°.

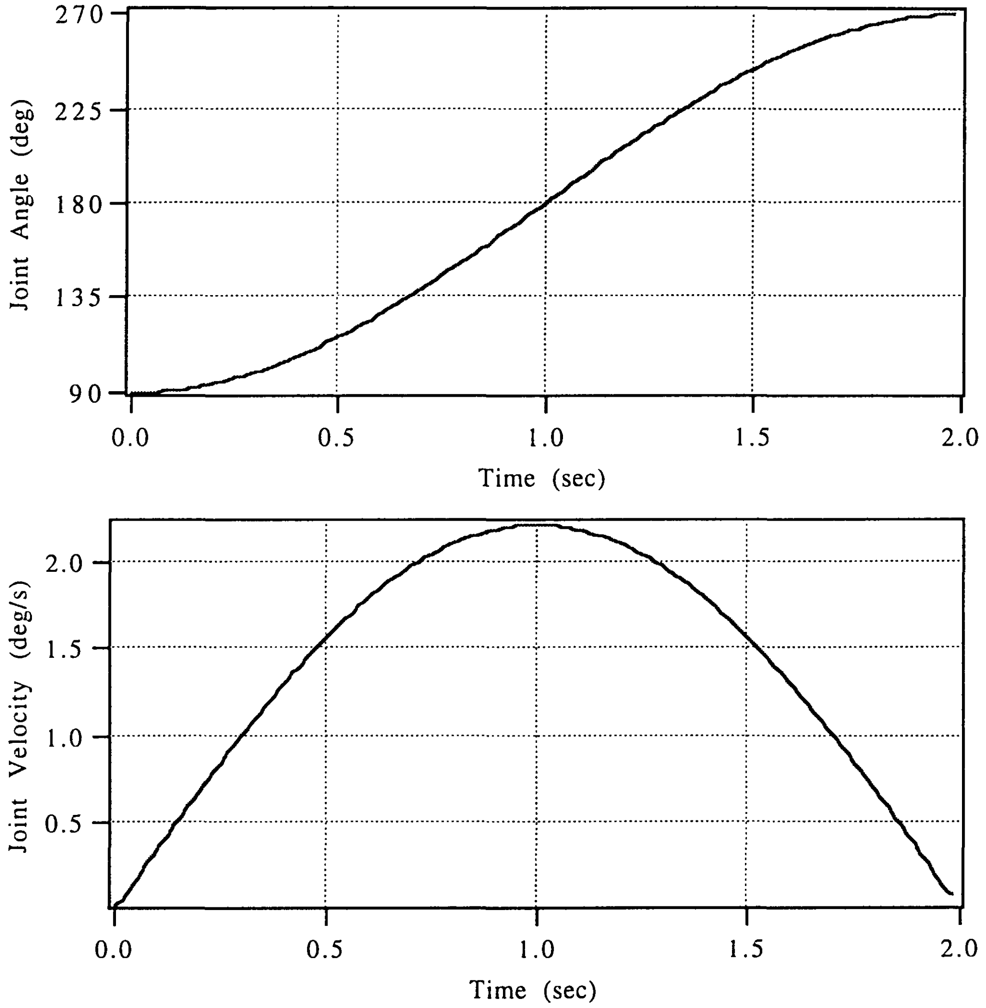

Figure A-3: Position and Velocity Profiles of Simple Motion

A.4 Modeling a Complex Beam

Beam Parameter	Variable	Value (Al)
Length	L_1 and L_2	see A.5
Modulus of Elasticity	E	$72\text{x}10^9$ Pa
Modulus of Rigidity	G	$27\text{x}10^9$ Pa
Moment of Inertia	I	see A.5
Polar Moment of Inertia	J	see A.5
Area	A	see A.5
Mass	M	see A.5
Material Density	ρ	$2.8\text{x}10^3$ kg/m^3

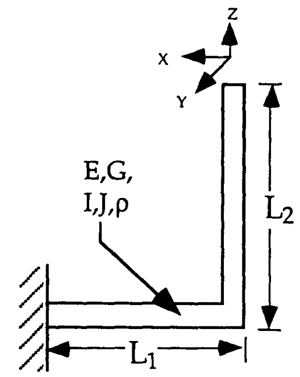

This more complex beam can be analyzed as the superposition of two simple beams. To form a compliance matrix, it is easiest to look at the translational and rotational effect of imposing individual forces and moments on the end of this structure:

$$F_X \Rightarrow \delta X = \frac{F_X \bullet L_2{}^3}{3 \bullet E \bullet I} \qquad \delta\theta_Y = \frac{F_X \bullet L_2{}^2}{2 \bullet E \bullet I} \qquad \{\text{Force on } L_2\}$$

$$\delta X = \frac{F_X \bullet L_1}{E \bullet A} \qquad \{\text{Force on } L_1\}$$

$$\delta Z = \frac{F_X \bullet L_2 \bullet L_1{}^2}{2 \bullet E \bullet I} \qquad \delta\theta_Y = \frac{F_X \bullet L_2 \bullet L_1}{E \bullet I} \qquad \delta X = L_2 \bullet \delta\theta_Y = \frac{F_X \bullet L_2{}^2 \bullet L_1}{E \bullet I} \qquad \{\text{Moment on } L_1\}$$

$$F_Y \Rightarrow \delta Y = \frac{F_Y \bullet L_2{}^3}{3 \bullet E \bullet I} \qquad \delta\theta_X = -\frac{F_Y \bullet L_2{}^2}{2 \bullet E \bullet I} \qquad \{\text{Force on } L_2\}$$

$$\delta Y = \frac{F_Y \bullet L_1{}^3}{3 \bullet E \bullet I} \qquad \delta\theta_Z = -\frac{F_Y \bullet L_1{}^2}{2 \bullet E \bullet I} \qquad \{\text{Force on } L_1\}$$

$$\delta\theta_X = -\frac{F_Y \bullet L_2 \bullet L_1}{G \bullet J} \qquad \delta Y = -L_2 \bullet \delta\theta_X = \frac{F_Y \bullet L_2{}^2 \bullet L_1}{G \bullet J} \qquad \{\text{Moment on } L_1\}$$

$$F_Z \Rightarrow \delta Z = \frac{F_Z \bullet L_2}{E \bullet A} \qquad \{\text{Force on } L_2\}$$

$$\delta Z = \frac{F_Z \bullet L_1{}^3}{3 \bullet E \bullet I} \qquad \delta\theta_Y = \frac{F_Z \bullet L_1{}^2}{2 \bullet E \bullet I} \qquad \delta X = L_2 \bullet \delta\theta_Y = \frac{F_Z \bullet L_1{}^2 \bullet L_2}{2 \bullet E \bullet I} \qquad \{\text{Force on } L_1\}$$

$$M_X \;\Rightarrow\; \delta Y = -\frac{M_X \bullet L_2^2}{2 \bullet E \bullet I} \qquad \delta\theta_X = \frac{M_X \bullet L_2}{E \bullet I}$$

{Moment on L_2}

$$\delta\theta_X = \frac{M_X \bullet L_1}{G \bullet J} \qquad \delta Y = -L_2 \bullet \delta\theta_X = -\frac{M_X \bullet L_2 \bullet L_1}{G \bullet J}$$

{Moment on L_1}

$$M_Y \;\Rightarrow\; \delta X = -\frac{M_Y \bullet L_2^2}{2 \bullet E \bullet I} \qquad \delta\theta_Y = \frac{M_Y \bullet L_2}{E \bullet I}$$

{Moment on L_2}

$$\delta Z = \frac{M_Y \bullet L_1^2}{2 \bullet E \bullet I} \qquad \delta\theta_Y = \frac{M_Y \bullet L_1}{G \bullet J} \qquad \delta X = L_2 \bullet \delta\theta_Y = -\frac{M_Y \bullet L_2 \bullet L_1}{G \bullet J}$$

{Moment on L_1}

$$M_Z \;\Rightarrow\; \delta\theta_Z = \frac{M_Z \bullet L_2}{G \bullet J}$$

{Moment on L_2}

$$\delta Y = -\frac{M_Z \bullet L_1^2}{2 \bullet E \bullet I} \qquad \delta\theta_Z = \frac{M_Z L_1}{E \bullet I}$$

{Moment on L_1}

These terms can be used to produce a compliance matrix Q for this system:

$$Q_{11} = \frac{\delta X}{F_X} = \frac{L_2^3}{3 \bullet E \bullet I} + \frac{L_1}{E \bullet A} + \frac{L_2^2 \bullet L_1}{E \bullet I}$$

$$Q_{22} = \frac{\delta Y}{F_Y} = \frac{L_2^3}{3 \bullet E \bullet I} + \frac{L_1^3}{3 \bullet E \bullet I} + \frac{L_2^2 \bullet L_1}{G \bullet J}$$

$$Q_{31} = \frac{\delta Z}{F_X} = \frac{L_2 \bullet L_1^2}{2 \bullet E \bullet I}$$

$$Q_{42} = \frac{\delta\theta_X}{F_Y} = -\frac{L_2^2}{2 \bullet E \bullet I} - \frac{L_1 \bullet L_2}{G \bullet J}$$

$$Q_{51} = \frac{\delta X}{M_Z} = \frac{L_2^2}{2 \bullet E \bullet I} + \frac{L_2 \bullet L_1}{E \bullet I}$$

$$Q_{62} = \frac{\delta\theta_Z}{F_Y} = -\frac{L_1^2}{2 \bullet E \bullet I}$$

$$Q_{13} = \frac{\delta X}{M_Y} = \frac{L_2 \bullet L_1^2}{2 \bullet E \bullet I}$$

$$Q_{15} = \frac{\delta X}{M_Z} = \frac{L_2^2}{2 \bullet E \bullet I} + \frac{L_2 \bullet L_1}{E \bullet I}$$

$$Q_{24} = \frac{\delta Y}{M_X} = -\frac{L_2^2}{2 \bullet E \bullet I} - \frac{L_1 \bullet L_2}{G \bullet J}$$

$$Q_{26} = \frac{\delta Y}{M_Z} = -\frac{L_1^2}{2 \bullet E \bullet I}$$

$$Q_{33} = \frac{\delta Z}{F_Z} = \frac{L_2}{E \bullet A} + \frac{L_1^3}{3 \bullet E \bullet I}$$

$$Q_{35} = \frac{\delta Z}{M_Y} = \frac{L_1^2}{2 \bullet E \bullet I}$$

$$Q_{44} = \frac{\delta\theta_X}{M_X} = \frac{L_2}{E \bullet I} + \frac{L_1}{G \bullet J}$$

$$Q_{53} = \frac{\delta\theta_Y}{F_Z} = \frac{L_1^2}{2 \bullet E \bullet I}$$

$$Q_{55} = \frac{\delta\theta_Y}{M_Y} = \frac{L_2}{E \bullet I} + \frac{L_1}{G \bullet J}$$

$$Q_{66} = \frac{\delta\theta_Z}{M_Z} = \frac{L_2}{G \bullet J} \frac{L_1}{E \bullet I}$$

The total mass of the beam can be calculated easily:

$$mass = A \bullet (L_1+L_2) \bullet \rho$$

The equivalent mass seen at the end of the beam can be calculated by the kinetic-energy method [Shigley 1967] as:

$$mass_{eq} = mass/2$$

The equivalent inertia seen at the end of the beam can be reasonably calculated by the equivalent parameter method [Shigley 1967] as:

$$I_{XXeq} = mass_{eq} \bullet L_2^2$$

$$I_{ZZeq} = mass_{eq} \bullet L_1^2$$

$$I_{YYeq} = mass_{eq} \bullet (L_1^2+L_2^2)$$

The mass matrix can then be created as:

$$M_{11} = M_{22} = M_{33} = mass_{eq}$$

$$M_{44} = I_{XXeq}$$

$$M_{55}= I_{YYeq}$$

$$M_{66} = I_{ZZeq}$$

A damping matrix can then be chosen to create a 5% damping ratio for the system:

$$B = 2 \bullet \zeta \bullet \sqrt{K \bullet M} \qquad \zeta = .05$$

A.5 Complex Beam Experiments

Several experiments in this thesis use a complex bent beam model in the VES with a PUMA 560 as shown in Figure A-3. The beam modeled is a long hollow cylinder with L_1 and L_2 of 8 meters, a cross sectional radius of 9 centimeters and a wall thickness of 7 millimeters made of aluminum, the equations above produce the following matrices:

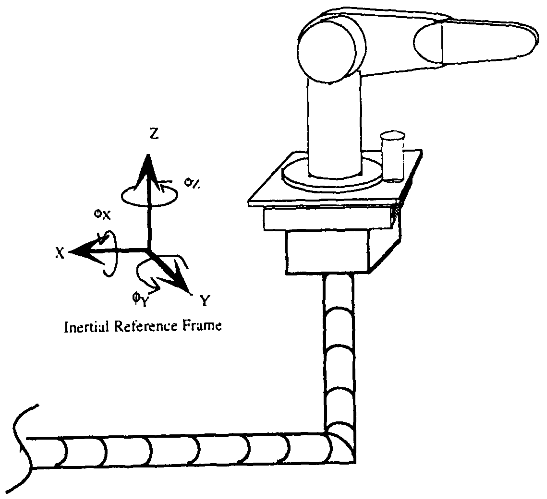

Figure A-3: PUMA Complex Beam

$$\text{Mass Matrix} = \begin{bmatrix} 41\text{ kg} & 0 & 0 & 0 & 0 & 0 \\ 0 & 41\text{ kg} & 0 & 0 & 0 & 0 \\ 0 & 0 & 41\text{ kg} & 0 & 0 & 0 \\ 0 & 0 & 0 & 2600\text{ kg}\cdot\text{m}^2 & 0 & 0 \\ 0 & 0 & 0 & 0 & 2600\text{ kg}\cdot\text{m}^2 & 0 \\ 0 & 0 & 0 & 0 & 0 & 5200\text{ kg}\cdot\text{m}^2 \end{bmatrix}$$

$$\text{Stiffness Matrix} =$$

$$\begin{bmatrix} 976\text{ N/m} & 0 & -770\text{ N/m} & 0 & -3698\text{ N/rad} & 0 \\ 0 & 492\text{ N/m} & 0 & 3093\text{ N/rad} & 0 & 844\text{ N/rad} \\ -770\text{ N/m} & 0 & 1592\text{ N/m} & 0 & 1233\text{ N/rad} & 0 \\ 0 & 3093\text{ N}\cdot\text{m/m} & 0 & 25548\text{ N}\cdot\text{m/rad} & 0 & 5302\text{ N}\cdot\text{m/rad} \\ -3698\text{ N}\cdot\text{m/m} & 0 & 1233\text{ N}\cdot\text{m/m} & 0 & 23013\text{ N}\cdot\text{m/rad} & 0 \\ 0 & 844\text{ N}\cdot\text{m/m} & 0 & 5302\text{ N}\cdot\text{m/rad} & 0 & 7552\text{ N}\cdot\text{m/rad} \end{bmatrix}$$

$$\text{Damping Matrix} = \begin{bmatrix} 15\text{ N/m/s} & 0 & -10\text{ N/m/s} & 0 & -122\text{ N/rad/s} & 0 \\ 0 & 10\text{ N/m/s} & 0 & 94\text{ N/rad/s} & 0 & 41\text{ N/rad/s} \\ -10\text{ N/m/s} & 0 & 34\text{ N/m/s} & 0 & 38\text{ N/rad/s} & 0 \\ 0 & 3\text{ N}\cdot\text{m/m/s} & 0 & 800\text{ N}\cdot\text{m/rad/s} & 0 & 195\text{ N}\cdot\text{m/rad/s} \\ -4\text{ N}\cdot\text{m/m/s} & 0 & 1\text{ N}\cdot\text{m/m/s} & 0 & 775\text{ N}\cdot\text{m/rad/s} & 0 \\ 0 & 1\text{ N}\cdot\text{m/m/s} & 0 & 98\text{ N}\cdot\text{m/rad/s} & 0 & 613\text{ N}\cdot\text{m/rad/s} \end{bmatrix}$$

Appendix B

The Anatomy of a PUMA 560

B.1 Coordinates and Definitions

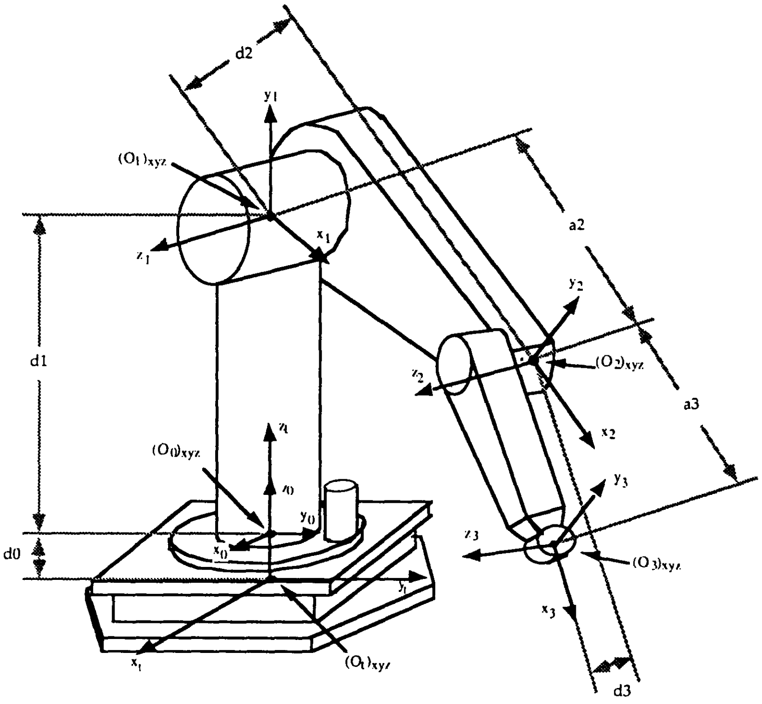

Figure B-1: PUMA 560 D-H Parameters

Denavit-Hartenburg Parameters of the PUMA 560 [Armstrong et. al. 1986]:

d0 =	0.22844 m	d3 =	0.098 m
d1 =	0.672 m	a2 =	0.4318 m
d2 =	-0.2435 m	a3 =	0.4331 m

B.2 Link Masses and Inertias

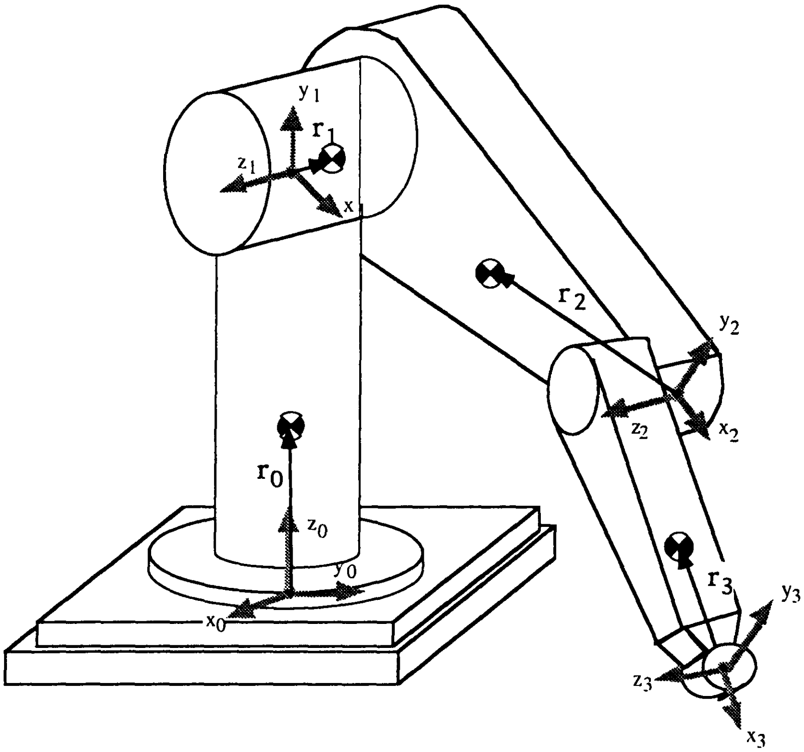

Figure B-2: PUMA 560 link masses and position vectors [Armstrong et. al. 1986]

$$r_0 = \begin{Bmatrix} r_{0x} \\ r_{0y} \\ r_{0z} \end{Bmatrix} = \begin{Bmatrix} 0 \\ 0 \\ 0.283 \end{Bmatrix} \qquad r_1 = \begin{Bmatrix} r_{1x} \\ r_{1y} \\ r_{1z} \end{Bmatrix} = \begin{Bmatrix} 0 \\ 0 \\ -0.056 \end{Bmatrix} \qquad \begin{matrix} M_0 = 54.5 \text{ kg} \\ M_1 = 12.8 \text{ kg} \end{matrix}$$

$$r_2 = \begin{Bmatrix} r_{2x} \\ r_{2y} \\ r_{2z} \end{Bmatrix} = \begin{Bmatrix} -0.364 \\ -0.006 \\ 0.016 \end{Bmatrix} \qquad r_3 = \begin{Bmatrix} r_{3x} \\ r_{3y} \\ r_{3z} \end{Bmatrix} = \begin{Bmatrix} -0.142 \\ 0 \\ 0 \end{Bmatrix} \qquad \begin{matrix} M_2 = 17.4 \text{ kg} \\ M_3 = 9.0 \text{ kg} \end{matrix}$$

$$I_0 = \begin{bmatrix} 6.686 & 0 & 0 \\ 0 & 6.465 & 0 \\ 0 & 0 & 1.815 \end{bmatrix} \qquad I_1 = \begin{bmatrix} 0.615 & 0 & 0 \\ 0 & 0.615 & 0 \\ 0 & 0 & 0.081 \end{bmatrix}$$

$$I_2 = \begin{bmatrix} 0.130 & 0 & 0 \\ 0 & 0.524 & 0 \\ 0 & 0 & 5.249 \end{bmatrix} \qquad I_3 = \begin{bmatrix} 0.015 & 0 & 0 \\ 0 & 0.574 & 0 \\ 0 & 0 & 1.424 \end{bmatrix}$$

B.3 Homogeneous Transformation Matrices

$\left[{}^{t}_{i}A\right]$ is the Homogeneous Transformation Matrix from the i^{th} link frame back to the platform top frame (the PUMA base frame):

$$\left[{}^{t}_{1}A\right] = \begin{bmatrix} c_1 & 0 & s_1 & 0 \\ s_1 & 0 & -c_1 & 0 \\ 0 & 1 & 0 & d_0+d_1 \\ 0 & 0 & 0 & 1 \end{bmatrix}$$

$$\left[{}^{t}_{2}A\right] = \begin{bmatrix} c_1\cdot c_2 & -c_1\cdot s_2 & s_1 & a_2\cdot c_1\cdot c_2+d_2\cdot s_1 \text{ (=a)} \\ s_1\cdot c_2 & -s_1\cdot s_2 & -c_1 & a_2\cdot s_1\cdot c_2-d_2\cdot c_1 \text{ (=b)} \\ s_2 & c_2 & 0 & a_2\cdot s_2+d_0+d_1 \text{ (=c)} \\ 0 & 0 & 0 & 1 \end{bmatrix}$$

$$\left[{}^{t}_{3}A\right] = \begin{bmatrix} c_1\cdot c_{23} & -c_1\cdot s_{23} & s_1 & a_3\cdot c_1\cdot c_{23}+d_3\cdot s_1+a_2\cdot c_1\cdot c_2+d_2\cdot s_1 \text{ (=d)} \\ s_1\cdot c_{23} & -s_1\cdot s_{23} & -c_1 & a_3\cdot s_1\cdot c_{23}-d_3\cdot c_1+a_2\cdot s_1\cdot c_2-d_2\cdot c_1 \text{ (=e)} \\ s_{23} & c_{23} & 0 & a_3\cdot s_{23}+a_2\cdot s_2+d_0+d_1 \text{ (=f)} \\ 0 & 0 & 0 & 1 \end{bmatrix}$$

where the terms:	are defined as:
ci, cj, cij	Cosine of robot joint angles ϑi, ϑj, and ϑi+ϑj.
si, sj, sij	Sine of robot joint angles ϑi, ϑj, and ϑi+ϑj.
d0, d1, d2, a2, a3	Denavit-Hartenburg constants of robot, see Section B.1.

B.4 Jacobian Matrices

The Jacobian matrix to the center of mass of each link, $\mathbf{r}_i$ in the link "i" frame, is shown below.

$$^1J = \begin{Bmatrix} ^1J_{11} \\ ^1J_{12} \\ ^1J_{13} \end{Bmatrix} = \begin{Bmatrix} -r_{1x}\cdot s_1+r_{1z}\cdot c_1 \\ r_{1x}\cdot c_1+r_{1z}\cdot s_1 \\ 0 \end{Bmatrix}$$

$$^2J = \begin{Bmatrix} ^2J_{11} & ^2J_{12} \\ ^2J_{13} & ^2J_{21} \\ ^2J_{22} & ^2J_{23} \end{Bmatrix} = \left\{\begin{array}{l} -r_{2x}\cdot s_1\cdot c_2+r_{2y}\cdot s_1\cdot s_2+r_{2z}\cdot c_1-a_2\cdot s_1\cdot c_2+d_2\cdot c_1 \\ r_{2x}\cdot c_1\cdot c_2-r_{2y}\cdot c_1\cdot s_2+r_{2z}\cdot s_1+a_2\cdot c_1\cdot c_2+d_2\cdot s_1 \\ 0 \\ -r_{2x}\cdot c_1\cdot s_2-r_{2y}\cdot c_1\cdot c_2-a_2\cdot c_1\cdot s_2 \\ -r_{2x}\cdot s_1\cdot s_2-r_{2y}\cdot s_1\cdot c_2-a_2\cdot s_1\cdot s_2 \\ r_{2x}\cdot c_2-r_{2y}\cdot s_2+a_2\cdot c_2 \end{array}\right\}$$

$$^3J = \begin{Bmatrix} ^3J_{11} & ^3J_{12} & ^3J_{13} \\ ^3J_{21} & ^3J_{22} & ^3J_{23} \\ ^3J_{31} & ^3J_{32} & ^3J_{33} \end{Bmatrix} = \left\{\begin{array}{l} -r_{3x}\cdot s_1\cdot c_{23}+r_{3y}\cdot s_1\cdot s_{23}+r_{3z}\cdot c_1-a_3\cdot s_1\cdot c_{23}+d_3\cdot c_1-a_2\cdot s_1\cdot c_2+d_2\cdot c_1 \\ r_{3x}\cdot c_1\cdot c_{23}-r_{3y}\cdot c_1\cdot s_{23}+r_{3z}\cdot s_1+a_3\cdot c_1\cdot c_{23}+d_3\cdot s_1+a_2\cdot c_1\cdot c_2+d_2\cdot s_1 \\ 0 \\ -r_{3x}\cdot c_1\cdot s_{23}-r_{3y}\cdot c_1\cdot c_{23}-a_3\cdot c_1\cdot s_{23}-a_2\cdot c_1\cdot s_2 \\ -r_{3x}\cdot s_1\cdot s_{23}-r_{3y}\cdot s_1\cdot c_{23}-a_3\cdot s_1\cdot s_{23}-a_2\cdot s_1\cdot s_2 \\ r_{3x}\cdot c_{23}-r_{3y}\cdot s_{23}+a_3\cdot c_{23}+a_2\cdot c_2 \\ \\ -r_{3x}\cdot c_1\cdot s_{23}-r_{3y}\cdot c_1\cdot c_{23}-a_3\cdot c_1\cdot s_{23} \\ -r_{3x}\cdot s_1\cdot s_{23}-r_{3y}\cdot s_1\cdot c_{23}-a_3\cdot s_1\cdot s_{23} \\ r_{3x}\cdot c_{23}-r_{3y}\cdot s_{23}+a_3\cdot c_{23} \end{array}\right\}$$

B.5 Virtual Manipulator to Endpoint

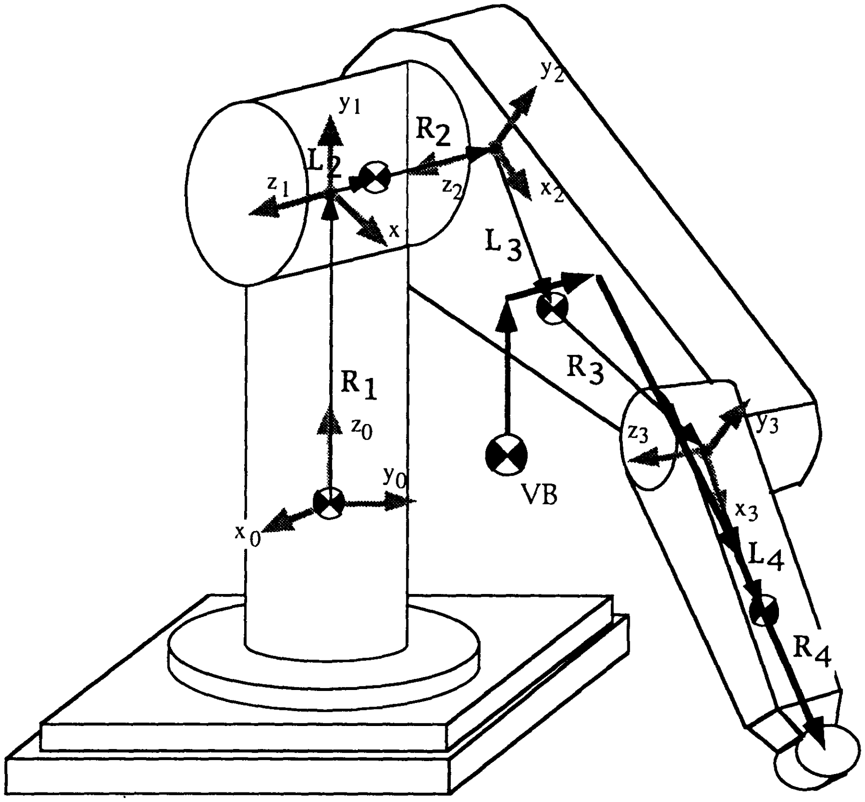

Figure B-3: PUMA 560 Virtual Manipulator to Endpoint

R1 = {0,0,0.629}

M1 = 54.5

L2 = {0,0,-0.056}

R2 = {0,0,-0.1875}

M2 = 12.8

L3 = {0.068,-0.006,0.016}

R3 = {0.364,0.006,0.082}

M3 = 17.4

L4 = {0.2911,0,0}

R4 = {0.142,0,0}

M4 = 9.0

Mtot = 93.4 kg

r1 = **R1** * M1/Mtot = {0,0,0.366}

l2 = **L2** * M1/Mtot = {0,0,-0.032}

r2 = **R2** * (M1+M2)/Mtot = {0,0,-0.135}

l3 = **L3** * (M1+M2)/Mtot = {0.0488,-0.0043,0.0115}

r3 = **R3** * (M1+M2+M3)/Mtot = {.329,0.0043,0.074}

l4 = **L4** * (M1+M2+M3)/Mtot = {0.263,0,0}

r4 = **R4** * (M1+M2+M3+M4)/Mtot = {.142,0,0}

V1 = **r1** = {0,0,0.215}

V2 = **r2** + **l2**= {0,0,-0.175}

V3 = **r3** + **l3**= {0.377,0,0.0855}

V4 = **r4** + **l4**= {0.405,0,0}

* The Virtual Manipulator concept is presented by [Vafa 1987, Vafa and Dubowsky 1990]

B.6 Virtual Manipulator to Base

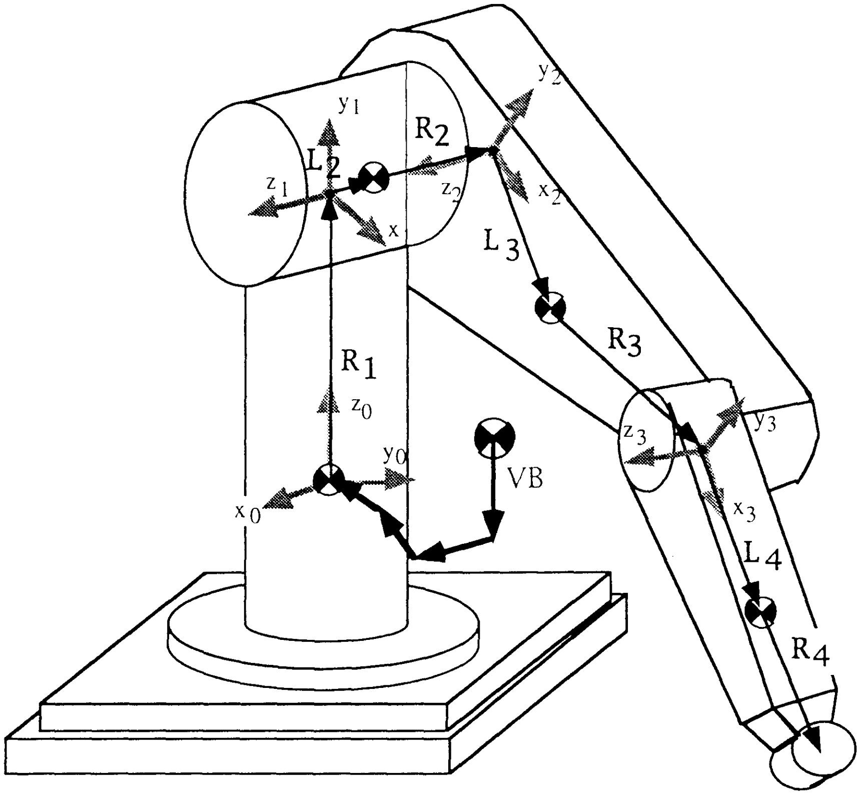

Figure B-4: PUMA 560 Virtual Manipulator to Base

$V1 = \mathbf{r1} - \mathbf{R1} = \{0,0,-0.263\}$

$V2 = \mathbf{r2} + \mathbf{l2} - \mathbf{R2} - \mathbf{L2} = \{0,0,0.0765\}$

$V3 = \mathbf{r3} + \mathbf{l3} - \mathbf{R3} - \mathbf{L3} = \{-0.054,0,-0.0125\}$

$V4 = \mathbf{r4} + \mathbf{l4} - \mathbf{R4} - \mathbf{L4} = \{-0.0281,0,0\}$

D-H Parameters of Virtual Manipulator:

$d1 = -0.263$

$d2 = 0.0765$

$d3 = -0.0125$

$a2 = -0.054$

$a3 = -0.0281$

Appendix C

Modeling a PUMA 560

C.1 Introduction

This section presents the equations and calculations required to form a minimal model of a PUMA 560, in the form presented in Chapter 3. Recall that the only manipulator model required to predict gravitational forces is the total mass of the manipulator system. This procedure is exactly the same for any manipulator system. The P vector which forms the manipulator model required to predict gravitational moments, and the corresponding G matrix, change for different manipulator geometries. Therefore, if a unique manipulator system is to be used, the analysis presented in this section must be repeated.

C.2 Evaluating the P vector

A formula for the moment at the base of a general manipulator was presented as Equation 3.6:

$$\mathbf{M_g} = \begin{Bmatrix} M_x \\ M_y \\ M_z \end{Bmatrix} = \sum_{i=0}^{n} \begin{bmatrix} 1 & 0 & 0 & 0 \\ 0 & 1 & 0 & 0 \\ 0 & 0 & 1 & 0 \end{bmatrix} \cdot \left[{}_{i}^{b}A \right] \cdot \begin{Bmatrix} r_{ix} \\ r_{iy} \\ r_{iz} \end{Bmatrix} \times (m_i) \cdot \begin{Bmatrix} {}^{b}g_x \\ {}^{b}g_y \\ {}^{b}g_z \end{Bmatrix}$$

For the PUMA 560, the homogeneous transformation matrices presented in Appendix B can be used to evaluate this equation:

$$m_0 \cdot \begin{Bmatrix} r_{0x} \\ r_{0y} \\ r_{0z} \end{Bmatrix} \times \begin{Bmatrix} g_x \\ g_y \\ g_z \end{Bmatrix} \Rightarrow$$

$$\begin{aligned} &m_0 \cdot (r_{0y} \cdot g_z - r_{0z} \cdot g_y)\hat{i} \ - \\ &m_0 \cdot (r_{0x} \cdot g_z - r_{0z} \cdot g_x)\hat{j} \ + \\ &m_0 \cdot (r_{0x} \cdot g_y - r_{0y} \cdot g_x)\hat{k} \end{aligned}$$

$$m_1 \cdot \begin{Bmatrix} r_{1x} \cdot c_1 + r_{1z} \cdot s_1 \\ r_{1x} \cdot s_1 - r_{1z} \cdot c_1 \\ r_{1y} \end{Bmatrix} \times \begin{Bmatrix} g_x \\ g_y \\ g_z \end{Bmatrix} \Rightarrow$$

$$\begin{aligned} &m_1 \cdot \Big((r_{1x} \cdot s_1 - r_{1z} \cdot c_1) \cdot g_z - r_{1y} \cdot g_y\Big)\hat{i} \ - \\ &m_1 \cdot \Big((r_{1x} \cdot c_1 - r_{1z} \cdot s_1) \cdot g_z - r_{1y} \cdot g_x\Big)\hat{j} \ + \\ &m_1 \cdot \Big((r_{1x} \cdot c_1 + r_{1z} \cdot s_1) \cdot g_y - (r_{1x} \cdot s_1 - r_{1z} \cdot c_1) \cdot g_x\Big)\hat{k} \end{aligned}$$

$$m_2 \cdot \begin{Bmatrix} r_{2x} \cdot c_1 \cdot c_2 - r_{2y} \cdot c_1 \cdot s_2 + r_{2z} \cdot s_1 + a \\ r_{2x} \cdot s_1 \cdot c_2 - r_{2y} \cdot s_1 \cdot s_2 - r_{2z} \cdot c_1 + b \\ r_{2x} \cdot s_2 + r_{2y} \cdot c_2 + c \end{Bmatrix} \times \begin{Bmatrix} g_x \\ g_y \\ g_z \end{Bmatrix} \Rightarrow$$

$$\begin{aligned} &m_2 \cdot \Big((r_{2x} \cdot s_1 \cdot c_2 - r_{2y} \cdot s_1 \cdot s_2 - r_{2z} \cdot c_1 + b) \cdot g_z + (-r_{2x} \cdot s_2 - r_{2y} \cdot c_2 - c) \cdot g_y\Big)\hat{i} \ - \\ &m_2 \cdot \Big((r_{2x} \cdot c_1 \cdot c_2 - r_{2y} \cdot c_1 \cdot s_2 + r_{2z} \cdot s_1 - a) \cdot g_z + (-r_{2x} \cdot s_2 - r_{2y} \cdot c_2 + c) \cdot g_x\Big)\hat{j} \ - \\ &m_2 \cdot \Big((r_{2x} \cdot c_1 \cdot c_2 - r_{2y} \cdot c_1 \cdot s_2 + r_{2z} \cdot s_1 + a) \cdot g_y - (r_{2x} \cdot s_1 \cdot c_2 - r_{2y} \cdot s_1 \cdot s_2 - r_{2z} \cdot c_1 + b) \cdot g_x\Big)\hat{k} \end{aligned}$$

$$m_3 \cdot \begin{Bmatrix} r_{3x} \cdot c_1 \cdot c_{23} - r_{3y} \cdot c_1 \cdot s_{23} + r_{3z} \cdot s_1 + d \\ r_{3x} \cdot s_1 \cdot c_{23} - r_{3y} \cdot s_1 \cdot s_{23} - r_{3z} \cdot c_1 + e \\ r_{3x} \cdot s_{23} + r_{3y} \cdot c_{23} + f \end{Bmatrix} \times \begin{Bmatrix} g_x \\ g_y \\ g_z \end{Bmatrix} \Rightarrow$$

$$\begin{aligned} &m_3 \cdot \Big((r_{3x} \cdot s_1 \cdot c_{23} - r_{3y} \cdot s_1 \cdot s_{23} - r_{3z} \cdot c_1 + e) \cdot g_z + (-r_{3x} \cdot s_{23} - r_{3y} \cdot c_{23} + f) \cdot g_y\Big)\hat{i} \ - \\ &m_3 \cdot \Big((r_{3x} \cdot c_1 \cdot c_{23} - r_{3y} \cdot c_1 \cdot s_{23} + r_{3z} \cdot s_1 + d) \cdot g_z + (-r_{3x} \cdot s_{23} - r_{3y} \cdot c_{23} + f) \cdot g_x\Big)\hat{j} \ - \\ &m_3 \cdot \Big((r_{3x} \cdot c_1 \cdot c_{23} - r_{3y} \cdot c_1 \cdot s_{23} + r_{3z} \cdot s_1 + d) \cdot g_y - (r_{3x} \cdot s_1 \cdot c_{23} - r_{3y} \cdot s_1 \cdot s_{23} - r_{3z} \cdot c_1 + e) \cdot g_x\Big)\hat{k} \end{aligned}$$

The three separate equations (one each for M_x, M_y, and M_z) can be arranged into a simplified linear matrix form:

$$\mathbf{M_g} = [W] \cdot \mathbf{Q}$$

where

$$[W] = \left[\begin{array}{ccc|ccc} 0 & gz & -gy & s1 \cdot gz & -gy & -c1 \cdot gz \\ -gz & 0 & gx & -c1 \cdot gz & gx & -s1 \cdot gz \\ gy & -gx & 0 & c1 \cdot gy - s1 \cdot gx & 0 & s1 \cdot gy + c1 \cdot gx \end{array}\right|$$

$$\left|\begin{array}{ccc} s1 \cdot c2 \cdot gz - s2 \cdot gy & -s1 \cdot s2 \cdot gz - c2 \cdot gy & -c1 \cdot gz \\ -c1 \cdot c2 \cdot gz + s2 \cdot gx & c1 \cdot s2 \cdot gz + c2 \cdot gx & -s1 \cdot gz \\ c1 \cdot c2 \cdot gy - s1 \cdot c2 \cdot gx & -c1 \cdot s2 \cdot gy + s1 \cdot s2 \cdot gx & s1 \cdot gy + c1 \cdot gx \end{array}\right|$$

$$\left|\begin{array}{ccc} s1 \cdot c23 \cdot gz - s23 \cdot gy & -s1 \cdot s23 \cdot gz - c23 \cdot gy & -c1 \cdot gz \\ -c1 \cdot c23 \cdot gz + s23 \cdot gx & c1 \cdot s23 \cdot gz + c23 \cdot gx & -s1 \cdot gz \\ c1 \cdot c23 \cdot gy - s1 \cdot c23 \cdot gx & -c1 \cdot s23 \cdot gy + s1 \cdot s23 \cdot gx & s1 \cdot gy + c1 \cdot gx \end{array}\right]$$

$$Q = \left[\begin{array}{l} m0 \cdot r0x \\ m0 \cdot r0y \\ m0 \cdot r0z + m0 \cdot d0 \\ m1 \cdot r1x \\ m1 \cdot r1y + (m1+m2+m3) \cdot (d0+d1) \\ m1 \cdot r1z \\ m2 \cdot r2x + (m2+m3) \cdot a2 \\ m2 \cdot r2y \\ m2 \cdot r2z + (m2+m3) \cdot d2 \\ m3 \cdot r3x + m3 \cdot a3 \\ m3 \cdot r3y \\ m3 \cdot r3z + m3 \cdot d3 \end{array}\right]$$

When linearly independent columns are removed:

$$\mathbf{M_g} = [G] \cdot \mathbf{P}$$

$$[G] = \left[\begin{array}{ccc|cc} 0 & gz & -gy & s1\cdot gz & -c1\cdot gz \\ -gz & 0 & gx & -c1\cdot gz & -s1\cdot gz \\ gy & -gx & 0 & c1\cdot gy - s1\cdot gx & s1\cdot gy + c1\cdot gx \end{array} \right.$$

$$\begin{array}{c|c} s1\cdot c2\cdot gz - s2\cdot gy & -s1\cdot s2\cdot gz - c2\cdot gy \\ -c1\cdot c2\cdot gz + s2\cdot gx & c1\cdot s2\cdot gz + c2\cdot gx \\ c1\cdot c2\cdot gy - s1\cdot c2\cdot gx & -c1\cdot s2\cdot gy + s1\cdot s2\cdot gx \end{array}$$

$$\left. \begin{array}{cc} s1\cdot c23\cdot gz - s23\cdot gy & -s1\cdot s23\cdot gz - c23\cdot gy \\ -c1\cdot c23\cdot gz + s23\cdot gx & c1\cdot s23\cdot gz + c23\cdot gx \\ c1\cdot c23\cdot gy - s1\cdot c23\cdot gx & -c1\cdot s23\cdot gy + s1\cdot s23\cdot gx \end{array} \right]$$

$$\mathbf{P} = \left[\begin{array}{l} m0\cdot r0x \\ m0\cdot r0y \\ m0\cdot r0z + m1\cdot r1y + m0\cdot d0 + (m1+m2+m3)\cdot(d0+d1) \\ m1\cdot r1x \\ m1\cdot r1z + m2\cdot r2z + (m2+m3)\cdot d2 + m3\cdot r3z + m3\cdot d3 \\ m2\cdot r2x + (m2+m3)\cdot a2 \\ m2\cdot r2y \\ m3\cdot r3x + m3\cdot a3 \\ m3\cdot r3y \end{array} \right]$$

where the terms:	are defined as:
gx, gx, gz	Gravity vector in platform top frame, see Equation 3.4
ci, cj, cij	Cosine of PUMA joint angles ϑi, ϑj, and ϑi+ϑj.
si, sj, sij	Sine of PUMA joint angles ϑi, ϑj, and ϑi+ϑj.
d0, d1, d2, a2, a3	Denavit-Hartenburg constants of robot, see Appendix B.
rij	The "j" axis component of link "i" center of mass in link "i" coordinate frame.
mi	Mass of link "i".

C.3 Experimental Versus Measured Mass Parameters

The experimentally determined values for the P vector are compared to values found by disassembly and measurement [Armstrong et al. 1986].

	Experimentally Determined Values	Physically Measured Values
M_{total}:	95.065 kg	93.678 kg
$\bar{P}$ [1:	0.1028 kg-m	0 kg-m
2:	0.8352 kg-m	0 kg-m
3:	45.7104 kg-m	54.54 kg-m
4:	0.1593 kg-m	0 kg-m
5:	-5.8440 kg-m	-5.308 kg-m
6:	4.6137 kg-m	5.065 kg-m
7:	0.1298 kg-m	-0.1044 kg-m
8:	2.2527 kg-m	2.617 kg-m
9:]	-0.0738 kg-m	0 kg-m

Appendix D

Coordinate Frame Transformation

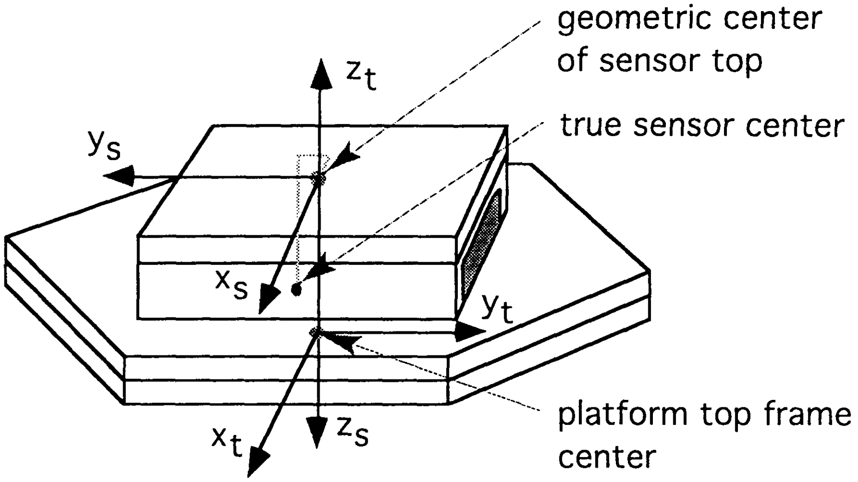

Figure D-1: Coordinate frame relationships

The coordinate center of measurements provided by the force sensor is not located at the geometric center of the force sensor top, as show in Figure D-1. Since the sensor frame and the top plate frame are orthogonal, the force readings have the same magnitude in both frames. Converting from the sensor frame to the platform top frame requires adding the moment components resulting from the offset of the two frames:

$$
\begin{aligned}
Fx_t &= Fx_s \\
Fy_t &= -Fy_s \\
Fz_t &= -Fz_s \\
Mx_t &= Mx_s - Fz_s \cdot {}^t y_0 + Fy_s \cdot {}^t z_0 \\
My_t &= -My_s + Fz_s \cdot {}^t x_0 + Fx_s \cdot {}^t z_0 \\
Mz_t &= -Mz_s - Fy_s \cdot {}^t x_0 + Fx_s \cdot {}^t y_0
\end{aligned}
\tag{D.1}
$$

where ${}^t x_0 = -0.001$ m , ${}^t y_0 = -0.00066$ m, ${}^t z_0 = 0.18944$

Appendix E

The VES Micro-Gravity Handbook

E.1 Introduction

This Appendix describes in detail the procedures and precautions for running the VES II system with the PUMA 560 to perform micro-gravity emulation experiments. A summary of the steps required for a typical experiment is followed by a details of each step. Charts are provided in Section 5.5 to determine platform gains for a desired bandwidth.

E.2 VES II Basic Rules

The VES II is a powerful machine and its operation for micro-gravity emulation requires the coordination of two computers. There are many small mistakes which can cause the computers to lock up, loosing communication and control of the platform. Caution should always be exercised while operating the VES and it should be watched constantly as long as the safety valves are open and its position is being controlled by the hardware. The most important thing to remember while operating the VES is:

Rule #1: If in doubt, press the panic button to freeze the platform.

Panic buttons are located on the main control crate and in the room with the VES II. After freezing the platform, follow the *VES II Freeze Recovery Procedure* below

The PUMA 560 is usually controlled by the PMAC with the built in VAL controller standing by in free mode. If the power to the PMAC is shut off while the VAL controller is in free mode, the PUMA 560 will collapse causing damage to itself and possibly the VES II.

Rule #2: **Do not shut off the crate power (even briefly) without pressing the PUMA 560 panic button.**

The PUMA 560 panic button is located on the modified teach pendant/control module.

E.3 Basic Operating Procedures

VES II Start Up Procedures

Note: This procedure assumes that the platform is starting in the sleep position (all legs retracted).

1) Calibrate the PUMA 560 position with VAL.

Turn the Unimation box power on with the switch on the control box. The VAL monitor (connected to the Unimation box) will display an initialization message.

Type "Y" and "return" twice to initialize VAL. The teach pendant will display "No High Power".

Release the panic button and press the black power button to provide power to the PUMA. (The PUMA can now be operated in joint mode, etc.)

Press "comp" on the teach pendant to put the PUMA into computer mode.

On the VAL monitor keyboard type "CA" for calibrate. The PUMA will move each joint a short distance.

Type "speed 15" to limit the motion speed. Then type "do ready" to move the PUMA to its home position.

2) Boot up the Redslave, Blueslave and PMAC

Switch the power to the Huerikon crate to "on". The Redslave, Blueslave and PMAC will boot automatically. Terminals can be connected to the Redslave or Blueslave through the back of the crate to monitor the boot up procedure.

The Redslave and Blueslave boot up process takes a minute or two.

3) Run "loadmkb" program on the Sun

In a Sun command window, move to the /home/platform/bin directory.

Type "loadmkb", to run the program which allows you to transfer admittance models from the Sun to the Redslave.

NOTE: This program must be started before the "testPlatform" program is run or it will lock up the computers. Once "loadmkb" is started it can be used to transfer new admittance models while "testPlatform" is running, but when it is first started it sends default information to the Redslave which will not work if the platform is already running.

4) Set up the Redslave and Blueslave

In a Sun command window, type "rlogin blueslave" to remotely log into the Blueslave. (the alias "blue" can be used)

In another Sun command window, type "rlogin redslave" to remotely log into the Redslave. (the alias "red" can be used)

In the Redslave window, type "sendShMemArray" to define the array of shared memory variables and set up memory sharing between the Redslave and Blueslave.

5) Run "PumaMove" and move the PUMA to a safe position

In the Blueslave window type "ld < PumaStuff" to load the PUMA control software.

Type "PumaMove" to run the PUMA control software.

On the PUMA control box, release the panic button and press the arm power button. Press the "free" button, and switch levers "1", "2" and "3" to the "+" symbol to release the first three joints from VAL control.

Doing this will normally cause the joints to fall down, but when the "PumaMove" software is initialized, it configures the PMAC to control the first three joints.

At the main menu, choose "1 Robot Control".

Move joint #2 to 0 or 180 degrees.

NOTE: The PUMA must be in its home position when the PMAC is started or the joint encoders will not be properly zeroed. The PUMA must then be moved away from its home position before the platform is moved or it will crash through the ceiling when the platform moves to its home position.

6) Run "testPlatform" and start the platform

Make sure the red panic button on the platform control cart is pushed.

Start the hydraulic pump by pulling forward on the lever arm and then quickly slamming it back as far as it will go.

In the Redslave window type "testPlatform" to run the platform control software.

At the K1 and K2 gain prompts type any numbers and hit return. THE PANIC BUTTON MUST BE PRESSED. This step makes the platform try to start while the panic button is pressed. This functions as a quick check of the platform safety routines. Error messages should appear saying that the pressure is too low and the panic button is pressed. If no error messages appear make sure the shared memory array has been sent or start over.

Type cntrl-C to break out of the error messages.

Type "testPlatform" again.

Choose K1 and K2 gains based on bandwidth requirements and the charts in Section 5.5. BEFORE HITTING RETURN AFTER GAIN K2: keep your hand near the platform panic button, if anything will go wrong, this is a likely time. Hit return for gain K2, and watch the platform and control cart carefully for several seconds. (1) The platform should not move AT ALL. (2) The lights on the legslave boards should remain on. (3) The lights on the top row of current amplifier boards should go on. (4) the main platform control menu should appear on the Redslave window. If any of that does not happen, hit the panic button and start step six over.

NOTE: A loud popping noise will be heard and the platform may shake slightly as the safety valves and solenoids open. This is normal.

The platform is now under closed loop control in Idle mode.

7) Set the platActive flag

In the Blueslave window, choose "1 toggle platActive flag" to toggle the platActive flag to "1". This flag tells the PumaMove software that the platform is active and is passing force sensor information via shared memory.

NOTE: While the platform is running, it must constantly read the Data Translation board to monitor the hydraulic fluid manifold pressure. If a routine which reads the force sensor is run while the platform is running, both the Redslave and Blueslave will be trying to read the Data Translation board at the same time. This will lock up both computers.

8) Load a calibration matrix and mass parameter vector

In the Blueslave window, choose "2 Load calibration matrix and P vector". At the prompts choose the name of the most recent calibration matrix and mass parameter vector. (e.g. "mass15.dat" and "cal15.dat")

9) Zero the force sensor

In the Blueslave window, choose "3 Zero the force sensor", then choose "2 puma". This will set the zero of the force sensor based on the gravity wrench estimate.

10) Verify the Gravity Compensation

In the Blueslave window, choose "4 Show measured and estimated wrench". This option displays both the force sensor readings and the gravity wrench estimation. These should be very close since the force sensor was just zeroed based on the estimate.

While in the Gravity Comp Test Menu, the PUMA can be moved to new positions (option 1) and the new actual and estimated wrench can be checked for estimation accuracy (option 3).

11) Run the experiments

Follow procedures for either a spline motion or random motion experiment below.

Micro-Gravity Spline Motions

1) Set up and test the spline motion

In the Blueslave window, at the Main Menu, choose "2 Spline Motion".

At the Spline Move Menu, choose "3 Load a Spline File", and type the name of a file containing the spline to be run. NOTE: All spline files should be located in "/home/pmac/puma/GCdata".

Set the speed of the spline. (1=full speed, 2=half speed...)

Make sure the platform is in a low position (preferably the sleep position)

Run the spline and watch to make sure that there will be plenty of room around the PUMA when the platform is moved to its home position. NOTE: If extra room is needed, the home position of the experiment can be lowered, see step 4 note.

2) Set up data collection

In the Redslave window, choose "4 data setup".

Turn on data collection, set a data collection rate (1=every cycle, 2=every other cycle), and select the data to be collected (forces, positions, etc.). If desired set the flag to coordinate data recording with the beginning of the experiment.

3) Set up admittance model

The admittance model for the experiment should be created (see appendix A) and stored in "/home/platform/bin/admModels"

On the Sun, in the "loadmkb" program window, enter the name of the model and the sampling rate which the experiment will run at. NOTE: decoupled models ≈ 85 Hz, beam models ≈ 80 Hz, coupled models ≈ 75 Hz.

4) Run gravity compensation

In the Redslave window, choose "6 Active Gravity Comp". NOTE: If the platform has not been moved yet, it will move to the home position first.

Select the type of model being used - decoupled, coupled, or beam.

Set the sampling rate to the same value used in step 3.

Type "0" and return to run the admittance model in micro-gravity. NOTE: The platform will not move until it receives a signal from the Blueslave.

NOTE: If extra room is required for the experiment, the platform home position can be shifted down. Choose "3 MKB model", then choose "6 Set Z offset", choose an offset (e.g. -.15m) to define a new home position. Exit to the Main Menu. Choose "1 Ramp the Platform" and move the platform to the new home position.

5) Run micro-gravity spline

In the Blueslave window, make sure that all the parameters were properly set per step 1 above. Be sure to set delay time before and after the experiment to see the base motion.

Select "9 Do It" to run the spline, the platform will start to move.

6) Reset the platform

If the experiment was successful, in the Redslave window choose "4 Data Setup", and then "11 Record Data" to record platform data from the experiment.

In the Redslave window, choose "1 Ramp the Platform" and move the platform to the home position for the next experiment.

Micro-Gravity Teleoperated Motions

1) Set up platform

Follow steps 2, 3 and 4 of *VES II Spline Motion Experiments* to set up data collection, load an admittance model, and start gravity compensation on the platform.

2) Run gravity compensation and move the PUMA

In the Blueslave window choose "5 Run Gravity Compensation"

Enter the amount of time you would like to run gravity compensation.

If you would like to move the PUMA during the experiment, push the "joint" button on the PUMA controller, and select "1 release PUMA to VAL control" in the Blueslave window.

The platform will start moving. The PUMA can be moved with the PUMA controller.

When the time has expired, type a key and return to re-establish PMAC control of the PUMA, then put the PUMA in free mode (see step 5 of *VES II Start Up Procedures.*

3) Reset the platform

Follow step 6 of *VES II Spline Motion Experiments* .

VES II Shut Down Procedures

1) Move the platform to sleep position

In the Redslave window, choose "0 quit". The platform will then prepare to move to the home position (all legs half extended). Make sure the PUMA will not hit the ceiling during this motion. Type "0" and return to allow the motion. The platform will then prepare to move to the sleep position (all legs retracted). Type "0" and return to allow the motion.

2) Shut down the platform

Press the panic button.

Press the pump motor kill button, which is located next to the panic button on the platform control crate.

3) Move the PUMA to its home position

In the Blueslave window, go to the Manual Mode Menu and move the PUMA joints to 180°,90°,0°. The next time the VES II is started, the calibration procedure will not be necessary.

4) Shut down the PUMA

Press the panic button on the PUMA controller.
Shut off the power switch on the PUMA controller.

5) Shut down the Redslave, Blueslave and PMAC

Switch off the power on the Huerikon crate.

NOTE: If the platform will not be run again for some time, shut off the power to the legslave boards, the temposonics cards, and the current amplifiers. The switches are located at the back of the platform control crate.

VES II Freeze Recovery Procedures

Note: This procedure assumes that the platform was frozen by pressing the panic button.

1) If communications are locked, reboot

If communication with the Redslave and/or Blueslave were locked up: press the panic button on the PUMA controller, then reboot the Huerikon crate.

2) Restart the platform

In the Redslave window, type cntrl-C to break out of the platform control software. If the computers were just rebooted, perform step 4) of the VES II Start Up Procedures.

Start the platform by performing step 6) of the VES II Start Up Procedures.

3) Move the platform to sleep position

Perform step 1) of the VES II Shut Down Procedures.

If the PUMA will hit the ceiling, start the PUMA and use the VAL controller in joint mode to move the PUMA to a safe position.

4) Start over

Perform the VES II Start Up Procedures from the beginning. NOTE: Be sure to reboot the PMAC if (1) the PUMA was moved under VAL control, or (2) the PMAC was rebooted with the PUMA not in its home position.

E.4 Laboratory Arrangement

In the summer of 1994, the VES was moved down the hall to a new laboratory space. Figure E-1 shows the arrangement of the platform in the new laboratory. This figure is a revision of Figure 4.4 in [Kuklinski 1993].

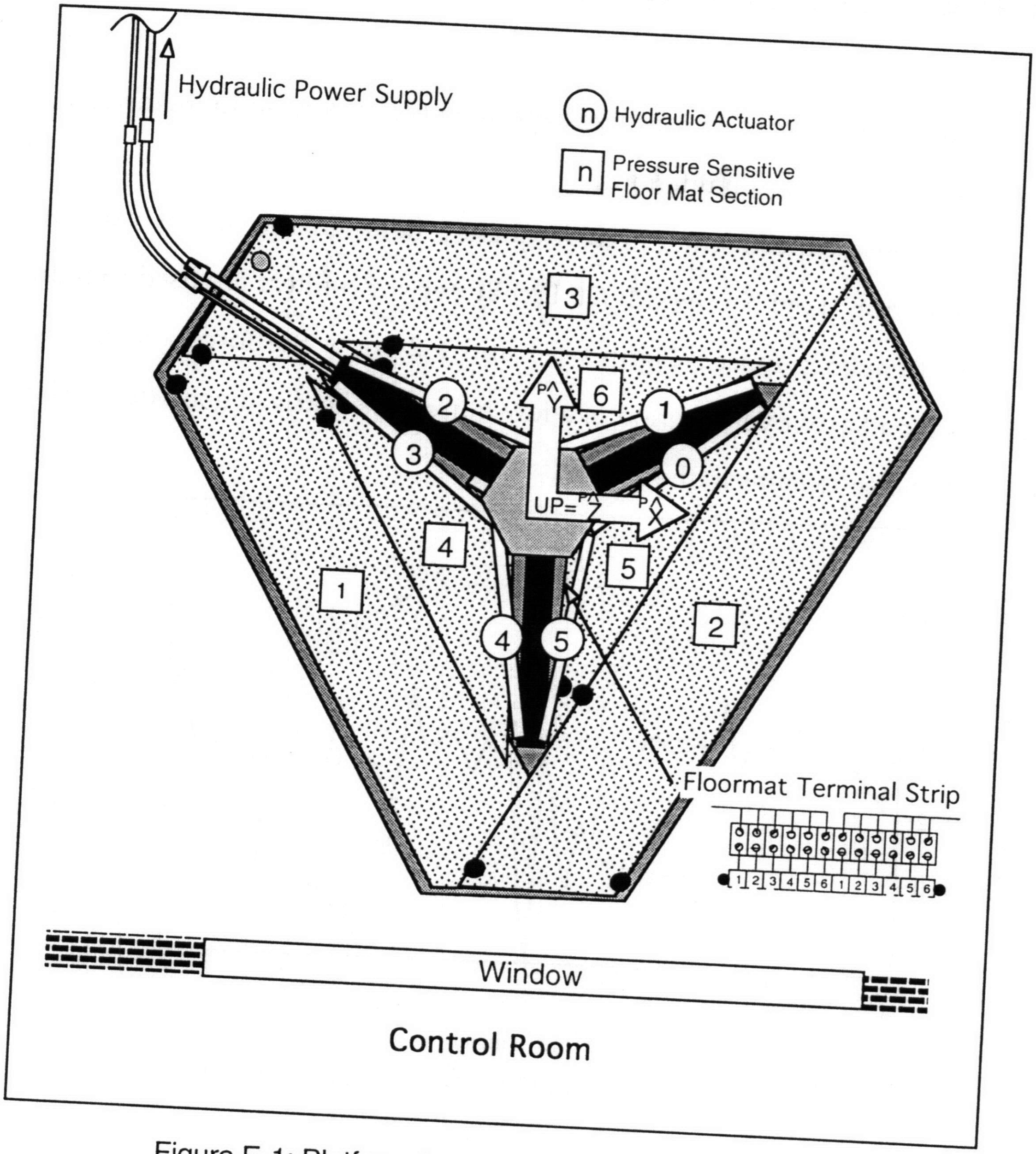

Figure E-1: Platform Arrangement in New Laboratory

Appendix F

Force Sensor Noise

The force sensor used for these experiments is a very accurate instrument. It does, however, have it limitations.

For these experiments, high frequency noise in the sensor can cause significant error. Low bandwidth (20 Hz) Butterworth filters are used to reduce this high frequency noise. Figures F-1 and F-2 show the force and moment readings for all axes over a period of a few minutes. Clearly, a good deal of high frequency noise remains in the system.

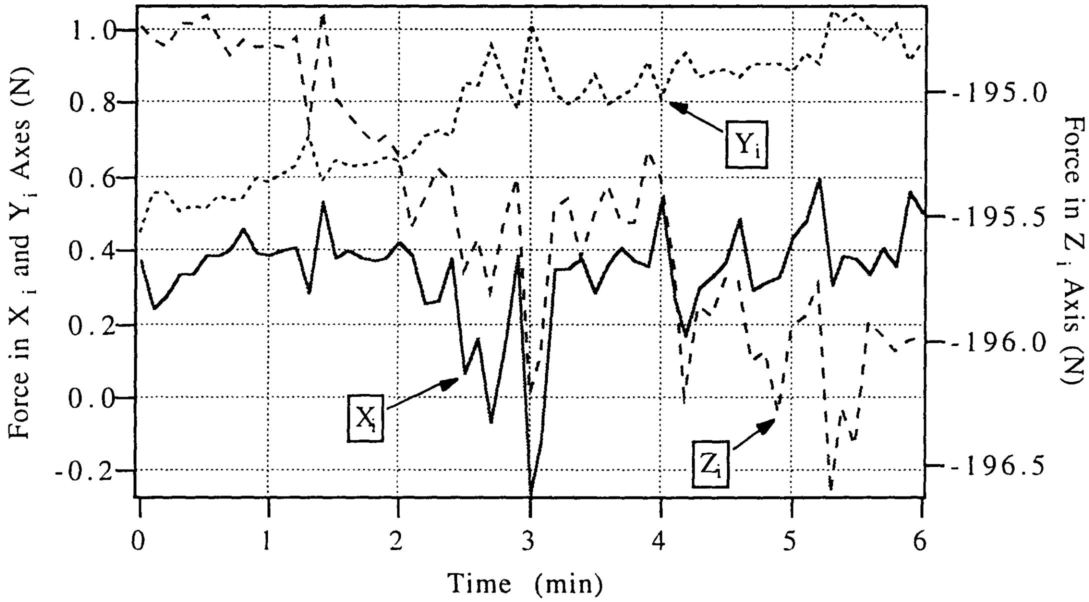

Figure F-1: High Frequency Sensor Noise - Force

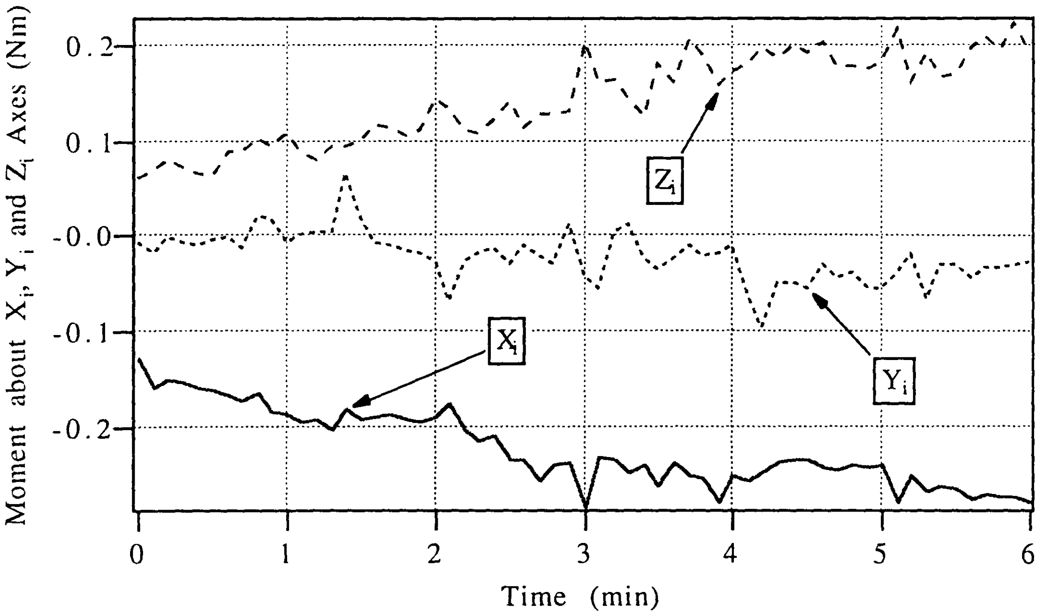

Figure F-2: High Frequency Sensor Noise - Moment

Very low frequency drift in the force sensor can also degrade the quality of this work. If the force sensor is zeroed often during an experiment, this is not a significant problem. Figure F-3 and F-4 show the force and moment readings of all the axes over a period of 8 hours. A serious drift in the sensor readings is apparent.

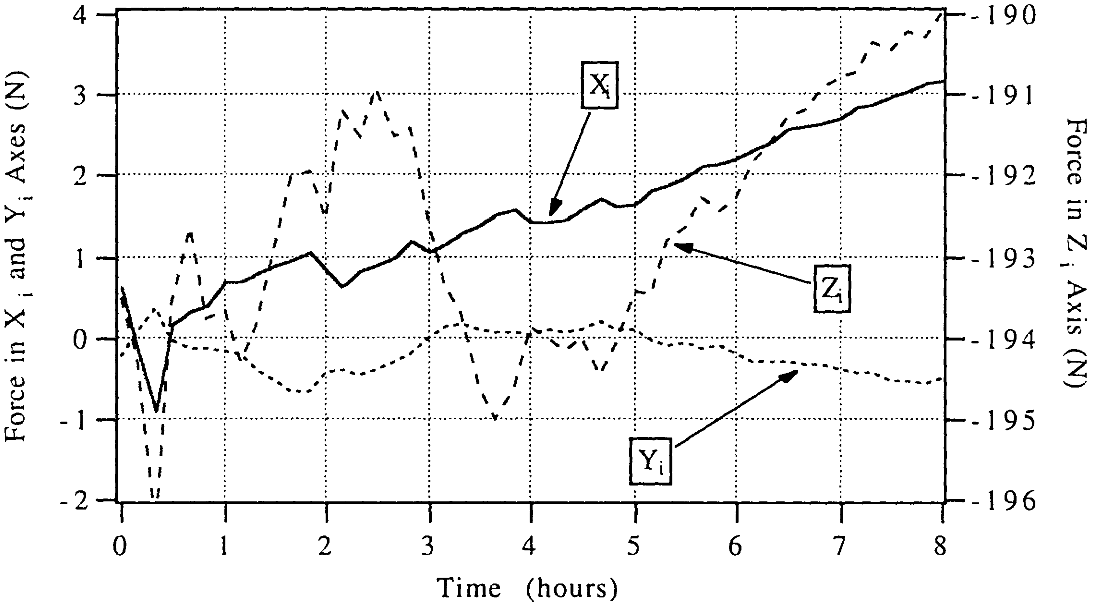

Figure F-3: Low Frequency Sensor Noise - Force

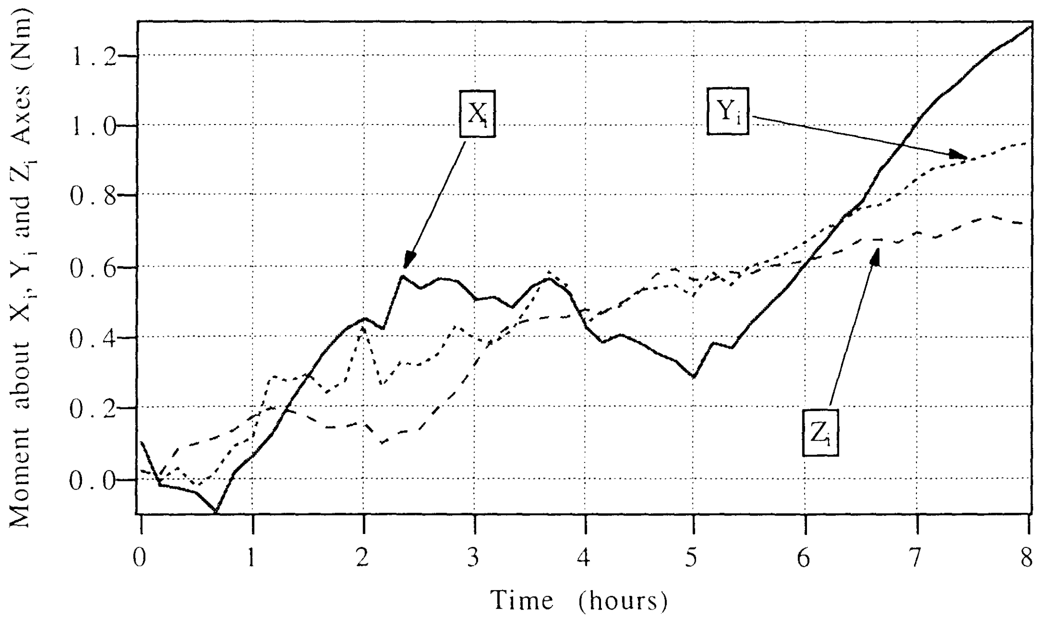

Figure F-4: Low Frequency Sensor Noise - Moment

Appendix G

Linearized Dynamic Model of PUMA on a Flexible Base

Introduction

An analysis of the full dynamic model of a PUMA 560 on a flexible base in zero gravity was conducted to allow calculation of joint controller gains for PPED, see Section 4.3.2. The flexible base is represented by mass, spring, and damper matrices called an admittance model, see Appendix A. Lagrange's equation was used to construct the model. The nonlinear corriolis and centrifugal forces were ignored to simplify the analysis.

The Model

18 state variables are required for this system:

q1, q2, q3 are the PUMA joint angles,

X, Y, Z, α, β, γ, are the translation and rotation of the PUMA base

The kinetic co-energy and potential energy of the system can be written:

$$
\begin{aligned}
T^* = \ & \frac{1}{2}\cdot M_b \cdot \begin{Bmatrix} \dot{X}^2 \\ \dot{Y}^2 \\ \dot{Z}^2 \end{Bmatrix} + \frac{1}{2}\cdot M_0 \cdot \left\{ \begin{Bmatrix} \dot{X} \\ \dot{Y} \\ \dot{Z} \end{Bmatrix} + \begin{Bmatrix} \dot{\alpha} \\ \dot{\beta} \\ \dot{\gamma} \end{Bmatrix} \times {}^{b}\mathbf{r}_0 \right\}^2 + \\
& \frac{1}{2}\cdot M_1 \cdot \left\{ \begin{Bmatrix} \dot{X} \\ \dot{Y} \\ \dot{Z} \end{Bmatrix} + \begin{Bmatrix} \dot{\alpha} \\ \dot{\beta} \\ \dot{\gamma} \end{Bmatrix} \times {}^{b}\mathbf{r}_1 + \left[J_1\right] \cdot \dot{q}_1 \right\}^2 + \\
& \frac{1}{2}\cdot M_2 \cdot \left\{ \begin{Bmatrix} \dot{X} \\ \dot{Y} \\ \dot{Z} \end{Bmatrix} + \begin{Bmatrix} \dot{\alpha} \\ \dot{\beta} \\ \dot{\gamma} \end{Bmatrix} \times {}^{b}\mathbf{r}_2 + \left[J_2\right] \cdot \dot{q}_2 \right\}^2 + \\
& \frac{1}{2}\cdot M_3 \cdot \left\{ \begin{Bmatrix} \dot{X} \\ \dot{Y} \\ \dot{Z} \end{Bmatrix} + \begin{Bmatrix} \dot{\alpha} \\ \dot{\beta} \\ \dot{\gamma} \end{Bmatrix} \times {}^{b}\mathbf{r}_3 + \left[J_3\right] \cdot \dot{q}_3 \right\}^2 + \\
& \frac{1}{2}\cdot I_b \cdot \begin{Bmatrix} \dot{\alpha}^2 \\ \dot{\beta}^2 \\ \dot{\gamma}^2 \end{Bmatrix} + \frac{1}{2}\cdot I_0 \cdot \begin{Bmatrix} \dot{\alpha}^2 \\ \dot{\beta}^2 \\ \dot{\gamma}^2 \end{Bmatrix} + \frac{1}{2}\cdot I_1 \cdot \left\{ \left[{}^{t}_{1}A\right]^T \cdot \begin{Bmatrix} \dot{\alpha} \\ \dot{\beta} \\ \dot{\gamma} + \dot{q}_1 \end{Bmatrix} \right\}^2 + \\
& \frac{1}{2}\cdot I_2 \cdot \left\{ \left[{}^{t}_{2}A\right]^T \cdot \begin{Bmatrix} \dot{\alpha} \\ \dot{\beta} \\ \dot{\gamma} + \dot{q}_1 \end{Bmatrix} + \begin{Bmatrix} 0 \\ 0 \\ \dot{q}_2 \end{Bmatrix} \right\}^2 + \\
& \frac{1}{2}\cdot I_3 \cdot \left\{ \left[{}^{t}_{3}A\right]^T \cdot \begin{Bmatrix} \dot{\alpha} \\ \dot{\beta} \\ \dot{\gamma} + \dot{q}_1 \end{Bmatrix} + \begin{Bmatrix} 0 \\ 0 \\ \dot{q}_3 \end{Bmatrix} \right\}^2
\end{aligned}
$$

$$
V = \ \frac{1}{2}\cdot \left[K_b\right] \cdot \begin{Bmatrix} X \\ Y \\ Z \\ \alpha \\ \beta \\ \gamma \end{Bmatrix}^2 + \frac{1}{2}\cdot \left[K_r\right] \cdot \begin{Bmatrix} q_1 \\ q_2 \\ q_3 \end{Bmatrix}^2
$$

where ${}^{b}\mathbf{r}_i$ is the link "i" position vector in the base frame, see Section B.3

The lagrangian formulation is written for each of the variables, and the corriolis and centrifugal forces are ignored. The results can be put into the form:

$$\left[\left[M^*\right]+\left[I^*\right]\right]\cdot\ddot{S}+\left[K^*\right]\cdot\dot{S}+\left[B^*\right]\cdot S=0$$

where:

$$S=\left\{X\ Y\ Z\ \alpha\ \beta\ \gamma\right\}^T$$

$$\left[M^*\right]=\begin{bmatrix} M_0+M_1+M_2+M_3 & M_0\cdot T_0+M_1\cdot T_1+M_2\cdot T_2+M_3\cdot T_3 & M_1\cdot J_1+M_2\cdot J_2+M_3\cdot J_3 \\ M_0\cdot T_0{}^T+M_1\cdot T_1{}^T+M_2\cdot T_2{}^T+M_3\cdot T_3{}^T & M_0\cdot T_0\cdot T_0{}^T+M_1\cdot T_1\cdot T_1{}^T+M_2\cdot T_2\cdot T_2{}^T+M_3\cdot T_3\cdot T_3{}^T & M_1\cdot T_1{}^T\cdot J_1+M_2\cdot T_2{}^T\cdot J_2+M_3\cdot T_3{}^T\cdot J_3 \\ M_1\cdot J_1{}^T+M_2\cdot J_2{}^T+M_3\cdot J_3{}^T & M_1\cdot J_1{}^T\cdot T_1+M_2\cdot J_2{}^T\cdot T_2+M_3\cdot J_3{}^T\cdot T_3 & M_1\cdot J_1{}^T\cdot J_1+M_2\cdot J_2{}^T\cdot J_2+M_3\cdot J_3{}^T\cdot J_3 \end{bmatrix}$$

with:

$$T_i=\begin{bmatrix} 0 & {}^b r_{iz} & -{}^b r_{iy} \\ -{}^b r_{iz} & 0 & {}^b r_{ix} \\ {}^b r_{iy} & -{}^b r_{ix} & 0 \end{bmatrix}$$ and J_i is the Jacobian matrix of Section B.4

$$\left[I^*\right]=\begin{bmatrix} 0 & 0 & 0 \\ 0 & I22 & I23 \\ 0 & I32 & I33 \end{bmatrix}, \text{with } \left[I22\right]=\left[{}^t_1A\right]\left[I_1\right]\left[{}^t_1A\right]^T+\left[{}^t_2A\right]\left[I_2\right]\left[{}^t_2A\right]^T+\left[{}^t_3A\right]\left[I_3\right]\left[{}^t_3A\right]^T$$

$$\left[I32\right]=\begin{bmatrix} I22(3,1) & I22(3,2) & I22(3,3) \\ I_{2z}\cdot s_1+I_{3z}\cdot s_1 & -I_{2z}\cdot c_1-I_{3z}\cdot c_1 & 0 \\ I_{3z}\cdot s_1 & -I_{3z}\cdot c_1 & 0 \end{bmatrix}$$

$$\left[I23\right]=\left[I32\right]^T$$

$$\left[I33\right]=\begin{bmatrix} \begin{array}{l} I_{1y}+I_{2x}\cdot s_2{}^2+I_{2y}\cdot c_2{}^2+ \\ I_{3x}\cdot(s_2\cdot c_3+c_2\cdot s_3)^2 \\ +I_{3y}\cdot(c_2\cdot c_3+s_2\cdot s_3)^2 \end{array} & 0 & 0 \\ 0 & I_{2z}+I_{3z} & I_{3z} \\ 0 & I_{3z} & I_{3z} \end{bmatrix}$$

$[K^*] = \begin{bmatrix} K_b & 0 \\ 0 & K_r \end{bmatrix}$, with K_b=base stiffness matrix and K_r=robot stiffness matrix

$[B^*] = \begin{bmatrix} B_b & 0 \\ 0 & B_r \end{bmatrix}$, with B_b=base damping matrix and B_r=robot damping matrix

[illegible]